Chem

CellPress
OPEN ACCESS

Article

Breaking the trade-off between selectivity and adsorption capacity for gas separation

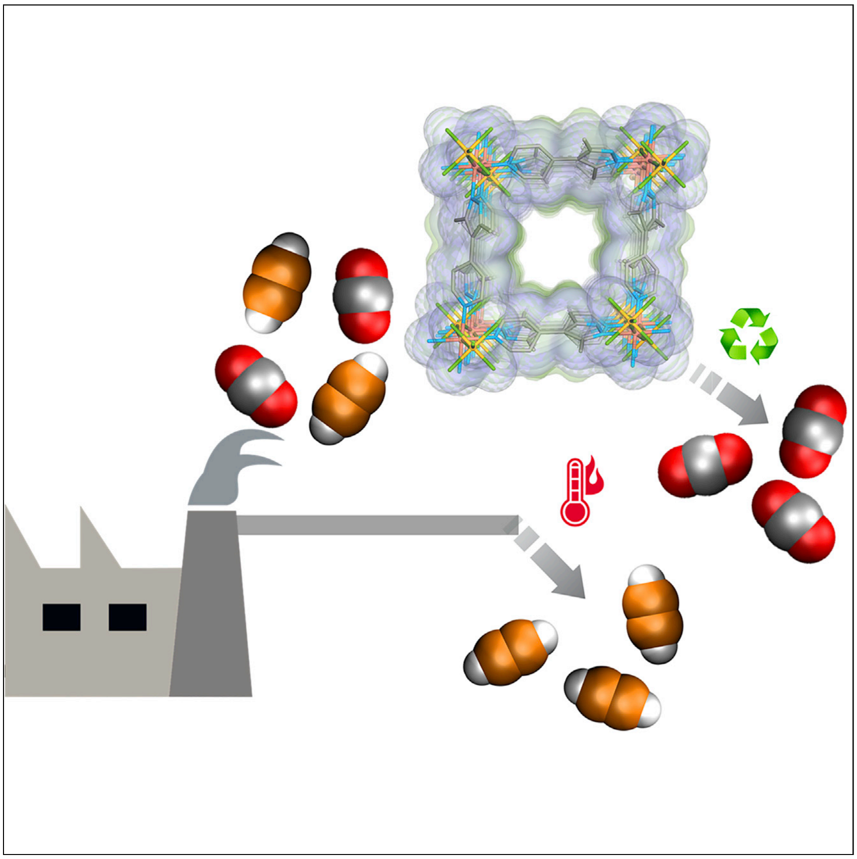

A new family of six isostructural hybrid ultramicroporous materials that enabled high adsorption capacity as well as high experimental separation selectivity values for C_2H_2/CO_2 separation.

Naveen Kumar, Soumya Mukherjee, Nathan C. Harvey-Reid, ..., Yining Huang, Paul E. Kruger, Michael J. Zaworotko

xtal@ul.ie

Highlights

Six isostructural hybrid ultramicroporous materials are prepared and characterized

Crystal engineering approach enabled fine-tuning of pore size and chemistry

Weak CO_2/strong C_2H_2 affinity resulted in high C_2H_2/CO_2 separation selectivities

SIFSIX-21-Ni: benchmark selectivity/uptake capacity for C_2H_2/CO_2 separation

7 AFFORDABLE AND CLEAN ENERGY

Kumar et al., Chem 7, 3085–3098
November 11, 2021 © 2021 The Authors.
Published by Elsevier Inc.
https://doi.org/10.1016/j.chempr.2021.07.007

Chem

CellPress
OPEN ACCESS

Article

Breaking the trade-off between selectivity and adsorption capacity for gas separation

Naveen Kumar,[1,7] Soumya Mukherjee,[1,7] Nathan C. Harvey-Reid,[2] Andrey A. Bezrukov,[1] Kui Tan,[3] Vinicius Martins,[4] Matthias Vandichel,[1] Tony Pham,[5] Lisa M. van Wyk,[6] Kolade Oyekan,[3] Amrit Kumar,[1] Katherine A. Forrest,[5] Komal M. Patil,[2] Leonard J. Barbour,[6] Brian Space,[5] Yining Huang,[4] Paul E. Kruger,[2] and Michael J. Zaworotko[1,8,*]

SUMMARY

The trade-off between selectivity and adsorption capacity with porous materials is a major roadblock to reducing the energy footprint of gas separation technologies. To address this matter, we report herein a systematic crystal engineering study of C_2H_2 removal from CO_2 in a family of hybrid ultramicroporous materials (HUMs). The HUMs are composed of the same organic linker ligand, 4-(3,5-dimethyl-1*H*-pyrazol-4-yl)pyridine, pypz, three inorganic pillar ligands, and two metal cations, thereby affording six isostructural pcu topology HUMs. All six HUMs exhibited strong binding sites for C_2H_2 and weaker affinity for CO_2. The tuning of pore size and chemistry enabled by crystal engineering resulted in benchmark C_2H_2/CO_2 separation performance. Fixed-bed dynamic column breakthrough experiments for an equimolar (v/v = 1:1) C_2H_2/CO_2 binary gas mixture revealed that one sorbent, SIFSIX-21-Ni, was the first C_2H_2 selective sorbent that combines exceptional separation selectivity (27.7) with high adsorption capacity (4 $mmol \cdot g^{-1}$).

The bigger picture

It is generally recognized that porous solids (sorbents) with high selectivity and high adsorption capacity offer potential for energy-efficient gas separations. Unfortunately, there is generally a trade-off between capacity and selectivity, which represents a roadblock to the utility of sorbents in key industrial processes. For example, acetylene (C_2H_2), an important fuel and chemical intermediate, is produced with CO_2 as an impurity, and the similar physicochemical properties of C_2H_2 and CO_2 mean that most sorbents are poorly selective. Hybrid ultramicroporous materials (HUMs) are candidates for gas separations as they exhibit benchmark selectivity for several key gas pairs. Unfortunately, existing HUMs are handicapped by low capacity. We report a new HUM, SIFSIX-21-Ni, that addresses the trade-off between selectivity and capacity that has plagued sorbents, as its high uptake and high selectivity renders it the new benchmark for C_2H_2/CO_2 separation performance.

INTRODUCTION

Acetylene (C_2H_2) is an important chemical commodity; it is used to manufacture vinyl and acrylate polymers and is a combustion fuel in oxy-acetylene torches.[1,2] The latter application stems from its flammability range, the widest known (2.5%–81%), but can thereby represent an explosion hazard at >2.5% concentrations.[3] Whereas the utility of C_2H_2 as an oxy-combustion fuel typically requires >98% purity grade for its use as a chemical feedstock, a higher purity grade is essential.[4] Bulk C_2H_2 is produced by either oxidative coupling (partial combustion) of methane or downstream thermal cracking of hydrocarbons; CO_2 is a by-product of both processes.[5] C_2H_2 production generates CO_2 as an impurity, which means that selective separation/purification of high-purity (>99% v/v) C_2H_2 from C_2H_2/CO_2 mixtures is of industrial relevance.[6] Three technologies are currently used to remove C_2H_2 from C_2H_2/CO_2 mixtures: (1) bulk solvent extraction, resulting in solvent waste such as *N*,*N*-dimethylformamide and acetone[7]; (2) partial hydrogenation of C_2H_2 to ethylene, C_2H_4, with costly noble-metal catalysts such as Ag(0)[8]; and (3) cryogenic distillation, an energy-intensive process.[9] All three processes suffer from high cost and low efficiency. Physisorbents offer potential for energy-efficient gas purification as exemplified by recent reports on physisorbents that exhibit benchmark performance for key separations such as CO_2/N_2,[10,11] CO_2/CH_4,[12] C_2H_2/C_2H_4,[13,14] and C_2H_6/C_2H_4,[15] among others.[16] Nevertheless, commercially viable C_2H_2 capture from CO_2 using physisorbents remains an unmet challenge since traditional physisorbents, such as zeolites, mesoporous silicas, and activated carbons, exhibit poor selectivity

© 2021 The Authors. Published by Elsevier Inc.

This is an open access article under the CC BY-NC-ND license (http://creativecommons.org/licenses/by-nc-nd/4.0/).

for C_2H_2 over CO_2[17] thanks to their similar physicochemical properties (molecular dimensions: $C_2H_2 = 3.32 \times 3.34 \times 5.7$ Å^3; $CO_2 = 3.18 \times 3.33 \times 5.36$ Å^3; kinetic diameters for both molecules = 3.3 Å; boiling points: C_2H_2 = 189.3 K, CO_2 = 194.7 K).[18,19] These physicochemical properties also practically rule out the application of molecular sieving.[20]

In this context, metal-organic materials (MOMs),[21] also known as metal-organic frameworks (MOFs)[22,23] or porous coordination polymers (PCPs),[24] have emerged as sorbent candidates to serve as C_2H_2 selective physisorbents in C_2H_2/CO_2 separation.[25] Unlike traditional classes of sorbents, the modularity of MOMs enables fine-tuning of pore size and pore chemistry using crystal engineering design approaches.[21] Nevertheless, there are >100,000 MOMs in the CSD MOF subset (2020.3 CSD release).[26] To the best of our knowledge, only a few (20) have been experimentally studied for C_2H_2/CO_2 separation under dynamic conditions (e.g., dynamic column breakthrough [DCB] experiments, see Table S1) including recently reported benchmarks set by **ATC-Cu**,[27] **FJI-H8-Me**,[28] and **SIFSIX-Cu-TPA**.[29] For example, **ATC-Cu** was found to exhibit an ideal adsorbed solution theory (IAST) selectivity of 53.6 for 1:1 C_2H_2/CO_2 separation.[27] The need to study sorbent performances under dynamic conditions arises because calculation of separation performance from C_2H_2 and CO_2 single-component isotherms tends to overestimate separation performance. IAST and fixed-bed simulated breakthrough calculations are, therefore, indicative rather than confirmative. Our review of the literature reveals that C_2H_2/CO_2 separation selectivity (α_{AC}) values for equimolar (v/v) mixtures have been experimentally measured for only 16 sorbents, most of which are classified as MOFs: **SIFSIX-Cu-TPA**,[29] **TCuI**,[30] **TCuBr**,[30] **TCuCl**,[30] **JCM-1**,[31] **NKMOF-1-Ni**,[32] **FJU-22a**,[33] **FJU-89a**,[34] **HOF-3**,[35] **FJU-6-TATB**,[36] **SSNU-45**,[37] **JXNU-5**,[38] **FJU-36a**,[39] **FeNiM′MOF**,[40] **UTSA-74a**,[41] and **sql-16-Cu-NO$_3$-α′**.[42] Whereas these results are promising, they do not fully address the *spectrum of performance parameters* needed before a material can be considered for commercialization.[43] In particular, in addition to selectivity, working capacity and recyclability (including the kinetics and energy of regeneration) are also key performance parameters.[25,44] As revealed in Table S1, **UTSA-74a** is the only sorbent that offers separation selectivity ≥ 5 and adsorption capacity ≥ 3.5 mmolg^{-1}. Unfortunately, **UTSA-74a** requires a high temperature for sorbent regeneration and activation (473 K under high vacuum) to generate the unsaturated metal centers (UMCs) that drive preferential binding for C_2H_2 over CO_2.

Hybrid ultramicroporous materials (HUMs), sorbents that exhibit <0.7 nm pore diameter and are comprised of both organic and inorganic linker ligands, are an emerging subclass of MOMs.[45] HUMs are outstanding candidates for physisorptive separation of small gas sorbates as they offer benchmark adsorption selectivities for C_2H_2 over C_2H_4 (S_{AE})[14,18] and CO_2 over N_2 (S_{CN}).[16,19,46] This performance has been attributed to two key features that enhance selective binding: (1) narrow pore sizes and (2) pore surfaces/walls offering strong electrostatics. HUMs are also modular, which enables crystal engineering-driven control of pore size and chemistry to facilitate removal of even trace impurities. Unfortunately, narrow pore size, as seen in the prototypal pyrazine-linked HUMs, tends to limit surface area and uptake capacity. We recently reported that an HUM based on an expanded symmetrical ligand, 3,3′,5,5′-tetramethyl-1*H*,1′*H*-4,4′-bipyrazole, pzpz, offered a highly selective CO_2 binding site that was also hydrophobic.[11] Six members of a new HUM platform based on an unsymmetrical ligand that is related to pzpz, 4-(3,5-dimethyl-1*H*-pyrazol-4-yl)pyridine (pypz) are introduced herein. The six HUMs were obtained by inorganic ligand (SiF_6^{2-}, SIFSIX; TiF_6^{2-}, TIFSIX; and $NbOF_5^{2-}$, NbOFFIVE) and/or metal

[1] Bernal Institute, Department of Chemical Sciences, University of Limerick, Limerick V94 T9PX, Republic of Ireland

[2] MacDiarmid Institute for Advanced Materials and Nanotechnology, School of Physical and Chemical Sciences, University of Canterbury, Private Bag 4800, Christchurch 8140, New Zealand

[3] Department of Materials Science & Engineering, University of Texas at Dallas, Richardson, TX 75080, USA

[4] Department of Chemistry, the University of Western Ontario, 1151 Richmond Street, London, ON N6A 5B7, Canada

[5] Department of Chemistry, University of South Florida, 4202 East Fowler Avenue, CHE205, Tampa, FL 33620-5250, USA

[6] Department of Chemistry and Polymer Science, University of Stellenbosch, Stellenbosch, Matieland 7602, South Africa

[7] These authors contributed equally

[8] Lead contact

*Correspondence: xtal@ul.ie

https://doi.org/10.1016/j.chempr.2021.07.007

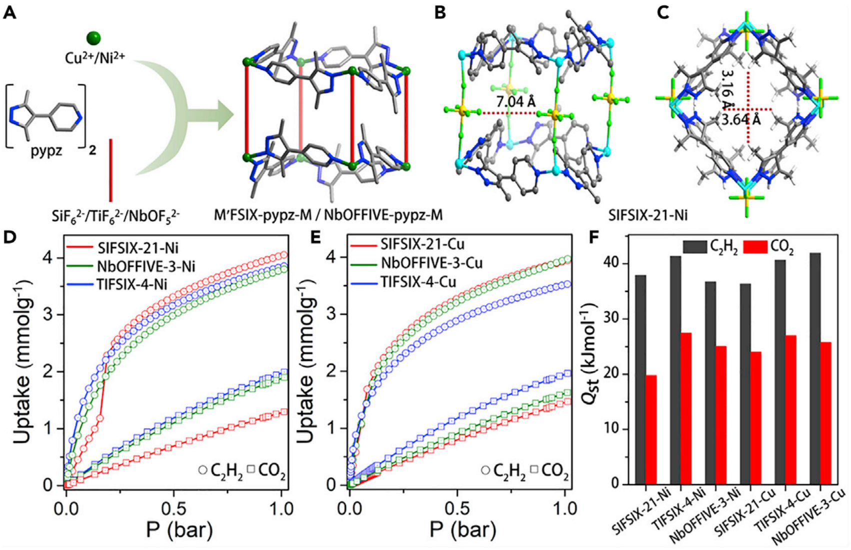

Figure 1. The family of isostructural HUMs reported herein and their single-crystal X-ray structures, single-component adsorption isotherms, and isosteric heats of adsorption

(A) Schematic illustration of the building blocks and pcu network topology of **M′FSIX-pypz-M** and **NbOFFIVE-pypz-M**.

(B) C_2H_2 binding site in **SIFSIX-21-Ni** viewed across diagonally opposite F atoms of SiF_6^{2-} pillars.

(C) The ultramicropore in **SIFSIX-21-Ni** viewed along the crystallographic *b* axis.

(D) C_2H_2 and CO_2 isotherms of **SIFSIX-21-Ni**, **NbOFFIVE-3-Ni**, and **TIFSIX-4-Ni** at 298 K.

(E) C_2H_2 and CO_2 isotherms of **SIFSIX-21-Cu**, **NbOFFIVE-3-Cu**, and **TIFSIX-4-Cu** at 298 K.

(F) Comparative bar diagram of isosteric heat of adsorptions (C_2H_2 and CO_2). (Color codes in Figures 1A–1C: C, gray; N, blue; Si, yellow; F, light green; Ni, cyan.)

(Ni^{2+} or Cu^{2+}) substitution (Figure 1A) and offer higher gravimetric surface areas (and, therefore, potentially higher working capacity) than the corresponding pyrazine-linked HUMs.[47] Herein, we report the exceptional adsorptive separation performance for C_2H_2 versus CO_2 of these HUMs as evaluated by single-component gas sorption measurements, dynamic gas breakthrough experiments, *in situ* IR studies, solid-state NMR experiments, and molecular modeling.

RESULTS AND DISCUSSION

Synthesis and structural characterization

Single crystals of **SIFSIX-21-Ni**, **TIFSIX-4-Ni**, **SIFSIX-21-Cu**, and **TIFSIX-4-Cu**, and microcrystalline samples of **NbOFFIVE-3-Ni** and **NbOFFIVE-3-Cu** were prepared as detailed in the supplemental information. Single-crystal X-ray diffraction (SCXRD) studies revealed that **SIFSIX-21-Ni**, **TIFSIX-4-Ni**, **SIFSIX-21-Cu**, and **TIFSIX-4-Cu** are isostructural and crystallize as **pcu** topology networks in orthorhombic space group *Pnna*. The crystallographic data and refinement parameters for **SIFSIX-21-Ni**, **TIFSIX-4-Ni**, **SIFSIX-21-Cu**, and **TIFSIX-4-Cu** are presented in Table S2. The unit cell parameters calculated from powder X-ray diffraction (PXRD) for **NbOFFIVE-3-Cu** and **NbOFFIVE-3-Ni** are close to those of the M′FSIX analogs (Figures S3 and S4). Unit cell volumes are as follows: **TIFSIX-4-Cu** (3,458.8 $Å^3$)> **SIFSIX-21-Cu** (3,361.1 $Å^3$)> **NbOFFIVE-3-Cu** (3,338 $Å^3$)> **TIFSIX-4-Ni** (3,291.7 $Å^3$)> **NbOFFIVE-3-Ni** (3,236 $Å^3$)> **SIFSIX-21-Ni** (3,199.2 $Å^3$). Solvent-accessible free volumes were calculated to be *ca.* 30%. Polycrystalline samples of **SIFSIX-21-Ni**, **TIFSIX-4-Ni**, **SIFSIX-21-Cu**, and **TIFSIX-4-Cu** used for physicochemical characterization and sorption studies were prepared solvothermally in methanol (see supplemental information for details). Bulk phase purity was established by comparison of experimental and calculated PXRD patterns (Figures S1 and S2). Thermogravimetric analysis and variable temperature PXRD (VT-PXRD) experiments revealed each material retained crystallinity as follows: 613 K (**NbOFFIVE-3-Ni**) > 573 K (**TIFSIX-4-Ni**) > 513 K (**SIFSIX-21-Ni**); 533 K (**TIFSIX-4-Cu**) > 513 K (**NbOFFIVE-3-Cu**) > 493 K (**SIFSIX-21-Cu**) (Figures S5–S10 and S13–S14).

Single-component gas isotherms and binding sites

To evaluate microporosity, N_2 and CO_2 adsorption isotherms were measured at 77 K and 195 K, respectively (Figures S15, S17, S19, S21, S23, and S25). Following the Rouquerol criteria,[48] Brunauer-Emmett-Teller (BET) surface areas were experimentally determined from the N_2 adsorption isotherms as follows: **TIFSIX-4-Ni** (931 m^2g^{-1}) > **SIFSIX-21-Ni** (871 m^2g^{-1}) > **SIFSIX-21-Cu** (839 m^2g^{-1}) > **NbOFFIVE-3-Cu** (805 m^2g^{-1}) > **NbOFFIVE-3-Ni** (761 m^2g^{-1}) > **TIFSIX-4-Cu** (747 m^2g^{-1}). C_2H_2 and CO_2 single-component gas sorption isotherms were collected at 298 K and 273 K (Figures S16, S18, S20, S22, S24, and S26). All six HUMs were observed to exhibit higher affinity for C_2H_2 than CO_2 with C_2H_2 uptakes >3.5 $mmolg^{-1}$ and CO_2 uptakes <2.0 $mmolg^{-1}$ at 298 K and 1 bar (Figures 1D and 1E). **SIFSIX-21-Ni** was found to exhibit the highest C_2H_2 uptake (~4.05 $mmolg^{-1}$), followed by **NbOFFIVE-3-Cu** (3.97 $mmolg^{-1}$), **SIFSIX-21-Cu** (3.94 $mmolg^{-1}$), **TIFSIX-4-Ni** (3.85 $mmolg^{-1}$), **NbOFFIVE-3-Ni** (3.79 $mmolg^{-1}$), and **TIFSIX-4-Cu** (3.53 $mmolg^{-1}$) (Figures 1D and 1E). The stepped isotherms observed for **SIFSIX-21-Ni** (Figure S16) and **SIFSIX-21-Cu** (Figure S22) prompted us to conduct *in situ* PXRD measurements on these two HUMs. These measurements (Figures S11 and S12) reveal no significant change in the PXRD patterns with C_2H_2 loading until 1 bar indicated that only subtle structural changes occurred during C_2H_2 sorption. Isosteric heats of adsorption, Q_{st}, were determined from virial fits of these experimental single-component gas isotherms. Q_{st} values for CO_2 at zero loading, $Q_{st}(CO_2)$, were as follows: 19.8 kJ mol^{-1} (**SIFSIX-21-Ni**) < 24.0 kJ mol^{-1} (**SIFSIX-21-Cu**) < 25.1 kJ mol^{-1} (**NbOFFIVE-3-Ni**) < 25.8 kJ mol^{-1} (**NbOFFIVE-3-Cu**) < 27.0 kJ mol^{-1} (**TIFSIX-4-Cu**) < 27.5 kJ mol^{-1} (**TIFSIX-4-Ni**). Q_{st} (C_2H_2) values were determined to be as follows: 36.3 kJ mol^{-1} (**SIFSIX-21-Cu**) < 36.7 kJ mol^{-1} (**NbOFFIVE-3-Ni**) < 37.9 kJ mol^{-1} (**SIFSIX-21-Ni**) < 40.6 kJ mol^{-1} (**TIFSIX-4-Cu**) < 41.3 kJ mol^{-1} (**TIFSIX-4-Ni**) < 41.9 kJ mol^{-1} (**NbOFFIVE-3-Cu**) (Figures 1F amd S27–S32; all virial fitting parameters are provided in Figures S33–S44). The differences between $Q_{st}(C_2H_2)$ and $Q_{st}(CO_2)$, $(\Delta Q_{st})_{AC}$ = $[Q_{st}(C_2H_2) - Q_{st}(CO_2)]$, were as follows: 18.1 kJ mol^{-1} (**SIFSIX-21-Ni**) > 16.1 kJ mol^{-1} (**NbOFFIVE-3-Cu**) > 13.9 kJ mol^{-1} (**TIFSIX-4-Ni**) > 13.6 kJ mol^{-1} (**TIFSIX-4-Cu**) > 12.3 kJ mol^{-1} (**SIFSIX-21-Cu**) > 11.6 kJ mol^{-1} (**NbOFFIVE-3-Ni**). These Q_{st} and ΔQ_{st} values reveal the relative thermodynamic preferences of the studied sorbents toward the competing sorbates, C_2H_2 and CO_2. Adsorption selectivities were calculated using IAST.[49] For C_2H_2/CO_2 (v/v: 1:1 and 2:1) at 1 bar and 298 K, IAST selectivities (S_{AC}) were calculated upon fitting the single-component isotherms to the dual-site Langmuir-Freundlich equation (see supplemental information for details; Figures S51, S52, and Table S3). S_{AC} (1:1/2:1) values at 1 bar were thereby determined to be 10.0/9.4 (**SIFSIX-21-Cu**) > 9.5/9.0 (**NbOFFIVE-3-Cu**) > 8.3/8.1 (**TIFSIX-4-Cu**) > 7.8/7.8 (**SIFSIX-21-Ni**) > 7.6/7.4 (**TIFSIX-4-Ni**) > 6.0/5.9 (**NbOFFIVE-3-Ni**) (Figures S45–S50). As presented in Table S1, under relevant partial pressures, S_{AC} for the six HUMs studied in this contribution were found to be comparable to leading C_2H_2-capture sorbents such as **SIFSIX-Cu-TPA**(5.3),[29] **MUF-17**(6),[50] **ZJU-60a**(6.7),[51] **FJU-22a**(7.1),[33] **TCuBr** (9.5),[30] **ZJUT-2a**(10),[52] **TIFSIX-2-Cu-i**(10),[53] **FJI-H8-Me**(10.4),[28] and **MIL-100(Fe)**(12.5).[54]

The binding sites for CO_2 and C_2H_2 in **SIFSIX-21-Ni** were determined by simulated annealing calculations (Figure 2). The binding energies at 0.1 bar obtained from canonical Monte Carlo (CMC) were in agreement with the experimentally derived low loading $Q_{st}(C_2H_2)$ and $Q_{st}(CO_2)$ obtained from single-component isotherms (Table S4). Results derived by these two simulation methods revealed that C_2H_2 molecules

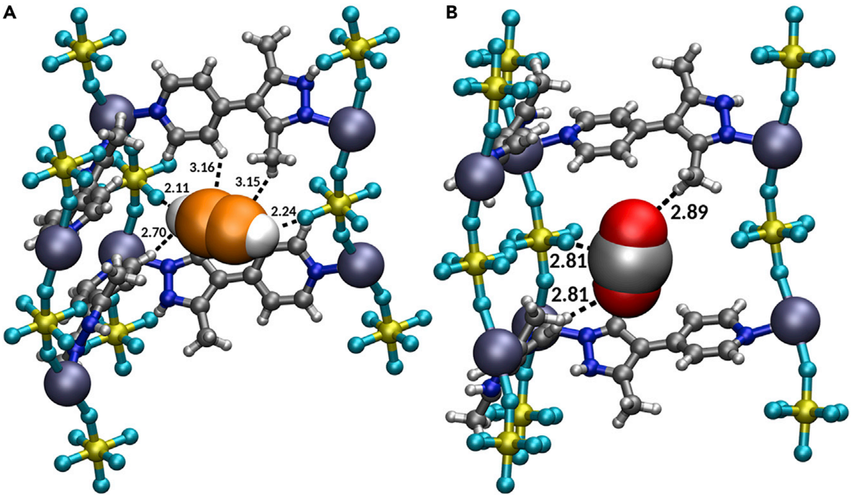

Figure 2. The binding sites in SIFSIX-21-Ni that result in strong C_2H_2 affinity versus CO_2

(A and B) Views of (A) C_2H_2 binding sites and (B) CO_2 binding sites in **SIFSIX-21-Ni** as determined from molecular simulations (C_2H_2 and CO_2 molecules are shown in space-filling model whereas **SIFSIX-21-Ni** is presented in ball-and-stick model) (color codes: N, blue; Si, yellow; F, turquoise; Ni, lilac; O, red; H, white; C, gray, except in the C_2H_2 molecule: orange).

interact with a pair of diagonally opposite F atoms of the inorganic pillars (SiF_6^{2-}) via two $(C_2H_2)CH^{\delta+}\cdots F^{\delta-}$ interactions. There are also $CH\cdots C(C_2H_2)$ interactions. CO_2 molecules form $C^{\delta+}\cdots F^{\delta-}$ and $CH\cdots O(CO_2)$ interactions. To further understand these binding sites, density function theory (DFT) refinements were conducted on the strongest binding sites of **SIFSIX-21-Ni** as identified by CMC simulations in order to calculate the adsorption enthalpies at low loading (one adsorbate molecule per unit cell). Employing the BEEF-vdW functional,[55] adsorption enthalpies of −45.3 and −30.1 kJ mol^{-1} were calculated for C_2H_2 and CO_2, respectively. The adsorption enthalpy difference of 15 kJ mol^{-1} correlates well with experimental ΔQ_{st} values (Figure 1F). For the BEEF-vdW optimized structures (see supplemental information), the optimized binding pocket with adsorbed C_2H_2 has two short $F^{\delta-}\cdots H^{\delta+}$ interactions (2.15 Å each, Figure S53A). For CO_2, $F^{\delta-}\cdots C^{\delta+}$ interactions of 3.69 Å and $CH\cdots O(CO_2)$ interactions of 2.95 and 3.34 Å (Figure S53B) were determined. For CO_2 adsorption, an alternate binding site with similar adsorption enthalpies (± 1 kJ mol^{-1}) with shorter $F^{\delta-}\cdots C^{\delta+}$ interactions of 3.10 Å and $CH\cdots O(CO_2)$ interactions of 2.59 and 3.15 Å were observed (Figure S53C). Because the adsorbates maximized their interactions within the binding pocket (Figure S53), these enthalpies are higher than the $Q_{st}(C_2H_2)$ and $Q_{st}(CO_2)$ determined from CMC simulations, the latter representing the average binding energy distribution at a certain pressure. Therefore, the loss in translational entropy was found to be higher for C_2H_2 than for CO_2. Experimental Q_{st} values representing a distribution averaged energy over all possible adsorption configurations of 16.1 $kJmol^{-1}$ (CO_2) and 40.6 $kJmol^{-1}$ (C_2H_2) were found to be slightly lower than the adsorption enthalpies computationally predicted from the optimal binding sites. Therefore, one can conclude that the average residence time of C_2H_2 in its most stable binding site compared with that of CO_2 is higher, suggesting that CO_2 will exhibit faster kinetics. When the CO_2 binding site of **SIFSIX-21-Ni** is compared with that of **SIFSIX-3-Ni**, unlike the single $C^{\delta+}\cdots F^{\delta-}$ binding interaction in **SIFSIX-21-Ni**, **SIFSIX-3-Ni** was found to exhibit four $C^{\delta+}\cdots F^{\delta-}$ binding interactions to electronegative F atoms from four independent SiF_6^{2-} anions.[56] Like **SIFSIX-18-Ni-β**, **SIFSIX-21-Ni** exhibits $C^{\delta+}\cdots F^{\delta-}$ and $CH\cdots O$ interactions with CO_2, however **SIFSIX-18-Ni-β** was found to exhibit multiple $CH\cdots O$ interactions thanks to the presence of extra methyl groups in pzpz over pypz.[11] Therefore, both **SIFSIX-3-Ni** and **SIFSIX-18-Ni-β** exhibit significantly higher CO_2 binding energies compared with **SIFSIX-21-Ni**.[11,56] Conversely, **SIFSIX-21-Ni** exhibits $CH^{\delta+}\cdots F^{\delta-}$ interactions with C_2H_2 similar to those observed in **SIFSIX-2-Cu-i** and **TIFSIX-2-Cu-i** thanks to their "sweet spots" for C_2H_2 binding (F•••F distance of *ca.* 7 Å, see Figure 1B).[13,53] In summary, the binding sites in the pypz HUMs reported herein combine key features that imply strong C_2H_2 affinity versus CO_2: $CH^{\delta+}\cdots F^{\delta+}$ interaction-driven binding sites for C_2H_2; weak CO_2-sorbent interactions.

Adsorption kinetics

Kinetics is a key factor in determining the efficiency of gas separations.[44] We, therefore, studied the pure gas adsorption kinetics for C_2H_2 and CO_2 for each of the activated samples (**SIFSIX-21-Ni**, **TIFSIX-4-Ni**, **NbOFFIVE-3-Ni**, **SIFSIX-21-Cu**, **TIFSIX-4-Cu**, and **NbOFFIVE-3-Cu**) by exposure to a constant flow of 10 cm^3min^{-1} of C_2H_2 or CO_2 at 303 K and 1.0 bar (Figures S54 and S55). After 5 cycles of C_2H_2 sorption, the order of uptakes were as follows: **SIFSIX-21-Cu** (7.8%) < **TIFSIX-4-Cu** (9.7%) < **NbOFFIVE-3-Cu** (10%) for the Cu(II) HUMs; **NbOFFIVE-3-Ni** (4.2%) ~ **TIFSIX-4-Ni** (4.3%) < **SIFSIX-21-Ni** (5.9%) for the Ni(II) HUMs (Figures S54 and S55). Meanwhile, the corresponding order after 3 cycles of CO_2 sorption were as follows: **NbOFFIVE-3-Cu** (0.73%) ~ **SIFSIX-21-Cu** (0.78%) < **TIFSIX-4-Cu** (1.5%) and **SIFSIX-21-Ni** (0.84%) ~ **TIFSIX-4-Ni** (0.85%) < **NbOFFIVE-3-Ni** (0.96%) for the Cu(II) and Ni(II) HUMs, respectively. The HUMs with the highest gravimetric uptakes, **NbOFFIVE-3-Cu** and **SIFSIX-21-Ni**, reached *ca.* 99% of their saturation uptakes in 54 and 35 min, respectively. For all HUMs, sorbent regeneration was conducted over five consecutive C_2H_2 adsorption/desorption cycles at 333 K under N_2 flow in <30 min (flow rate: 20 cm^3min^{-1}; Figures S54 andS55) for C_2H_2.

Dynamic column breakthrough (DCB) studies

Next, we investigated the C_2H_2/CO_2 separation performances of these HUMs through DCB experiments[57] with inlet gas mixture ratios 1:1 or 2:1 (v/v) for C_2H_2/CO_2.[1] Binary gas mixtures were passed through a fixed-bed reactor (8 mm diameter) filled with *ca.* 0.5 g of each HUM with a total gas flow rate of 1 cm^3min^{-1} at 1 bar and 298 K. Pre-activated samples were first heated at 333 K in a 20 cm^3min^{-1} flow of He to remove atmospheric impurities as monitored by gas chromatographic (GC) analysis of the effluent gas stream. The sorbent beds were then cooled to room temperature under continuous He flow and subjected to DCB experiments. Eluted gaseous components were continuously monitored through GC analysis (see supplemental information for details, Figure S56). Figure 3 reveals that CO_2 breakthrough occurred before that of C_2H_2 for each HUM and that **SIFSIX-21-Ni** was the best-performing sorbent, C_2H_2 breakthrough occurring at 363 and 298 min g^{-1} for the 1:1 and 2:1 gas mixtures, respectively. In contrast, the corresponding CO_2 breakthrough occurred at 152 and 114 min g^{-1} for the 1:1 and 2:1 gas mixtures, respectively. The time lags of 211 and 184 min g^{-1} between C_2H_2 and CO_2 breakthroughs for 1:1 and 2:1 gas mixtures, respectively, imply high C_2H_2 productivities.

GC data revealed that, for the 1:1 experiments, C_2H_2 levels in the effluent CO_2 gas stream were 623, 910, 1,751, 2,368, 2,368, and, 2,718 ppm for **SIFSIX-21-Ni**, **NbOFFIVE-3-Cu**, **TIFSIX-4-Cu**, **SIFSIX-21-Cu**, **TIFSIX-4-Ni**, and **NbOFFIVE-3-Ni**, respectively. Unlike the low uptakes of CO_2 registered in single-component isotherms (Figures 1D and 1E), 1:1 and 2:1 C_2H_2/CO_2 DCB experiments (Figure 3) revealed higher adsorbed CO_2 amounts indicated by coadsorption at lower partial pressures in dynamic experiments. Until C_2H_2 breakthrough occurred, CO_2 purity values in the effluent streams were found to be as follows: >99.9% for **SIFSIX-21-Ni** and

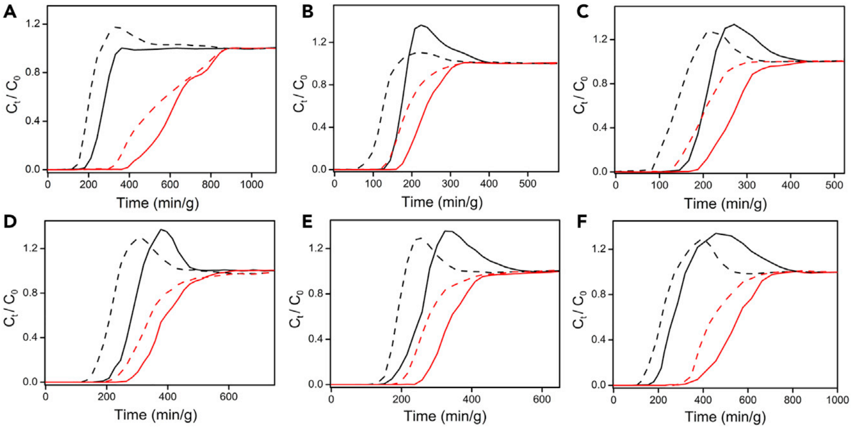

Figure 3. Experimental dynamic column breakthrough curves

(A–F) Binary C_2H_2/CO_2 mixture-based DCB experimental curves at 298 K and 1 bar on the studied family of pypz HUM sorbents (v/v = 1:1, solid line; 2:1, dashed line; C_2H_2, red; CO_2, black) (A), (B), and (C): **SIFSIX-21-Ni**, **TIFSIX-4-Ni**, and **NbOFFIVE-3-Ni**, respectively, and (D), (E), and (F): **SIFSIX-21-Cu**, **TIFSIX-4-Cu**, and **NbOFFIVE-3-Cu**, respectively (see details in the supplemental information).

NbOFFIVE-3-Cu; >99.7% for **TIFSIX-4-Cu**, **SIFSIX-21-Cu**, **TIFSIX-4-Ni**, and **NbOFFIVE-3-Ni**, i.e., higher than the commercial specification for CO_2 (N2.0, 99%). C_2H_2 uptakes calculated from the breakthrough curves for **SIFSIX-21-Ni**, **NbOFFIVE-3-Cu**, **TIFSIX-4-Cu**, **SIFSIX-21-Cu**, **TIFSIX-4-Ni**, and **NbOFFIVE-3-Ni** were observed to be 3.22, 3.08, 2.8, 3.07, 3.02, and 2.88 mmolg^{-1}, respectively (see supplemental information for details)[58,59]; these values are consistent with the respective isotherm-based uptakes at 0.5 bar. The DCB experiments enabled calculation of the separation selectivities (α_{AC}) for 1:1 and 2:1 C_2H_2:CO_2 mixtures: **SIFSIX-21-Ni** (27.7/10.0) > **NbOFFIVE-3-Cu** (16.9/7.9) > **NbOFFIVE-3-Ni** (15.0/6.5) > **TIFSIX-4-Cu** (5.4/4.1) > **SIFSIX-21-Cu** (4.6/3.1) > **TIFSIX-4-Ni** (4.4/3.1). **SIFSIX-21-Ni** exceeds the separation selectivities reported for **UTSA-74a** (20.1), **JXNU-5** (9.9), **JCM-1** (4.4), **FJU-89** (3), **SNNU-45** (2.9), **NKMOF-1-Ni** (2.6), **FJU-6-TATB** (2.3), **FJU-36a** (2.1), **HOF-3** (2), **SIFSIX-Cu-TPA** (1.97), **FJU-22a** (1.9), and **FeNi-M′MOF** (1.7) (Table S1). After full saturation in the equimolar DCB experiments, temperature programmed desorption measurements were conducted at 333 K (Figure S57). The desorption profiles revealed complete adsorbent regeneration in <120 min under a He flow of 20 cm^3 min^{-1} for **SIFSIX-21-Ni** and **NbOFFIVE-3-Cu**.

A mapping of α_{AC} versus equilibrium single-component C_2H_2 uptakes at 1 bar indicates that **SIFSIX-21-Ni, NbOFFIVE-3-Cu, NbOFFIVE-3-Ni, TIFSIX-4-Cu,** and **UTSA-74a** have potential to address the trade-off between adsorption capacity and separation selectivity for C_2H_2/CO_2 separation as they are the only sorbents that exhibit $\alpha_{AC} \geq 5$ and adsorption capacity ≥ 3.5 mmolg^{-1} (see Figure 4A for a comparison of performance parameters). The UMCs in **UTSA-74a** require high temperature for activation (473 K under high vacuum (Figure 4A). Conversely, the HUM sorbents require heating to only 333 K for sorbent regeneration. Overall, **SIFSIX-21-Ni** outperforms the other HUMs reported herein like **UTSA-74a** and other known C_2H_2 selective sorbents thanks to its high separation selectivity (27.7), C_2H_2 uptake (4.0 mmolg^{-1}), and low regeneration temperature. Interestingly, the high C_2H_2/CO_2 separation selectivities for **M′FSIX-pypz-M/NbOFFIVE-pypz-M** can be attributed as much to weak CO_2 binding as to strong C_2H_2 affinity as reflected in $(\Delta Q_{st})_{AC}$ values. **SIFSIX-21-Ni** exhibits a relatively low $Q_{st}(CO_2)$ of 19.8 kJ mol^{-1} at low loading versus other C_2H_2 selective physisorbents

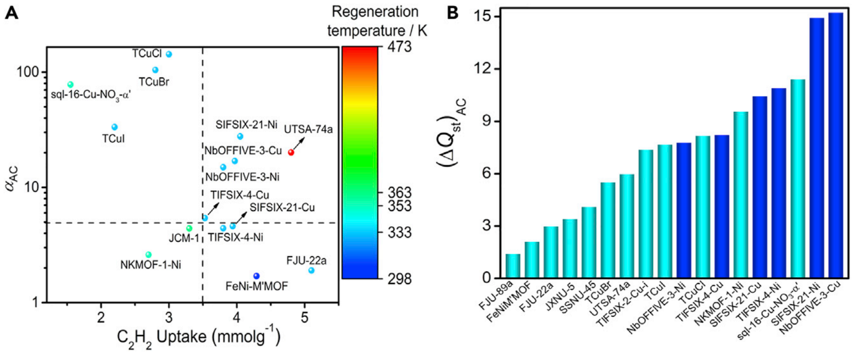

Figure 4. Comparison of separation selectivity versus uptake capacity and ΔQ_{st}

(A) Comparison of C_2H_2/CO_2 separation selectivity α_{AC} (v/v = 1:1) and gravimetric C_2H_2 uptake at 1 bar in benchmark C_2H_2/CO_2 separating adsorbents; regeneration/activation temperatures (range 298 to 473 K shown on the right side).

(B) Comparison of $(\Delta Q_{st})_{AC}$ for the best-performing adsorbents at half loadings.

(Table S1), resulting in a high $(\Delta Q_{st})_{AC}$ of 18.1 kJ mol^{-1}. Indeed, $(\Delta Q_{st})_{AC}$ at low loading for **SIFSIX-21-Ni** is close to that of **NKMOF-1-Ni** (19.4) kJ mol^{-1} (Figure S59), which exhibits an exceptionally high $Q_{st}(C_2H_2)$ of 60.3 kJ mol^{-1}. However, as Figure S58 reveals, the $Q_{st}(C_2H_2)$ for **NKMOF-1-Ni** rapidly declines to 46.0 kJ mol^{-1} at half loading, at which point $(\Delta Q_{st})_{AC}$ is reduced to 9.5 kJ mol^{-1} (Figure 4B). $(\Delta Q_{st})_{AC}$ values at zero coverage, although widely used, tend to overestimate separation performance at relevant partial pressures. In our experience, for most C_2H_2 selective sorbents, particularly those with high surface areas, $Q_{st}(C_2H_2)$ at half and full coverage decline from their zero loading values because of weak multilayer adsorption. Therefore, comparing $(\Delta Q_{st})_{AC}$ at low coverage does not always translate well to a prediction of relative binding affinity and is why we consider $(\Delta Q_{st})_{AC}$ at half loading to be a suitable metric to estimate relative binding for an equimolar mixture.[42] Figure 4B reveals that **NbOFFIVE-3-Cu** and **SIFSIX-21-Ni** set new benchmarks of $(\Delta Q_{st})_{AC}$ values at half loading, 15.2 and 14.9 kJmol^{-1}, respectively. This result is consistent with their DCB separation performances especially higher α_{AC} relative to those of **TIFSIX-4-Ni**, **SIFSIX-21-Cu**, **TIFSIX-4-Cu**, and **NbOFFIVE-3-Ni**. Overall, $(\Delta Q_{st})_{AC}$ values of at least 7.5 kJmol^{-1} for all HUMs reported herein suggests thermodynamic preference for C_2H_2 over CO_2 and correlates well with their high α_{AC} values.

Spectroscopic studies

In situ *infrared spectroscopy*

To further probe the binding sites of C_2H_2 and CO_2 in these HUMs, we carried out *in situ* infrared (IR) spectroscopy measurements of C_2H_2 and CO_2 adsorption in the two best-performing adsorbents, **NbOFFIVE-3-Cu** and **SIFSIX-21-Ni**. The difference spectra for **NbOFFIVE-3-Cu** (Figure 5) and **SIFSIX-21-Ni** (Figure S60) demonstrate characteristic stretching bands for adsorbed C_2H_2 and CO_2 molecules, i.e., $\nu_{as}(C_2H_2)$ at 3,309–3,209 cm^{-1} and $\nu_{as}(CO_2)$ at 2,338 cm^{-1}, whereas the perturbations of vibrational bands in the HUMs are characterized by the decrease in $\nu(CH)_{phenyl}$ peak intensity and its derivative feature in the shorter region, 1,700–1,000 cm^{-1}. The perturbed bands $\nu(CH)_{phenyl}$, $\nu(CC)_{phenyl}$, $\delta(CH)_{ip,\ phenyl}$, and $\nu(CN)_{phenyl}$ (see Figures 5, S60, and S61) indicate that C_2H_2 and CO_2 interact with the linker ligand's phenyl rings,[60] as predicted computationally (Figure 2). Analysis of these data revealed that concomitant loading of C_2H_2 perturbs the vibrational bands of the HUMs more than CO_2, which is also indicative of stronger sorbent-sorbate interactions for C_2H_2. Particularly, two distinct $\nu_{as}(C_2H_2)$ bands are present at 3,209 and 3,309 cm^{-1} in both **NbOFFIVE-3-Cu** and **SIFSIX-21-Ni**. These bands suggest two types of C_2H_2 binding

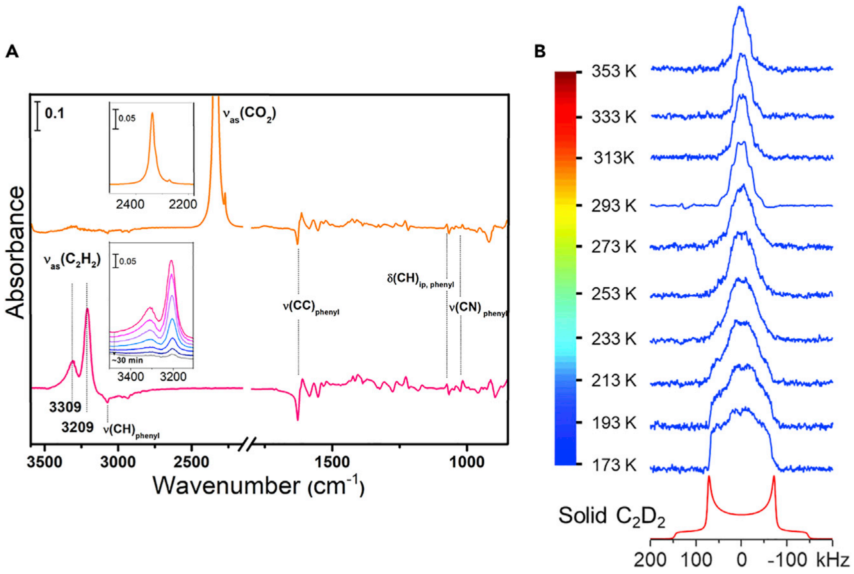

Figure 5. *In situ* infrared spectra and ^{2}H static NMR spectra

(A) Difference IR spectra showing the adsorbed CO_2 (orange) and C_2H_2 (pink) upon loading at 298 K and 1 bar adsorbate pressure into **NbOFFIVE-3-Cu** and subsequent evacuation of the gas phase within 3 s, respectively. Each is referenced to the spectrum of activated HUMs. Top inset shows the $\nu_{as}(CO_2)$ band and the bottom inset shows the decay of $\nu_{as}(C_2H_2)$ bands under vacuum. Notation and acronym: ν, stretching; δ, deformation; *ip*, in plane.

(B) Experimental ^{2}H static NMR spectra of C_2D_2 adsorbed in **NbOFFIVE-3-Cu** (at a loading level of 0.4 C_2D_2 per Cu) as a function of temperature (blue lines) and simulated ^{2}H spectrum of static C_2D_2 (red line).

sites with different binding strengths. This is in contrast to adsorbed CO_2, which displays a single peak at 2,338 cm^{-1} in the corresponding IR spectrum, indicating only a single type of adsorbed CO_2 molecule. The 3,209 cm^{-1} IR band decays slightly slower than the one at 3,309 cm^{-1} (Figure S63), also implying stronger C_2H_2 binding inside the HUMs. Higher relative intensity suggests that the stronger binding sites are more populated with C_2H_2. C_2H_2 is well-known to be relatively acidic (pK_a = 25) in the context of hydrocarbons and, thus, tends to form hydrogen bonding interactions, as observed in several MOMs.[56,61] Similar to the well-studied OH or N-H stretch vibrations,[62] the $\nu_{as}(C_2H_2)$ band undergoes a downward shift with respect to the gas phase value (at 3,287 cm^{-1}) upon forming intermolecular hydrogen bonds. The 3,209 cm^{-1} band represents a red-shift of 78 cm^{-1} and is consistent with the C_2H_2 binding site identified by simulation in Figure 2A. Overall, these *in situ* IR studies support the high adsorption selectivities for C_2H_2 over CO_2.

SOLID-STATE NMR SPECTROSCOPY

Solid-state NMR spectroscopy is a powerful technique for investigating the behavior of gaseous molecules adsorbed by porous materials.[63–65] To better understand the adsorptive properties of the HUMs studied herein, ^{13}C and ^{2}H static solid-state NMR experiments were conducted to directly monitor the behavior of $^{13}CO_2$ and C_2D_2 molecules adsorbed by **NbOFFIVE-3-Cu**. Figure S64 illustrates the ^{13}C NMR spectra of **NbOFFIVE-3-Cu** loaded with ^{13}C-labeled CO_2 at various temperatures. At 373 K, the spectrum contains a relatively sharp, symmetric peak at 125 ppm superimposed on a very broad profile. Comparing the spectrum of the HUM loaded with CO_2 with the spectrum of the empty HUM (Figure S64) indicates that the broad resonance in the spectrum of CO_2-loaded HUM likely originates from the linkers in the framework.

The position of the sharp signal indicates that this signal is from adsorbed CO_2. The sharpness of the resonance suggests that CO_2 molecules are rather mobile, implying weak interaction of CO_2 with the framework. Considering that ^{13}C enrichment of $^{13}CO_2$ is 99% and that the framework carbon atoms are at natural abundance (1.1%), the relative intensity of the two signals suggests that a relatively small amount of CO_2 was adsorbed by the HUM, which is consistent with the poor S/N ratio of the spectrum. Previous studies showed that for MOMs featuring good affinity toward CO_2, the ^{13}C spectra of adsorbed CO_2 usually exhibited a significantly higher intensity under similar adsorption conditions.[66–68] Overall, the ^{13}C NMR results indicate that **NbOFFIVE-3-Cu** does not adsorb CO_2 well. It is worth noting that the isotropic chemical shift of adsorbed CO_2 (125 ppm) is the same as that of CO_2 adsorbed in the diamagnetic MOMs,[66–68] suggesting the lack of a significant paramagnetic interaction between CO_2 and Cu(II). This is likely due to the distances between the carbon of CO_2 and nearby paramagnetic metal ions being rather long, i.e., 8.03, 7.16, 6.03, 6.31 Å (Figure S65), and that CO_2 is highly mobile. Similar situations have been observed in other Cu(II)-MOMs.[69,70] Upon lowering the temperature, the sharp characteristic peak of CO_2 gradually became broader and merged with the broad framework peak at 253 K. We attribute this to reduced mobility of CO_2 with decreasing temperature and chemical shift anisotropy, which is largely averaged by molecular motions at higher temperatures, becoming dominant and broadening the signal.

In contrast to the ^{13}C spectra of CO_2 loaded in **NbOFFIVE-3-Cu**, the ^{2}H static NMR spectra of C_2D_2 loaded in this HUM exhibited much stronger signals (Figure 5B), suggesting that **NbOFFIVE-3-Cu** has a higher affinity for C_2D_2 versus CO_2 under the same loading conditions. The ^{2}H static spectrum of adsorbed C_2D_2 at room temperature (293 K) exhibits a narrow pattern, suggesting a lack of significant paramagnetic interaction between the deuterons of C_2D_2 and Cu(II). This is consistent with the modeling study herein that indicates that two deuterium atoms in C_2D_2 are distant from nearby metal centers (5.1–6.4 Å). Inspection of the spectrum also reveals a well-defined line-shape with characteristic horns, shoulders, and "feet." However, such a pattern cannot be simulated by a single site. Instead, analytical simulation using WSolids software[71] revealed two components: a narrower component with a quadrupolar coupling constant (C_Q) of 43 kHz and a non-zero asymmetry parameter (η_Q) of 0.60 and a broader component with a C_Q of 65 kHz and η_Q of 0.0 (Figure S66B). The overall breadths of both patterns are markedly smaller than that of a static C_2D_2 (Figure 5B), which has a C_Q of 198 kHz and $\eta_Q = 0$.[72] This observation indicates that the first-order quadrupolar interaction is averaged by molecular motions experienced by C_2D_2. Seeing two separate patterns suggests that there are two types of C_2D_2 molecules in the unit cell and that they undergo different motions. In an attempt to identify the types of motions, dynamic simulations were performed by using the Express software package.[73] Based on the simulation results, we propose that the narrower pattern results from the C_2D_2 molecules that simultaneously undergo two motions: (1) localized wobbling motion modeled by a C_3 rotation and (2) a delocalized hopping about a C_2 axis (Figure S66D). A small portion (around 10%) of C_2D_2 only wobbles at its absorption site (Figure S66C), yielding a broader line. The spectra between 293 and 353 K look similar, implying that the motions are in the fast exchange regime. In the temperature range 273–173 K, the pattern for each spectrum is gradually broadened and loses its characteristic discontinuities. The overall breadth of the pattern at 173 K is much broader than at 293 K, inferring that C_2D_2 adsorbed by the HUM becomes much less mobile. However, it is difficult to analyze the spectra at low temperature. When loading was increased, the ^{2}H spectrum comprised a sharp peak in the middle and a broad component at the bottom (Figure S67). The sharp peak is likely due to the C_2D_2 molecules inside the pores undergoing fast exchange with the C_2D_2 outside the HUM. They do not interact with the framework strongly. The broad component is attributed to C_2D_2 molecules inside the pores that have strong interactions with the framework. The preference of C_2H_2 versus CO_2 indicated by solid-state NMR spectra further supports our results from single-component sorption, DCB experiments, molecular modeling, and *in situ* FTIR spectroscopic studies.

Accelerated stability tests[74] (313 K and 75% RH for 14 days) revealed that **NbOFFIVE-3-Ni**, **SIFSIX-21-Cu**, **TIFSIX-4-Cu**, and **NbOFFIVE-3-Cu** exhibit excellent hydrolytic stability (Figures S68C–S68F). Accelerated stability tests also revealed that both **SIFSIX-21-Ni** and **TIFSIX-4-Ni** (Figures S68A and S68B) underwent a phase change after exposure to humidity. Such phase changes have been observed in other HUMs and were attributed to inorganic pillar ligands being replaced by aqua ligands to afford corresponding **sql** networks.[75] **SIFSIX-21-Ni** was regenerated by heating the humidity-exposed sample at 358 K for 10 h in MeOH (Figure S69), whereas **TIFSIX-4-Ni** was regenerated by heating at 393 K (Figure S70).

Conclusions

In summary, six new HUMs, **SIFSIX-21-Ni**, **TIFSIX-4-Ni**, **NbOFFIVE-3-Ni**, **SIFSIX-21-Cu**, **TIFSIX-4-Cu**, and **NbOFFIVE-3-Cu**, were studied with respect to their ability to separate C_2H_2 from CO_2. Single-component sorption isotherms and equimolar C_2H_2/CO_2 binary gas mixture DCB experiments revealed that four of these HUMs, **SIFSIX-21-Ni**, **NbOFFIVE-3-Ni**, **TIFSIX-4-Cu**, and **NbOFFIVE-3-Cu**, break the trade-off between high adsorption capacities ≥ 3.5 mmol$\cdot$g^{-1} and high separation selectivities ≥ 5. **SIFSIX-21-Ni** outperformed all sorbents thanks to its benchmark separation selectivity (27.7) and high adsorption capacity (4 mmol$\cdot$g^{-1}). The key to the performance of **SIFSIX-21-Ni** is pore size and chemistry that enables relatively high surface area and strong C_2H_2 binding sites. This study once again highlights the ability of ultramicroporous sorbents to offer hitherto unattainable selectivity values for key binary gas separations.[25]

EXPERIMENTAL PROCEDURES

Resource availability

Lead contact

Further information and requests for resources should be directed to and will be fulfilled by the lead contact, Michael J. Zaworotko (xtal@ul.ie).

Materials availability

All materials generated in this study are available from the lead contact on request.

Data and code availability

The accession number for the crystal structures reported in this paper is Cambridge Crystallographic Data Centre, CCDC: 2052024, 2052025, 2052046, and 2052047.

SUPPLEMENTAL INFORMATION

Supplemental information can be found online at https://doi.org/10.1016/j.chempr.2021.07.007.

ACKNOWLEDGMENTS

M.J.Z. acknowledges the support of the Science Foundation Ireland (SFI awards 13/RP/B2549 and 16/IA/4624) and the European Research Council (award ADG 885695). T.P., K.A.F., and B.S. acknowledge the National Science Foundation (award no. DMR-1607989), including support from the Major Research

Instrumentation Program (award no. CHE-1531590). P.E.K gratefully acknowledges the MacDiarmid Institute for Advanced Materials and Nanotechnology. Computational resources were made available by an XSEDE grant (no. TG-DMR090028) awarded to B.S. and by Research Computing at the University of South Florida. We thank Matthew Mostrom for his assistance with calculating the partial charges. K.T. acknowledges the U. S. Department of Energy, Office of Science, Basic Energy Sciences under award no. DE-SC0019902. Y.H. thanks the Natural Science and Engineering Research Council (NSERC) of Canada for a Discovery Grant. M.V. acknowledges the Irish Centre for High-End Computing (ICHEC) for the provision of computational facilities and support.

AUTHOR CONTRIBUTIONS

Conceptualization, N.K., S.M., and M.J.Z.; methodology, N.K. and S.M.; validation, N.K., S.M., N.C.H.-R., and A.A.B.; investigation, N.K., S.M., N.C.H.-R., A.A.B., K.T., V.M., L.M.v.W., K.O., and K.M.P.; formal analysis, M.V., T.P., and K.A.F.; resources, N.H.R. and A.K.; data curation, N.K., S.M., A.A.B., M.V., T.P., and K.A.F.; writing – original draft, N.K., S.M., N.H.R., A.A.B., K.T., V.M., M.V., T.P., Y.H., and M.J.Z; writing – review & editing, all authors; funding acquisition, K.T., L.B., B.S., Y.H., P.E.K., and M.J.Z; supervision, M.J.Z.

DECLARATION OF INTERESTS

The authors declare no competing interests.

Received: January 10, 2021
Revised: February 25, 2021
Accepted: July 13, 2021
Published: August 10, 2021

REFERENCES

1. Pässler, P., Hefner, W., Buckl, K., Meinass, H., Meiswinkel, A., Wernicke, H.-J., Ebersberg, G., Müller, R., Bässler, J., Behringer, H., et al. (2011). Acetylene. In Ullmann's Encyclopedia of Industrial Chemistry (Wiley).

2. Himbert, G. (1996). Book review: modern acetylene chemistry. In Angew. Chem. Int. Ed. Engl., *35*, P.J. Stang and F. Diederich, eds., pp. 2154–2155.

3. Lower and upper explosive limits for flammable gases and vapors(LEL/UEL). https://www.chrysalisscientific.com/pg443-Lower-LEL-Upper-UEL-Explosive-Limits.pdf.

4. Gannon, R.E., Krukonis, V.J., and Schoenberg, T. (1970). Conversion of coal to acetylene in arc-heated hydrogen. Prod. R D *9*, 343–347.

5. Granada, A., Karra, S.B., and Senkan, S.M. (1987). Conversion of methane into acetylene and ethylene by the chlorine-catalyzed oxidative-pyrolysis (CCOP) process. 1. Oxidative pyrolysis of chloromethane. Ind. Eng. Chem. Res. *26*, 1901–1905.

6. Guo, C.J., Shen, D., and Bülow, M. (2001). 18-O-03 - Kinetic separation of binary mixtures of carbon dioxide and C2 hydrocarbons on modified LTA-type zeolites. Studies in Surface Science and Catalysis *135*, 144.

7. Arpe, H.-J., and Weissermel, K. (2003). Aromatics — production and conversion. In Industrial Organic Chemistry, Fourth Edition Edition (Wiley-VCH Press), pp. 313–336.

8. Thanh, C.N., Didillon, B., Sarrazin, P., and Cameron, S. (1996). Selective hydrogenation catalyst and a process using that catalyst. US patent US6054409A, filed December 20, 1996, and granted April 25, 2000.

9. Xu, G.L.F., Yang, Y., Hu, Y., Zhang, K., and Liu, W. (2014). An improved CO_2 separation and purification system based on cryogenic separation and distillation. Energies *7*, 3484–3502.

10. Nugent, P., Belmabkhout, Y., Burd, S.D., Cairns, A.J., Luebke, R., Forrest, K., et al. (2013). Porous materials with optimal adsorption thermodynamics and kinetics for CO_2 separation. Nature *495*, 80–84.

11. Mukherjee, S., Sikdar, N., O'Nolan, D., Franz, D.M., Gascón, V., Kumar, A., et al. (2019). Trace CO_2 capture by an ultramicroporous physisorbent with low water affinity. Sci. Adv. *5*, eaax9171.

12. Couck, S., Denayer, J.F.M., Baron, G.V., Rémy, T., Gascon, J., and Kapteijn, F. (2009). An amine-functionalized MIL-53 metal−organic framework with large separation power for CO_2 and CH_4. J. Am. Chem. Soc. *131*, 6326–6327.

13. Cui, X., Chen, K., Xing, H., Yang, Q., Krishna, R., Bao, Z., Wu, H., Zhou, W., Dong, X., Han, Y., et al. (2016). Pore chemistry and size control in hybrid porous materials for acetylene capture from ethylene. Science *353*, 141–144.

14. Li, B., Cui, X., O'Nolan, D., Wen, H.-M., Jiang, M., Krishna, R., Wu, H., Lin, R.-B., Chen, Y.-S., Yuan, D., et al. (2017). An ideal molecular sieve for acetylene removal from ethylene with record selectivity and productivity. Adv. Mater. *29*, 1704210.

15. Chen, C., Wei, Z., Pham, T., Lan, P.C., Zhang, L., Forrest, K.A., Chen, S., Al-Enizi, A.M., Nafady, A., Su, C., et al. (2021). Nanospace engineering of metal–organic frameworks through dynamic spacer installation of multifunctionalities for efficient separation of ethane from ethane/ethylene mixtures. Angew. Chem. Int. Ed. *60*, 9680–9685.

16. Lin, R.-B., Xiang, S., Zhou, W., and Chen, B. (2020). Microporous metal-organic framework materials for gas separation. Chem *6*, 337–363.

17. Matsuda, R., Kitaura, R., Kitagawa, S., Kubota, Y., Belosludov, R.V., Kobayashi, T.C., Sakamoto, H., Chiba, T., Takata, M., Kawazoe, Y., and Mita, Y. (2005). Highly controlled acetylene accommodation in a metal–organic microporous material. Nature *436*, 238–241.

18. Li, J.R., Kuppler, R.J., and Zhou, H.C. (2009). Selective gas adsorption and separation in

metal–organic frameworks. Chem. Soc. Rev. *38*, 1477–1504.

19. Sircar, S. (2006). Basic Research needs for design of adsorptive gas separation processes. Ind. Eng. Chem. Res. *45*, 5435–5448.

20. Cui, W.G., Hu, T.L., and Bu, X.H. (2020). Metal–organic framework materials for the separation and purification of light hydrocarbons. Adv. Mater. *32*, e1806445.

21. Perry, J.J., Perman, J.A., and Zaworotko, M.J. (2009). Design and synthesis of metal–organic frameworks using metal–organic polyhedra as supermolecular building blocks. Chem. Soc. Rev. *38*, 1400–1417.

22. MacGillivray, R. (2010). Metal-Organic Frameworks: Design and Application (John Wiley & Sons).

23. Schröder, M., and Banerjee, M. (2009). Functional Metal-Organic Frameworks: Gas Storage, Separation and Catalysis (Springer-Verlag).

24. Kitagawa, S., Kitaura, R., and Noro, S.-i. (2004). Functional porous coordination polymers. Angew. Chem. Int. Ed. Engl. *43*, 2334–2375.

25. Mukherjee, S., Sensharma, D., Chen, K.J., and Zaworotko, M.J. (2020). Crystal engineering of porous coordination networks to enable separation of C2 hydrocarbons. Chem. Commun. (Camb) *56*, 10419–10441.

26. CCDC (2020). New data and improvements - 2020.3 CSD data release. https://www.ccdc.cam.ac.uk/Community/blog/New_Data_and_improvements_2020.3_blog/.

27. Niu, Z., Cui, X., Pham, T., Verma, G., Lan, P.C., Shan, C., et al. (2021). A MOF-based ultra-strong acetylene nano-trap for highly efficient C_2H_2/CO_2 separation. Angew. Chem. Int. Ed. Engl. *60*, 5283–5288.

28. Di, Z., Liu, C., Pang, J., Chen, C., Hu, F., Yuan, D., et al. (2021). Cage-like porous materials with simultaneous high C_2H_2 storage and excellent C_2H_2/CO_2 separation performance. Angew. Chem. Int. Ed. Engl. *60*, 10828–10832.

29. Li, H., Liu, C., Chen, C., Di, Z., Yuan, D., Pang, J., Wei, W., Wu, M., and Hong, M. (2021). An unprecedented pillar–cage fluorinated hybrid porous framework with highly efficient acetylene storage and separation. Angew. Chem. Int. Ed. Engl. *60*, 7547–7552.

30. Mukherjee, S., He, Y., Franz, D., Wang, S.Q., Xian, W.R., Bezrukov, A.A., et al. (2020). Halogen–C_2H_2 binding in ultramicroporous metal–organic frameworks (MOFs) for benchmark C_2H_2/CO_2 separation selectivity. Chem. Eur. J. *26*, 4923–4929.

31. Lee, J., Chuah, C.Y., Kim, J., Kim, Y., Ko, N., Seo, Y., Kim, K., Bae, T.H., and Lee, E. (2018). Separation of acetylene from carbon dioxide and ethylene by a water-stable microporous metal–organic framework with aligned imidazolium groups inside the channels. Angew. Chem. Int. Ed. Engl. *57*, 7869–7873.

32. Peng, Y.L., Pham, T., Li, P., Wang, T., Chen, Y., Chen, K.J., Forrest, K.A., Space, B., Cheng, P., Zaworotko, M.J., and Zhang, Z. (2018). Robust ultramicroporous metal–organic frameworks with benchmark affinity for acetylene. Angew. Chem. Int. Ed. Engl. *57*, 10971–10975.

33. Yao, Z., Zhang, Z., Liu, L., Li, Z., Zhou, W., Zhao, Y., et al. (2016). Extraordinary separation of acetylene-containing mixtures with microporous metal–organic frameworks with open O donor sites and tunable robustness through control of the helical chain secondary building units. Chem. Eur. J. *22*, 5676–5683.

34. Ye, Y., Chen, S., Chen, L., Huang, J., Ma, Z., Li, Z., Yao, Z., Zhang, J., Zhang, Z., and Xiang, S. (2018). Additive-induced supramolecular isomerism and enhancement of robustness in Co(II)-based MOFs for efficiently trapping acetylene from acetylene-containing mixtures. ACS Appl. Mater. Interfaces *10*, 30912–30918.

35. Li, P., He, Y., Zhao, Y., Weng, L., Wang, H., Krishna, R., et al. (2015). A rod-packing microporous hydrogen-bonded organic framework for highly selective separation of C_2H_2/CO_2 at room temperature. Angew. Chem. Int. Ed. Engl. *54*, 574–577.

36. Liu, L., Yao, Z., Ye, Y., Yang, Y., Lin, Q., Zhang, Z., et al. (2020). Integrating the pillared-layer strategy and pore-space partition method to construct multicomponent MOFs for C_2H_2/CO_2 separation. J. Am. Chem. Soc. *142*, 9258–9266.

37. Li, Y.P., Wang, Y., Xue, Y.Y., Li, H.P., Zhai, Q.G., Li, S.N., Jiang, Y.C., Hu, M.C., and Bu, X. (2019). Ultramicroporous building units as a path to bi-microporous metal–organic frameworks with high acetylene storage and separation performance. Angew. Chem. Int. Ed. Engl. *58*, 13590–13595.

38. Liu, R., Liu, Q.Y., Krishna, R., Wang, W., He, C.T., and Wang, Y.L. (2019). Water-stable europium 1,3,6,8-Tetrakis(4-carboxylphenyl) pyrene framework for efficient C_2H_2/CO_2 separation. Inorg. Chem. *58*, 5089–5095.

39. Liu, L., Yao, Z., Ye, Y., Chen, L., Lin, Q., Yang, Y., Zhang, Z., and Xiang, S. (2018). Robustness, selective gas separation, and nitrobenzene sensing on two isomers of cadmium metal–organic frameworks containing various metal–O–metal chains. Inorg. Chem. *57*, 12961–12968.

40. Gao, J., Qian, X., Lin, R.-B., Krishna, R., Wu, H., Zhou, W., et al. (2020). Mixed metal–organic framework with multiple binding sites for efficient C_2H_2/CO_2 separation. Angew. Chem. Int. Ed. *59*, 4396–4400.

41. Luo, F., Yan, C., Dang, L., Krishna, R., Zhou, W., Wu, H., Dong, X., Han, Y., Hu, T.L., O'Keeffe, M., et al. (2016). UTSA-74: a MOF-74 isomer with two accessible binding sites per metal center for zhighly selective gas separation. J. Am. Chem. Soc. *138*, 5678–5684.

42. Kumar, N., Mukherjee, S., Bezrukov, A.A., Vandichel, M., Shivanna, M., Sensharma, D., et al. (2020). A square lattice topology coordination network that exhibits highly selective C_2H_2/CO_2 separation performance. SmartMat *1*, e1008.

43. Mukherjee, S., Kumar, A., and Zaworotko, M.J. (2019). 2 - Metal-organic framework based carbon capture and purification technologies for clean environment. In Metal-Organic Frameworks (MOFs) for Environmental Applications, S.K. Ghosh, ed. (Elsevier), pp. 5–61.

44. Oschatz, M., and Antonietti, M. (2018). A search for selectivity to enable CO_2 capture with porous adsorbents. Energy Environ. Sci. *11*, 57–70.

45. Scott, H.S., Bajpai, A., Chen, K.-J., Pham, T., Space, B., Perry, J.J., et al. (2015). Novel mode of 2-fold interpenetration observed in a primitive cubic network of formula $[Ni(1,2\text{-}bis(4\text{-}pyridyl)acetylene)_2(Cr_2O_7)]n$. Chem. Commun. *51*, 14832–14835.

46. Bhatt, P.M., Belmabkhout, Y., Cadiau, A., Adil, K., Shekhah, O., Shkurenko, A., et al. (2016). A fine-tuned fluorinated MOF addresses the needs for trace CO_2 removal and air capture using physisorption. J. Am. Chem. Soc. *138*, 9301–9307.

47. Mukherjee, S., and Zaworotko, M.J. (2020). Crystal engineering of hybrid coordination networks: From form to function. Trends in Chemistry *2*, 506–518.

48. Howarth, A.J., Peters, A.W., Vermeulen, N.A., Wang, T.C., Hupp, J.T., and Farha, O.K. (2017). Best practices for the synthesis, activation, and characterization of metal–organic frameworks. Chem. Mater. *29*, 26–39.

49. Myers, A.L., and Prausnitz, J.M. (1965). Thermodynamics of mixed-gas adsorption. AIChE J *11*, 121–127.

50. Qazvini, O.T., Babarao, R., and Telfer, S.G. (2019). Multipurpose metal–organic framework for the adsorption of acetylene: ethylene purification and carbon dioxide removal. Chem. Mater. *31*, 4919–4926.

51. Duan, X., Zhang, Q., Cai, J., Yang, Y., Cui, Y., He, Y., Wu, C., Krishna, R., Chen, B., and Qian, G. (2014). A new metal–organic framework with potential for adsorptive separation of methane from carbon dioxide, acetylene, ethylene, and ethane established by simulated breakthrough experiments. J. Mater. Chem. A *2*, 2628–2633.

52. Wen, H.M., Liao, C., Li, L., Yang, L., Wang, J., Huang, L., et al. (2019). Reversing C_2H_2–CO_2 adsorption selectivity in an ultramicroporous metal–organic framework platform. Chem. Commun. (Camb) *55*, 11354–11357.

53. Chen, K.-J., Scott, H.S., Madden, D.G., Pham, T., Kumar, A., Bajpai, A., et al. (2016). Benchmark C_2H_2/CO_2 and CO_2/C_2H_2 separation by two closely related hybrid ultramicroporous materials. Chem *1*, 753–765.

54. Yoon, J.W., Lee, J.S., Lee, S., Cho, K.H., Hwang, Y.K., Daturi, M., et al. (2015). Adsorptive separation of acetylene from light hydrocarbons by mesoporous iron Trimesate MIL-100(Fe). Chem. Eur. J. *21*, 18431–18438.

55. Wellendorff, J., Lundgaard, K.T., Møgelhøj, A., Petzold, V., Landis, D.D., Nørskov, J.K., Bligaard, T., and Jacobsen, K.W. (2012). Density functionals for surface science: exchange-correlation model development with Bayesian error estimation. Phys. Rev. B *85*, 235149.

56. Chen, K.J., Madden, D.G., Mukherjee, S., Pham, T., Forrest, K.A., Kumar, A., Space, B., Kong, J., Zhang, Q.Y., and Zaworotko, M.J. (2019). Synergistic sorbent separation for one-step ethylene purification from a four-component mixture. Science *366*, 241–246.

57. Rajendran, A., Kariwala, V., and Farooq, S. (2008). Correction procedures for extra-column effects in dynamic column breakthrough experiments. Chem. Eng. Sci. *63*, 2696–2706.

58. Shen, J., He, X., Ke, T., Krishna, R., van Baten, J.M.V., Chen, R., Bao, Z., Xing, H., Dincǎ, M., Zhang, Z., et al. (2020). Simultaneous interlayer and intralayer space control in two-dimensional metal−organic frameworks for acetylene/ethylene separation. Nat. Commun. *11*, 6259.

59. Zhang, Z., Tan, B., Wang, P., Cui, X., and Xing, H. (2020). Highly efficient separation of linear and branched C4 isomers with a tailor-made metal–organic framework. AIChE J *66*, e16236.

60. Swoboda, A.R., and Kunze, G.W. (1964). Infrared study of pyridine adsorbed on montmorillonite surfaces. Clays Clay Miner *13*, 277–288.

61. Nijem, N., Wu, H.H., Canepa, P., Marti, A., Balkus, K.J., Thonhauser, T., Li, J., and Chabal, Y.J. (2012). Tuning the gate opening pressure of metal-organic frameworks (MOFs) for the selective separation of hydrocarbons. J. Am. Chem. Soc. *134*, 15201–15204.

62. Marechal, Y. (2007). The Hydrogen Bond and the Water Molecule: the Physics and Chemistry of Water, Aqueous and Bio-Media (Elsevier Science).

63. Wong, Y.T.A., Martins, V., Lucier, B.E.G., and Huang, Y. (2019). Solid-state NMR spectroscopy: a powerful technique to directly study small gas molecules adsorbed in metal-organic frameworks. Chem. Eur. J. *25*, 1848–1853.

64. Bertmer, M. (2020). Solid-state NMR of small molecule adsorption in metal–organic frameworks (MOFs). Annu. Rep. NMR Spectrosc. *101*, 1–64.

65. Witherspoon, V.J., Xu, J., and Reimer, J.A. (2018). Solid-state NMR investigations of carbon dioxide gas in metal–organic frameworks: insights into molecular motion and adsorptive behavior. Chem. Rev. *118*, 10033–10048.

66. Zhang, Y., Lucier, B.E.G., and Huang, Y. (2016). Deducing CO_2 motion, adsorption locations and binding strengths in a flexible metal–organic framework without open metal sites. Phys. Chem. Chem. Phys. *18*, 8327–8341.

67. Lu, Y., Lucier, B.E.G., Zhang, Y., Ren, P., Zheng, A., and Huang, Y. (2017). Sizable dynamics in small pores: CO_2 location and motion in the α-Mg formate metal–organic framework. Phys. Chem. Chem. Phys. *19*, 6130–6141.

68. Wu, B., Wong, Y.T.A., Lucier, B.E.G., Boyle, P.D., and Huang, Y. (2019). Exploring host-guest interactions in the α-$Zn_3(HCOO)_6$ metal-organic framework. ACS Omega *4*, 4000–4011.

69. Chen, M., Chen, S., Chen, W., Lucier, B.E.G., Zhang, Y., Zheng, A., and Huang, Y. (2018). Analyzing gas adsorption in an amide-functionalized metal organic framework: are the carbonyl or amine groups responsible? Chem. Mater. *30*, 3613–3617.

70. Gul-E-Noor, F., Mendt, M., Michel, D., Pöppl, A., Krautscheid, H., Haase, J., et al. (2013). Adsorption of Small Molecules on $Cu_3(btc)_2$ and $Cu_{3-x}Zn_x(btc)_2$ Metal–Organic Frameworks (MOF) As Studied by Solid-State NMR. J. Phys. Chem. C *117*, 7703–7712.

71. Eichele, K. (2011). WSolids1, Version 1.20.15 (Tübingen, Germany: Universität Tübingen). http://anorganik.uni-tuebingen.de/klaus/soft/wsolids1/wsolids1.pdf.

72. Millett, F.S., and Dailey, B.P. (1972). NMR determination of some deuterium quadrupole coupling constants in nematic solutions. J. Chem. Phys. *56*, 3249–3256.

73. Vold, R.L., and Hoatson, G.L. (2009). Effects of jump dynamics on solid state nuclear magnetic resonance line shapes and spin relaxation times. J. Magn. Reson. *198*, 57–72.

74. Waterman, K.C. (2009). Understanding and predicting pharmaceutical product shelf-life. In Handbook of Stability Testing in Pharmaceutical Development: Regulations, Methodologies, and Best Practices, K. Huynh-Ba, ed. (Springer), pp. 115–135.

75. O'Nolan, D., Kumar, A., and Zaworotko, M.J. (2017). Water vapor sorption in hybrid pillared square grid materials. J. Am. Chem. Soc. *139*, 8508–8513.

Chem, Volume *7*

Supplemental information

Breaking the trade-off between selectivity and adsorption capacity for gas separation

Naveen Kumar, Soumya Mukherjee, Nathan C. Harvey-Reid, Andrey A. Bezrukov, Kui Tan, Vinicius Martins, Matthias Vandichel, Tony Pham, Lisa M. van Wyk, Kolade Oyekan, Amrit Kumar, Katherine A. Forrest, Komal M. Patil, Leonard J. Barbour, Brian Space, Yining Huang, Paul E. Kruger, and Michael J. Zaworotko

Supplemental Information for

Breaking the trade-off between selectivity and adsorption capacity for C_2H_2/CO_2 separation

Naveen Kumar,[1,†] Soumya Mukherjee,[1,†] Nathan C. Harvey-Reid,[2] Andrey A. Bezrukov,[1] Kui Tan,[3] Vinicius Martins,[4] Matthias Vandichel,[1] Tony Pham,[5] Lisa M. van Wyk,[6] Kolade Oyekan,[3] Amrit Kumar,[1] Katherine A. Forrest,[5] Komal M. Patil,[2] Leonard J. Barbour,[6] Brian Space,[5] Yining Huang,[4] Paul E. Kruger,[2] and Michael J. Zaworotko[1,]*
*correspondence: xtal@ul.ie
[†]These authors contributed equally.

Materials and Methods S4
Supplemental Text S8
Figures S1 to S73
Figure S1. PXRD profiles of **SIFSIX-21-Ni, TIFSIX-4-Ni and NbOFFIVE-3-Ni**, validating phase purity S20
Figure S2. PXRD profiles of **SIFSIX-21-Cu, TIFSIX-4-Cu** and **NbOFFIVE-3-Cu**, validating phase purity S20
Figure S3. Pawley profile fit of the PXRD patterns of **NbOFFIVE-3-Ni** S21
Figure S4. Pawley profile fit of the PXRD patterns of **NbOFFIVE-3-Cu** S21
Figure S5. Variable temperature PXRD patterns of **SIFSIX-21-Ni** S22
Figure S6. Variable temperature PXRD patterns of **TIFSIX-4-Ni** S22
Figure S7. Variable temperature PXRD patterns of **NbOFFIVE-3-Ni** S23
Figure S8. Variable temperature PXRD patterns of **SIFSIX-21-Cu** S23
Figure S9. Variable temperature PXRD patterns of **TIFSIX-4-Cu** S24
Figure S10. Variable temperature PXRD patterns of **NbOFFIVE-3-Cu** S24
Figure S11. *In situ* PXRD patterns of **SIFSIX-21-Ni** on C_2H_2 dosing S25
Figure S12. *In situ* PXRD patterns of **SIFSIX-21-Cu** on C_2H_2 dosing S25
Figure S13. Thermogravimetric analysis profiles of the as-synthesised **SIFSIX-21-Ni, TIFSIX-4-Ni** and **NbOFFIVE-3-Ni** S26
Figure S14. Thermogravimetric analysis profiles of the as-synthesised **SIFSIX-21-Cu, TIFSIX-4-Cu** and **NbOFFIVE-3-Cu** S26
Figure S15. Low temperature sorption isotherms for **SIFSIX-21-Ni** S27
Figure S16. C_2H_2 and CO_2 adsorption isotherms for **SIFSIX-21-Ni** S27
Figure S17. Low temperature sorption isotherms for **TIFSIX-4-Ni** S28
Figure S18. C_2H_2 and CO_2 adsorption isotherms for **TIFSIX-4-Ni** S28
Figure S19. Low temperature sorption isotherms for **NbOFFIVE-3-Ni** S29
Figure S20. C_2H_2 and CO_2 adsorption isotherms for **NbOFFIVE-3-Ni** S29
Figure S21. Low temperature sorption isotherms for **SIFSIX-21-Cu** S30
Figure S22. C_2H_2 and CO_2 adsorption isotherms for **SIFSIX-21-Cu** S30
Figure S23. Low temperature sorption isotherms for **TIFSIX-4-Cu** S31
Figure S24. C_2H_2 and CO_2 adsorption isotherms for **TIFSIX-4-Cu** S31
Figure S25. Low temperature sorption isotherms for **NbOFFIVE-3-Cu** S32
Figure S26. C_2H_2 and CO_2 adsorption isotherms for **NbOFFIVE-3-Cu** S32

Figure S27. Isosteric enthalpies of adsorption for **SIFSIX-21-Ni** S33
Figure S28. Isosteric enthalpies of adsorption for **TIFSIX-4-Ni** S33
Figure S29. Isosteric enthalpies of adsorption for **NbOFFIVE-3-Ni** S34
Figure S30. Isosteric enthalpies of adsorption for **SIFSIX-21-Cu** S34
Figure S31. Isosteric enthalpies of adsorption for **TIFSIX-4-Cu** S35
Figure S32. Isosteric enthalpies of adsorption for **NbOFFIVE-3-Cu** S35
Figure S33. Virial Fitting of the CO_2 isotherms for **SIFSIX-21-Ni** S36
Figure S34. Virial Fitting of the C_2H_2 isotherms for **SIFSIX-21-Ni** S36
Figure S35. Virial Fitting of the CO_2 isotherms for **TIFSIX-4-Ni** S37
Figure S36. Virial Fitting of the C_2H_2 isotherms for **TIFSIX-4-Ni** S37
Figure S37. Virial Fitting of the CO_2 isotherms for **NbOFFIVE-3-Ni** S38
Figure S38. Virial Fitting of the C_2H_2 isotherms for **NbOFFIVE-3-Ni** S38
Figure S39. Virial Fitting of the CO_2 isotherms for **SIFSIX-21-Cu** S39
Figure S40. Virial Fitting of the C_2H_2 isotherms for **SIFSIX-21-Cu** S39
Figure S41. Virial Fitting of the CO_2 isotherms for **TIFSIX-4-Cu** S40
Figure S42. Virial Fitting of the C_2H_2 isotherms for **TIFSIX-4-Cu** S40
Figure S43. Virial Fitting of the CO_2 isotherms for **NbOFFIVE-3-Cu** S41
Figure S44. Virial Fitting of the C_2H_2 isotherms for **NbOFFIVE-3-Cu** S41
Figure S45. C_2H_2/CO_2 selectivity calculated by IAST for **SIFSIX-21-Ni** S42
Figure S46. C_2H_2/CO_2 selectivity calculated by IAST for **TIFSIX-4-Ni** S42
Figure S47. C_2H_2/CO_2 selectivity calculated by IAST for **NbOFFIVE-3-Ni** S43
Figure S48. C_2H_2/CO_2 selectivity calculated by IAST for **SIFSIX-21-Cu** S43
Figure S49. C_2H_2/CO_2 selectivity calculated by IAST for **TIFSIX-4-Cu** S44
Figure S50. C_2H_2/CO_2 selectivity calculated by IAST for **SIFSIX-21-Cu** S44
Figure S51. Mixed isotherms for Ni HUM series S45
Figure S52. Mixed isotherms for Cu HUM series S46
Figure S53. C_2H_2 and CO_2 binding sites for **SIFSIX-21-Ni** S47
Figure S54. Sorption kinetics for C_2H_2 and CO_2 for Ni HUM series S48
Figure S55. Sorption kinetics for C_2H_2 and CO_2 for Cu HUM series S48
Figure S56. Schematic of dynamic column breakthrough experimental setup S49
Figure S57. Temperature programmed desorption experiments S49
Figure S58. Comparison of $Q_{st}(C_2H_2)$ for C_2H_2/CO_2 separating MOMs S50
Figure S59. Comparison of $\Delta Q_{st}(C_2H_2/CO_2)$ for C_2H_2/CO_2 separating MOMs S50
Figure S60. Difference IR spectra for CO_2 and C_2H_2 adsorption in **SIFSIX-21-Ni** S51
Figure S61. IR spectra of activated **NbOFFIVE-3-Cu** and **SIFSIX-21-Ni** S51
Figure S62. Theoretical IR spectrum of pypz from DFT calculation S52
Figure S63. Evolution of the $\nu_{as}(C_2H_2)$ bands in **NbOFFIVE-3-Cu** S52
Figure S64. ^{13}C static NMR spectra of $^{13}CO_2$ adsorbed in **NbOFFIVE-3-Cu** S53
Figure S65. Modelled structures to illustrate distance between CO_2 and C_2H_2 molecules from the metal centres S53
Figure S66. Experimental and simulated ^2H static spectra of C_2D_2 absorbed in **NbOFFIVE-3-Cu** S54
Figure S67. A comparison of experimental 2H static NMR spectra of **NbOFFIVE-3-Cu** loaded with 0.4 and 0.8 eq. and 0.4 eq. C_2D_2 at room temperature S55
Figure S68. PXRD patterns of humidity exposed samples S55
Figure S69. PXRD patterns of regenerated samples of **SIFSIX-21-Ni** S56

Figure S70. PXRD patterns of regenerated samples of **TIFSIX-4-Ni** S56
Figure S71. Supplemental figures of **TIFSIX-4-Ni** S57
Figure S72. Supplemental figures of **SIFSIX-21-Cu** S57
Figure S73. Supplemental figures of **TIFSIX-4-Cu** S58

Tables S1-S4

Table S1. Structural information, sorption data and C_2H_2/CO_2 selectivities S59
Table S2. Crystallographic data for **SIFSIX-21-Ni**, **TIFSIX-4-Ni**, **SIFSIX-21-Cu** and **TIFSIX-4-Cu** S61
Table S3. DSLF fitting parameters summary for C_2H_2 and CO_2 sorption S62
Table S4. Calculated averaged total potential energies (in kJ mol^{-1}) for a single C_2H_2 and CO_2 molecule S63

References S64

Materials and Methods.

Starting materials, reagents and solvents were purchased from commercial sources (Sigma-Aldrich, TCI Europe N.V., AK Scientific Inc. USA) and used without further purification.

Powder X-ray Diffraction (PXRD). Diffractograms were recorded using a PANalytical Empyrean™ diffractometer equipped with a PIXcel^{3D} detector operating in scanning line detector mode with an active length of 4 utilizing 255 channels. The diffractometer is outfitted with an Empyrean Cu LFF (long fine-focus) HR (9430 033 7310x) tube operated at 40 kV and 40 mA and CuK$_{\alpha}$ radiation (λ_{α} = 1.540598 Å) was used for diffraction experiments. Continuous scanning mode with the goniometer in the theta-theta orientation was used to collect the data. Incident beam optics included the Fixed Divergences slit with anti-scatter slit PreFIX module, with a 1/8° divergence slit and a 1/4° anti-scatter slit, as well as a 10 mm fixed incident beam mask and a Soller slit (0.04 rad). Divergent beam optics included a P7.5 anti-scatter slit, a Soller slit (0.04 rad) and a Ni-β filter. In a typical experiment, 25 mg of sample was dried, ground into a fine powder and was loaded on a zero background silicon disks. The data was collected from 5°–40° (2θ) with a step-size of 0.0131303° and a scan time of 30 seconds per step. Crude data were analyzed using the X'Pert HighScore Plus™ software V 4.1 (PANalytical, The Netherlands).

Variable Temperature Powder X-ray Diffraction (VT-PXRD). Diffractograms at different temperature were recorded using a PANalytical X'Pert Pro-MPD diffractometer equipped with a PIXcel3D detector operating in scanning line detector mode with an active length of 4 utilizing 255 channels. Anton Paar TTK 450 stage coupled with the Anton Paar TCU 110 Temperature Control Unit was used to record the variable temperature diffractograms. The diffractometer is outfitted with an Empyrean Cu LFF (long fine-focus) HR (9430 033 7300x) tube operated at 40 kV and 40 mA and CuKα radiation (λα = 1.54056 Å) was used for diffraction experiments. Continuous scanning mode with the goniometer in the theta-theta orientation was used to collect the data. Incident beam optics included the Fixed Divergences slit, with a 1/4° divergence slit and a Soller slit (0.04 rad). Divergent beam optics included a P7.5 anti-scatter slit, a Soller slit (0.04 rad), and a Ni-β filter. In a typical experiment, 20 mg of sample was dried, ground into a fine powder and was loaded on a zero background sample holder made for Anton Paar TTK 450 chamber. The data was collected from 5°–45° (2θ) with a step-size of 0.0167113° and a scan time of 50 seconds per step. Crude data were analyzed using the X'Pert HighScore Plus™ software V 4.1 (PANalytical, The Netherlands).

Thermogravimetric Analysis (TGA). Thermograms were recorded under nitrogen using TGA instrument TA Q50 V20.13 Build 39. Platinum pans and a flow rate of 60 cm^3 min^{-1} for the nitrogen gas were used for the experiments. The data was collected in the High Resolution Dynamic mode with a sensitivity of 1.0, a resolution of 4.0 and a temperature ramp of 20 °C min^{-1} up to 550 °C. The data was evaluated using the T.A. Universal Analysis suite for Windows XP/Vista Version 4.5A.

Gas Sorption Measurements. For gas sorption experiments, ultrahigh-purity gases were used as received from BOC Gases Ireland: research-grade He (99.999%), CO_2 (99.995%), C_2H_2 (98.5%) and N_2 (99.998%). Adsorption experiments (up to 1 bar) for 77 K N_2 and 195 K CO_2 were performed on Micromeritics Tristar II 3030. Micromeritics 3Flex surface area and pore size analyser 3500 was used for collecting the 273 and 298 K sorption isotherms for C_2H_2 and CO_2. Before sorption measurements, activation of all six different **HUMs** was achieved by degassing the air-dried samples on a SmartVacPrep™ using dynamic vacuum and heating for 8 h (each sample heated from RT to 333 K with a ramp rate of 5 °C). Brunauer-Emmett-Teller (BET) surface areas were determined from the CO_2 and N_2 adsorption isotherms at 195 K and 77 K respectively, using the Micromeritics Microactive software. About 100 mg of activated samples were used for the measurements. A Julabo temperature controller was used to maintain a constant temperature in the bath throughout the experiment. The bath temperatures of 273 and 298 K were precisely controlled with a Julabo ME (v.2) recirculating control system containing a mixture of ethylene glycol and water. The low temperature at 77 K and 195 K were controlled by a 4 L Dewar filled with liquid N_2 and dry ice/acetone, respectively. At every interval of two independent isotherms recorded for any sorbent, samples were regenerated by degassing over 5 h under high vacuum at 333 K, before commencing the next sorption experiment.

Accelerated Stability Protocol. In a typical experiment, as followed by the pharmaceutical industries,[1] microcrystalline samples of each of the HUMs was exposed to 313 K and 75 % RH for 1, 7 and 14 days (d) in a desiccator (corresponding to 4 d, 1 month and 2 months shelf-life, respectively). These conditions were achieved by using a supersaturated aqueous solution of NaCl maintained at 313 K in a closed desiccator. After 1, 7 and 14 d, sample aliquots were removed from desiccator and characterized by PXRD measurements in order to detect signs the sample which may have been affected by humidity.

Single-gas sorption cycling test. Gravimetric uptakes were recorded under pure C_2H_2 gas, using TGA instrument TA Q50 V20.13 Build 39. Platinum pans and gas flow rates of 10 cm^3/min were used in these experiments. Desorption at 60 °C was performed under N_2 flow of 20 cm^3/min. The data was collected in the High Resolution Dynamic mode with a sensitivity of 1.0, a resolution of 4.0 and the weight changes during C_2H_2 gas adsorption step were monitored under isothermal condition at 60 °C. The data was evaluated using the T.A. Universal Analysis suite for Windows

XP/Vista Version 4.5A. The flowrates of all these sorbates were monitored by pre-calibrated Bronkhorst Mass Flow Controllers.

Breakthrough Experiments. In typical breakthrough experiments, ~ 0.5 g of pre-activated **HUMs** were placed in quartz tubing (8 mm diameter; 8 mm x 6 mm x 400 mm) to form fixed beds. First, the adsorbent bed was purged under a 30 cm^3 min^{-1} flow of He gas at 333 K for 30 min prior to breakthrough experiment. Upon cooling to room temperature, the gas flow was switched to the desired C_2H_2/CO_2 gas mixture compositions (2:1 and 1:1 respectively), maintained at a total flow rate of 1.0 cm^3 min^{-1}. Herein, 2:1 and 1:1 C_2H_2/CO_2 binary breakthrough experiments were conducted at 298 K for all six **HUMs**. The outlet composition was continuously monitored by a Shimadzu Nexis GC-2030 gas chromatograph until complete breakthrough was achieved. For temperature programmed desorption (TPD), post-breakthrough saturated sorbent beds were heated at a constant rate to 60 °C under He flow, 20 cm^3min^{-1}. The desorbed gases were monitored continuously.

Supplemental Text

Single Crystal X-ray Diffraction.

Single crystal X-ray diffraction data of all the crystals were collected on a Bruker Quest diffractometer equipped with a IμS microfocus X-ray source (Cu Kα, λ = 1.54178 Å; Mo *K*α, (λ = 0.71073 Å) and CMOS detector. APEX3 was used for collecting, indexing, integrating and scaling the data.[2] Open-flow nitrogen attachment with Oxford Cryosystem was used for low temperature measurements. Absorption correction was performed by multi-scan method.[3] Space groups were determined using XPREP[4] as implemented in APEX3. All the scaled data were solved using intrinsic phasing method (XT)[5] and refined on F^2 using SHELXL[6] inbuilt in OLEX2 v1.2 (2009) program.[7] All non-hydrogen atoms present in the frameworks were refined anisotropically. Hydrogen atoms were located at idealized positions from the molecular geometry and refined isotropically with thermal parameters based on the equivalent displacement parameters of their carriers. The reported structures were refined from twin crystals. Each of the crystals of **SIFSIX-21-Ni**, **TIFSIX-4-Ni**, **SIFSIX-21-Cu** and **TIFSIX-4-Cu** was revealed as a two-domain twin. Appropriate PART instructions were used to model framework disorder in these structures. Where needed, especially for disordered sections of the frameworks, restraints (SIMU, DELU, ISOR, RIGU) were used to ensure proper geometry of the molecules and to allow anisotropic refinement of non-hydrogen atoms. Crystallographic data for all the HUMs reported in this paper, are summarised in Table S2. Crystal structures are deposited to the Cambridge Crystallographic Data Centre (CCDC 2052024-2052025; 2052046-2052047).

Adsorption Energy Calculations.

Except the six HUMs studied herein, other *Q_{st}* plots and associated parameters were obtained from data extraction using WebPlotDigitizer.[8]

A virial-type expression of the below form was used to fit the combined 273 and 298 K isotherm data of C_2H_2 and CO_2 for all six **HUMs**, where P is the pressure described in Pa, *N* is the adsorbed amount in mmol g^{-1}, T is the temperature in K, a_i and b_i are virial coefficients and *m* and *n* are the number of coefficients used to describe the isotherms. Q_{st} is the coverage-dependent enthalpy of adsorption and R is the universal gas constant. All fitting was performed using Origin Pro 8.[9] Fitting parameters thus obtained for the six **HUMs** can be found in Figures S33–S44.

$$\ln P = \ln N + \sum_{i=0}^{m} a_i N_i + \sum_{i=0}^{n} \binom{n}{k} b_i N_i$$

Q_{st} was calculated from the virial model using the equation below.

$$-Q_{st} = -R \sum_{i=0}^{m} a_i N_i$$

Adsorption Selectivity Calculations.

The selectivities for the adsorbate mixture composition of interest were calculated from the single-component adsorption isotherms using Ideal Adsorbed Solution Theory (IAST), using a modified version of the program pyIAST.[10] First, the single-component isotherms for the gas sorbates at 298 K were fitted to the dual-site Langmuir-Freundlich (DLF) equation.[11]

$$n(P) = \frac{q_1 (k_1 P)^{n_1}}{1 + (k_1 P)^{n_1}} + \frac{q_2 (k_2 P)^{n_2}}{1 + (k_2 P)^{n_1}}$$

In this equation, q_i is the amount adsorbed per unit mass of material (in mmol g^{-1}), *P* is the total pressure (in bar) of the bulk gas at equilibrium with the adsorbed phase, q_1 and q_2 are the saturation uptakes (in mmol g^{-1}) for sites 1 and 2 respectively, k_1 and k_2 are the affinity coefficients (in bar^{-1}) for sites 1 and 2 respectively and n_1^{-1} and n_2^{-1} represent the deviations from the ideal homogeneous surface (unit-less) for sites 1 and 2 respectively. Final selectivity for adsorbate *i* relative to adsorbate *j* was calculated using the following equation.

$$S_{i/j} = \frac{({}^{x_i}/{x_j})}{({}^{y_i}/{y_j})}$$

Here, x_i and x_j are the mole fractions of components *i* and *j*, respectively, in the adsorbed phase and y_i and y_j are the mole fractions of components *i* and *j*, respectively, in the gas phase. Dual-site Langmuir-Freundlich equation fitting parameters thus obtained for all the adsorbents can be found in Table S3.

Separation factor / Separation selectivity Calculations.

The amount of adsorbed gas *i* (q_i) is calculated from the breakthrough curve as follows:

$$q_i = \frac{V_i T_0 - V_{dead} - \int_0^{t_0} V_e \, \Delta T}{m}$$

Here, V_i is the influent flow rate of gas (cm^3 min^{-1}), V_e is the effluent flow rate of gas (cm^3 min^{-1}), V_{dead} is the dead volume of the system (cm^3), T_0 is the adsorption time (min) and *m* is the mass of the sorbent (g).[12]

The amount of adsorbed gas *i* (q_i) is calculated from the breakthrough curve as follows:

$$q_i = \frac{V_T \Delta T P_i}{m}$$

Here, V_T is the total flow rate of gas (cm^3 min^{-1}), P_i is the partial pressure of gas *i* (bar), ΔT is the time for initial breakthrough of gas *i* to occur (min) and *m* is the mass of the sorbent (g). The separation factor, also known as separation selectivity (α) for the breakthrough experiment *i.e.* breakthrough derived selectivity is determined as follows:

$$\alpha = \frac{q_1 \, y_2}{q_2 \, y_1}$$

y_i is the partial pressure of gas i in the gas mixture. In the case where one gas component has negligible adsorption, the amount of gas adsorbed is treated as ≤ 1 cm^3 for calculations.

For C_2H_2/CO_2 DCB experiments, the C_2H_2 concentration is defined by:

$$Concentration(\mathrm{C_2H_2}) = \frac{signal(\mathrm{C_2H_2})}{signal(\mathrm{C_2H_2}) + signal(\mathrm{CO_2})}$$

CO_2 purity is defined by:

$$Purity(\mathrm{CO_2}) = \frac{signal(\mathrm{CO_2})}{signal(\mathrm{C_2H_2}) + signal(\mathrm{CO_2})}$$

The C_2H_2 uptake calculation in breakthrough experiment is defined by:

$$n(\mathrm{C_2H_2}) = \frac{\int_0^{t_2} (u_i y_{C_2H_2} - u_e(t) y_e(t) A dt}{V_m} = \frac{F \times y_{C_2H_2} \times \int_0^{t_2} (1 - \frac{C(t)}{C_0}) dt}{V_m}$$

$$= \frac{F \times y_{C_2H_2} \times (t_2 - \int_0^{t_2} \frac{C(t)}{C_0} \, dt)}{V_m}$$

Where $n(\mathrm{C_2H_2})$ is the C_2H_2 uptake in mmol g^{-1}, t_2 is the C_2H_2 saturation time, $u_e(t)$ is the transient linear velocity in outlet gas, $y_e(t)$ is the transient C_2H_2 volume fraction in the outlet gas, u_i is the transient linear velocity in inlet gas, F is the inlet gas volume flow rate, $y_{C_2H_2}$ is the volume fraction of C_2H_2 in the mixed gas, $\int_0^{t_2} \frac{C(t)}{C_0} \, dt$ is the integrated area between the C_2H_2 breakthrough curve and the X-axis within the range 0 and t_2, $C(t)$ is the detected C_2H_2 concentration in the outlet gas, C_0 is the detected C_2H_2 concentration in the outlet gas and V_m is molar volume of the gas.

In situ Variable Pressure PXRD.

Crystals of each material were activated in a glass oven at 40 °C under vacuum (pressure: ~1 x 10^{-2} millibar) for approximately 4 h. The activated solid was ground into a fine powder using a pestle and mortar and packed into an environmental gas cell (EGC). The EGC consists of a 0.5 mm glass Lindemann Capillary attached to a steel nut with epoxy, which is then screwed into a valve body. The EGC allows for pressurisation/evacuation of the immediate sample environment while the valve allows for this environment to be isolated and transported to the diffractometer. To determine a diffractogram under vacuum an EGC was attached to a manifold, that in turn was connected to a vacuum pump (pressure: ~7 x 10^{-3} millibar) and left to equilibrate for approximately 4 h. For the variable pressure studies an EGC was attached to a C_2H_2 cylinder *via* a regulator. The system was pressurised and left to equilibrate under static pressure for approximately 4–6 h. After the valve to the EGC was closed, it could be transported to the diffractometer. A PANalytical XPERT-PRO diffractometer was used to record experimental diffractograms. The diffractometer utilises Bragg-Brentano geometry and Cu Kα radiation (λ = 1.5418 Å) as the incident beam. Intensity data were recorded using a capillary spinner to which the EGC was attached. The samples were scanned between 4° and 45° 2θ with a varying scan speed and step size, which was dependent on the nature of the sample.

In situ Infrared (IR) Spectroscopy.

In situ IR measurements were performed on a Nicolet 6700 FTIR spectrometer using a liquid N_2-cooled mercury cadmium telluride (MCT-A) detector. A vacuum cell is placed in the sample compartment of the infrared spectrometer with the sample at the focal point of the beam. The samples (~5 mg) were gently pressed onto KBr pellet and placed into a cell that is connected to a vacuum line for evacuation. The samples of **NbOFFIVE-3-Cu** and **SIFSIX-21-Ni** were activated by evacuation overnight at 60 ºC, respectively, and then cooled back to room temperature for CO_2 and C_2H_2 gas exposure measurement. Note that the IR absorption of the gas phase is prohibitively high at this pressure, making the observation of adsorbed molecules impossible. We pumped out the gas phase and recorded spectra as a function of time in the desorption process. Within ~5 seconds of evacuation, the pressure of gas-phase drops below ~500 mTorr (negligible gas-phase IR absorption).

DFT calculation of vibrational bands of pypz linker.

The DFT calculations and IR vibrational modes presented here were obtained using the Jaguar electronic structure program.[13, 14] Geometry relaxation included perturbation of all rotatable proper and improper torsions, except those in rings and double bonds, to ensure convergence at the minimum energy structure. Subsequent single point vibrational frequencies calculation was carried out to obtain the IR spectrum shown in Figure S62. All structure derivatives were computed using the B3LYP-D3 hybrid functional[15] and 6-31G** basis set.[16] The chemical structure images were drawn with Maestro.[17]

Solid-state (SS) NMR Spectroscopy.

100 mg of the **NbOFFIVE-3-Cu** sample was ground into a fine powder, packed into an L-shaped glass tube, and then connected to a Schlenk line where it was left evacuating at room temperature for 24 h. The samples were then loaded with the guest gases ($^{13}CO_2$: 0.4 eq. per metal; C_2D_2: 0.4 and 0.8 eq. per metal) and sealed off from the Schlenk line. The guest-loaded samples were then left at room temperature for 24 h before the NMR experiments to allow for the equilibration.

All SSNMR experiments were carried out using a Varian Infinity Plus NMR spectrometer, equipped with an Oxford 9.4 T wide-bore magnet and a 5 mm HX static Varian/Chemagnetics probe. Static ^{13}C NMR spectra [$\upsilon_0(^{13}C)$ = 100.5 MHz] were referenced to TMS using the high-frequency signal of ethanol at 58.05 ppm as a secondary reference.[18] Experiments were performed using the DEPTH-echo pulse sequence to remove the background from the probe,[19] with a 90° pulse width of 3.2 µs and a 180° pulse width of 6.4 µs. The spectral width was 300 kHz and the optimized recycle delay was 3 s. The number of scans required for static VT ^{13}C ranges from 700 to 1000 scans. Static ^{2}H NMR spectra [$\upsilon_0(^{13}C)$ = 61.3 MHz] were referenced using the signal of $D_2O(l)$ at 4.80 ppm as a secondary reference.[18] A quadrupolar echo pulse sequence of the form ($\pi/2-\tau1-\pi/2-\tau2$) was used with a 90° pulse width of 4.0 µs, a τ_1 of 30.0 µs and a τ_2 of 30.0 µs. The spectral width was 500 kHz and the optimized ^{2}H recycle delay was 0.5 s. The number of scans required for static ^{2}H VT SSNMR experiments ranges between 3000 and 3200 scans. The WSolids software package[20] was used to simulate all static SSNMR spectra in order to extract the NMR parameters of gas molecules from observed spectra. The EXPRESS software[21] was used to simulate the effects of guest motion.

Synthesis of compounds.

3,5-dimethyl-1*H*-pyrazol-4-yl)pyridine (pypz) synthesis.

3,5-dimethyl-1*H*-pyrazol-4-yl)pyridine was synthesized following reported procedure.[22]

Preparation of SIFSIX-21-Ni single crystals. Single crystals of the compound **SIFSIX-21-Ni** were obtained by solvothermal reaction as following: a suspension of **pypz** (0.1 mmol, 17 mg) and $NiSiF_6.6H_2O$ (0.05 mmol, 15 mg) in MeOH (3 mL) were reacted at 85 °C in a small 10.5 mL glass vial for overnight, keeping in a fixed-temperature oven. The crystals were collected in *ca.* 75 % yield by filtration and washed with MeOH three times.

Preparation of TIFSIX-4-Ni single crystals. MeOH (2 mL) was carefully layered over a solution of $NiTiF_6.6H_2O$ (0.05 mmol, 16 mg) 2 mL of MeOH to which **pypz** (0.1 mmol, 17 mg) in 2 mL of MeOH was layered. Light pink single crystals were obtained after several days with *ca.* 60 % yield. The crystals were harvested by filtration and washed with MeOH three times.

Preparation of SIFSIX-21-Cu single crystals.

Single crystals of the compound **SIFSIX-21-Cu.** An ethylene glycol solution (2 ml) of $Cu(NO_3)_2$ (8.4 mg, 0.035 mmol) and $(NH_4)_2SiF_6$ (6.2 mg, 0.035 mmol) was prepared and carefully transferred to a test tube of 10 cm length and 1 cm diameter. A buffer solution of ethylene-glycol:methanol (1:1/v:v) was prepared and 6 ml of this was carefully layered above the first solution, creating a defined layer between the two. A methanol solution (2 ml) of ligand **pypz** (12 mg, 0.07 mmol) was layered on top of the buffer solution creating a third layer. The test-tube was sealed and left to stand. After two weeks, small blue/violet coloured crystals formed on the inside of the test-tube.

Preparation of TIFSIX-4-Cu single crystals.

Single crystals of the compound **TIFSIX-4-Cu.** Crystals were made following the same method as that used for **TIFSIX-4-Cu**, however $(NH_4)_2TiF_6$ (6.7 mg, 0.035 mmol) was used in place of $(NH_4)_2SiF_6$.

Preparation of NbOFFIVE-3-Ni crystalline powder. Crystalline powder of **NbOFFIVE-3-Ni** can be prepared by solvothermal reaction as following: a suspension of **pypz** (1 mmol, 170 mg) and $NiNbOF_5.6H_2O$ (0.5 mmol, 185 mg) in MeOH (15 mL) were reacted at 85 °C in a 100 ml Schott Duran® bottle for overnight, keeping in a fixed-temperature oven. The powder was collected in *ca.* 70% yield by filtration and washed with MeOH three times.

Preparation of NbOFFIVE-3-Cu crystalline powder. Crystalline powder of **NbOFFIVE-3-Cu** can be prepared from the similar procedure of **NbOFFIVE-3-Ni**, using $CuNbOF_5.6H_2O$ (0.5 mmol, 187 mg) instead of $NiNbOF_5.6H_2O$.

Preparation of SIFSIX-21-Cu crystalline powder. Crystalline powder of **SIFSIX-21-Cu** can be prepared from the similar procedure of **NbOFFIVE-3-Ni**, using $CuSiF_6.6H_2O$ (0.5 mmol, 157 mg) instead of $NiNbOF_5.6H_2O$.

Preparation of TIFSIX-4-Cu crystalline powder. Crystalline powder of **TIFSIX-4-Cu** can be prepared from the similar procedure of **NbOFFIVE-3-Ni**, using $CuTiF_6.6H_2O$ (0.5 mmol, 167 mg) instead of $NiNbOF_5.6H_2O$.

Preparation of TIFSIX-4-Ni crystalline powder. Crystalline powder of **TIFSIX-4-Ni** can be prepared from the similar procedure of **NbOFFIVE-3-Ni**, using $NiTiF_6.6H_2O$ (0.5 mmol, 164 mg) instead of $NiNbOF_5.6H_2O$.

Scale up for SIFSIX-21-Ni. SIFSIX-21-Ni can be scaled up from the similar procedure of **NbOFFIVE-3-Ni**, using $NiSiF_6.6H_2O$ (0.5 mmol, 154 mg) instead of $NiNbOF_5.6H_2O$.

Modelling Studies.

The binding sites for C_2H_2 and CO_2 in **SIFSIX-21-Ni** were determined through classical molecular simulations. All parametrizations and simulations were performed on the single X-ray crystallographic structure published herein for the material.

All atoms of **SIFSIX-21-Ni** were treated with Lennard-Jones (LJ) parameters (ε and σ), point partial charges and point polarizabilities in order to model repulsion/dispersion, stationary electrostatic and many-body polarization interactions, respectively. The LJ parameters for all C and H atoms were taken from the Optimized Potentials For Liquid Simulations – All Atom (OPLS-AA) force field,[23] while those for the N, F, Si and Ni atoms were taken from the Universal Force Field (UFF).[24] The partial charges for the chemically distinct atoms in **SIFSIX-21-Ni** were determined through the Restrained Electrostatic Potential (RESP) method[25] using the CP2K program.[26] The exponential damping-type polarizability values for all C, H, N and F atoms were taken from a carefully parametrized set provided by the work of van Duijnen and Swart.[27] The polarizability parameter for Si^{4+} and Ni^{2+} was calculated in previous work[28, 29] and used herein. After the hydrogen nuclei were optimized, a Restrained Electrostatic Surface Potential (RESP) charge fit was performed to obtain partial charges on each atom for use in empirical simulation. Universal force Field (UFF)[24] radii were used during the sphere sampling protocol.

Simulated annealing (SA) calculations[30] were performed for a single molecule of both adsorbates through a canonical Monte Carlo (*NVT*) process in a 2 × 2 × 2 supercell of **SIFSIX-21-Ni**. This was done in order to identify the most favorable binding site for both adsorbates in the material. All HUM atoms were kept fixed at their crystallographic positions throughout the simulations. A spherical cut-off distance of 14.6342 Å, representing half the shortest supercell dimension length, was used for the simulations. C_2H_2 and CO_2 were modeled using polarizable potentials of the respective adsorbates that were developed previously.[31, 32] The total potential energy of the HUM–adsorbate system was calculated through the sum of the repulsion/dispersion, stationary electrostatic and many-body polarization energies. These were calculated using the LJ potential,[33] the Ewald summation technique,[34, 35] and a Thole-Applequist type model,[36-39] respectively. SA calculations for both adsorbates utilized an initial temperature of 500 K and this temperature was scaled by a factor of 0.99999 after every 1.0×10^3 Monte Carlo steps. The simulations continued until the temperature of the system dropped below 10 K.

Next, canonical Monte Carlo (CMC) simulations were performed for a single molecule of C_2H_2 and CO_2, individually, positioned at their global minimum in **SIFSIX-21-Ni**. This was done in order to evaluate the averaged classical potential energy for both adsorbates about their energy minimum position in the material. As with the SA calculations, the simulations were carried out within the rigid 2 × 2 × 2 supercell of the HUM using the same force fields. The CMC simulations were performed at a temperature of 298 K and a pressure of 0.10 atm. These simulations ran for a total of 1.0×10^6 Monte Carlo steps to ensure reasonable ensemble averages for the total potential energy of the system. The averaged classical potential energies for C_2H_2 and CO_2 localized about their energy minimum position in **SIFSIX-21-Ni** are presented in Table S4. All SA calculations and CMC simulations were carried out using the Massively Parallel Monte Carlo (MPMC) code.[40, 41]

Modelling details of C_2H_2 and CO_2 sites which corresponds to the Figure S53.

To study the C_2H_2 and CO_2 binding sites in **SIFSIX-21-Ni** systematically, periodic DFT calculations are performed with the Vienna Ab Initio Simulation Package (VASP 5.4.4).[42, 43] To describe the interactions between the HUM and adsorbates accurately, we opted for the BEEF-vdW functional.[44] This functional is parametrized with training data based on the CCSD(T) method, it is therefore also an excellent choice to account for van der Waals interactions as well as hydrogen bonds especially valuable for the comparison of CO_2 and C_2H_2 adsorption enthalpies. The one-electron Kohn-Sham orbitals were expanded in a plane wave basis set with a kinetic energy cut-off of 550 eV for all calculations. PAW potentials are employed to describe the interaction between the valence electrons and the core.[45] The HUM is first structurally cell-optimized (Γ-point) until the largest force is smaller than 0.02 eV/Å. Afterwards, the atomic positions of the HUM-lattice are fixed and the adsorbates are optimized until the largest force is smaller than 0.01 eV/Å. Furthermore, a Gaussian smearing of 0.05 eV is applied to improve convergence,[42] while the convergence criterion for the electric self-consistent field (SCF) problem is set to 10^{-5} eV for all optimizations. For the energy calculations on the converged structures, the reciprocal space integration over the Brillouin zone is approximated with finite sampling using

Monkhorst-Pack grids [46, 47] using a 3x3x3 k-point grid. For the optimized binding site of C_2H_2 (Figure S53a), there were no imaginary modes observed, while for the optimized binding sites of CO_2, there are 1 or 2 imaginary modes for the geometries given in Figures S53b and S53c, respectively. For the calculation of the enthalpies, these imaginary modes are replaced by an arbitrary mode of 100 cm^{-1}. To verify the local minima, a relevant partial Hessian vibrational analysis (PHVA) is employed, keeping all atoms from the framework fixed except the adsorbate. The PHVA is used also to obtain zero-point corrections and enthalpy contributions.[48, 49] The numerical partial Hessian is calculated by displacements in x, y and z-directions of ±0.004 Å and the vibrational modes are extracted using the normal mode analysis as implemented in the post-processing toolkit TAMKIN.[50]

Powder X-ray Diffraction.

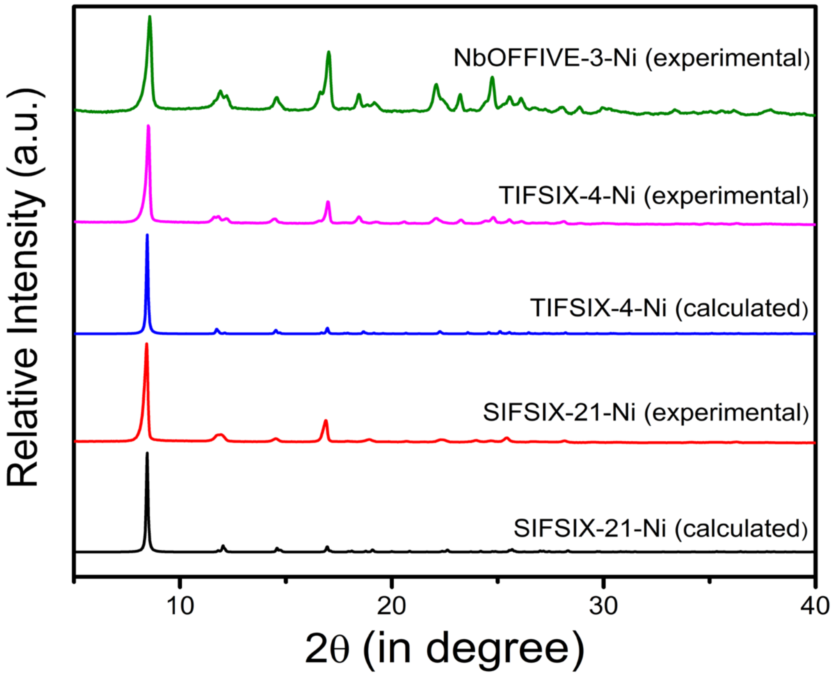

Figure S1. PXRD profiles of **SIFSIX-21-Ni, TIFSIX-4-Ni and NbOFFIVE-3-Ni**, validating phase purity.

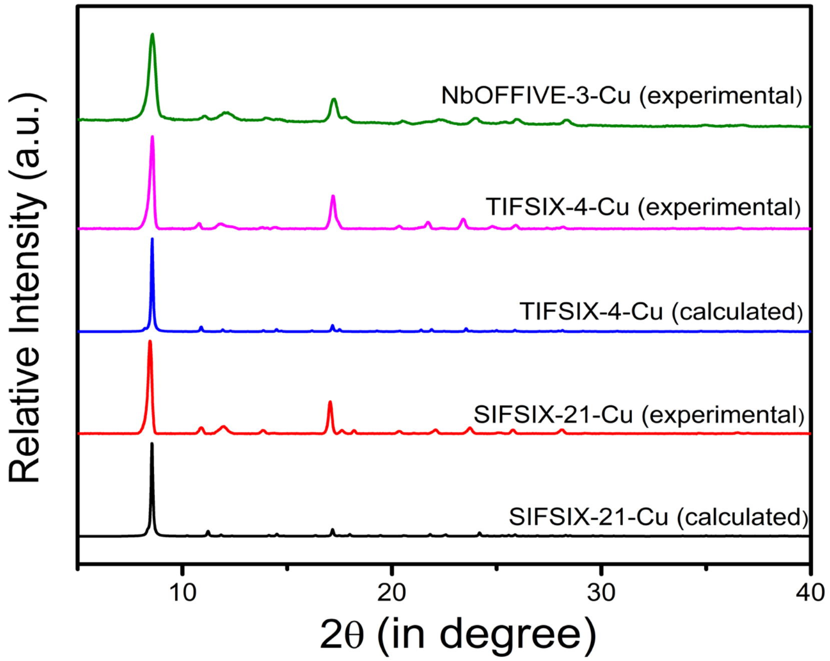

Figure S2. PXRD profiles of **SIFSIX-21-Cu, TIFSIX-4-Cu and NbOFFIVE-3-Cu**, validating phase purity.

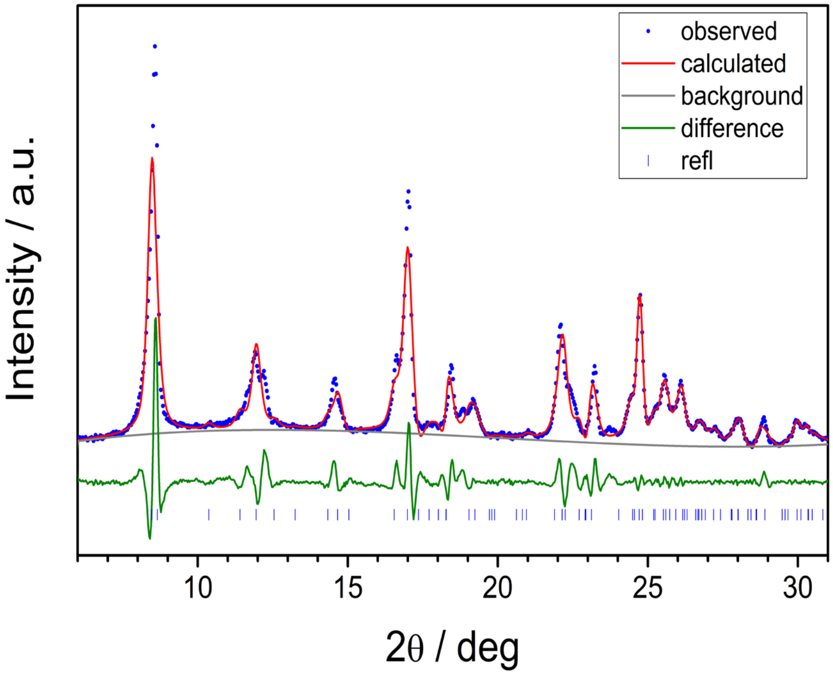

Figure S3. Pawley profile fit of the PXRD patterns of **NbOFFIVE-3-Ni**. Space group = *Pnna*, a = 14.804(8) Å, b = 15.50(15) Å, c = 14.10(12) Å, $\alpha = 90°$, $\beta = 90°$, $\gamma = 90°$, V = 3236(3) Å^3, Rwp = 16.9 %.

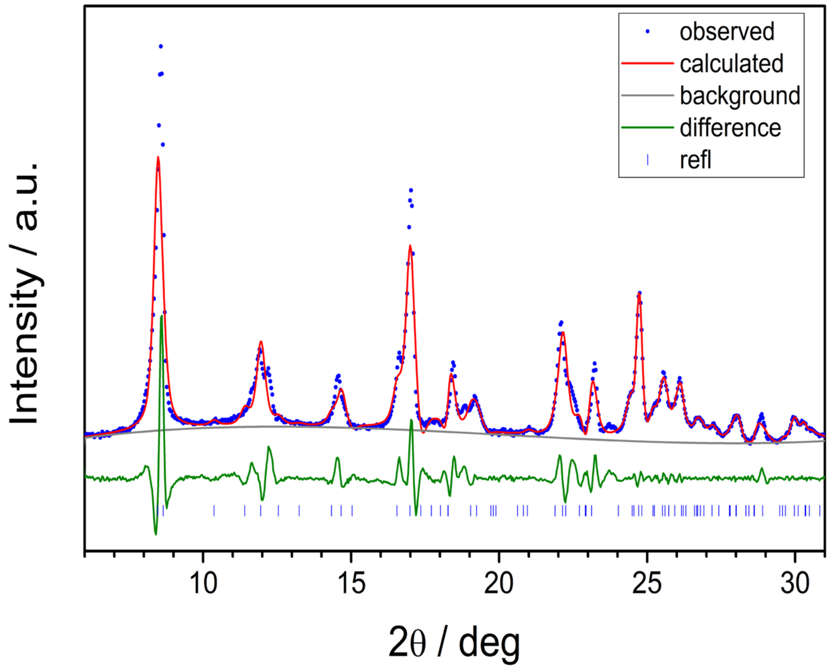

Figure S4. Pawley profile fit of the PXRD patterns of **NbOFFIVE-3-Cu**. Space group = *Pnna*, a = 14.894(3) Å, b = 15.705(3) Å, c = 14.272(3) Å, $\alpha = 90°$, $\beta = 90°$, $\gamma = 90°$, V = 3338(17) Å^3, Rwp = 9.18 %.

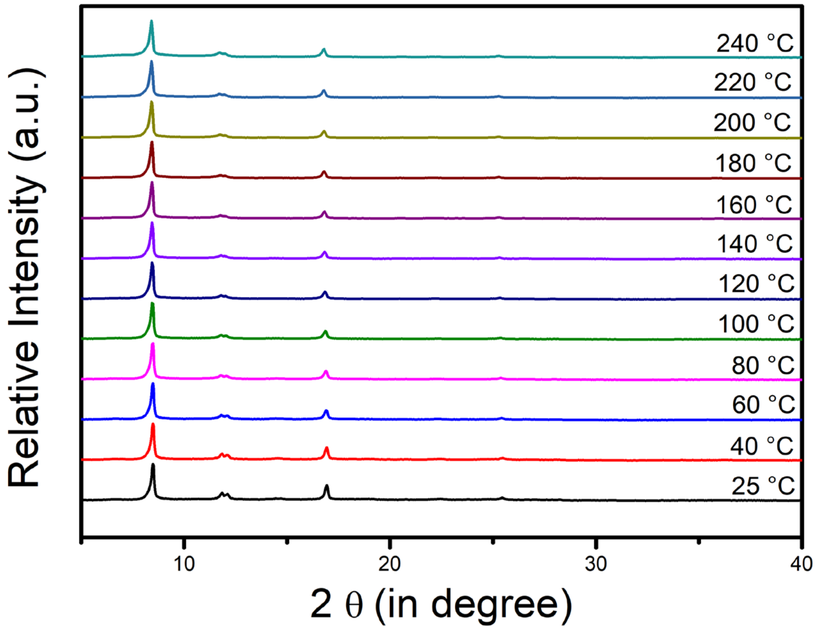

Figure S5. Variable temperature (VT) PXRD profiles of **SIFSIX-21-Ni**.

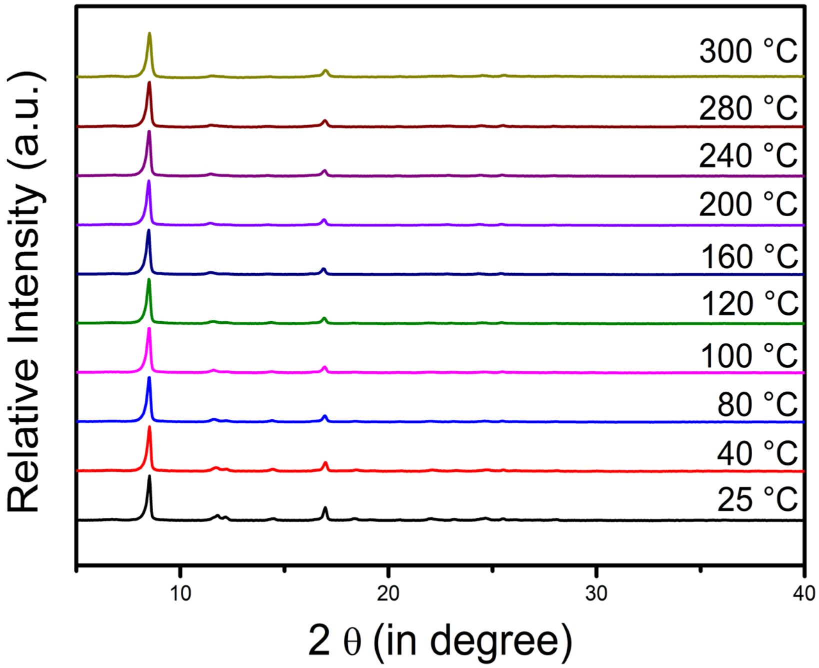

Figure S6. VT-PXRD profiles of **TIFSIX-4-Ni**.

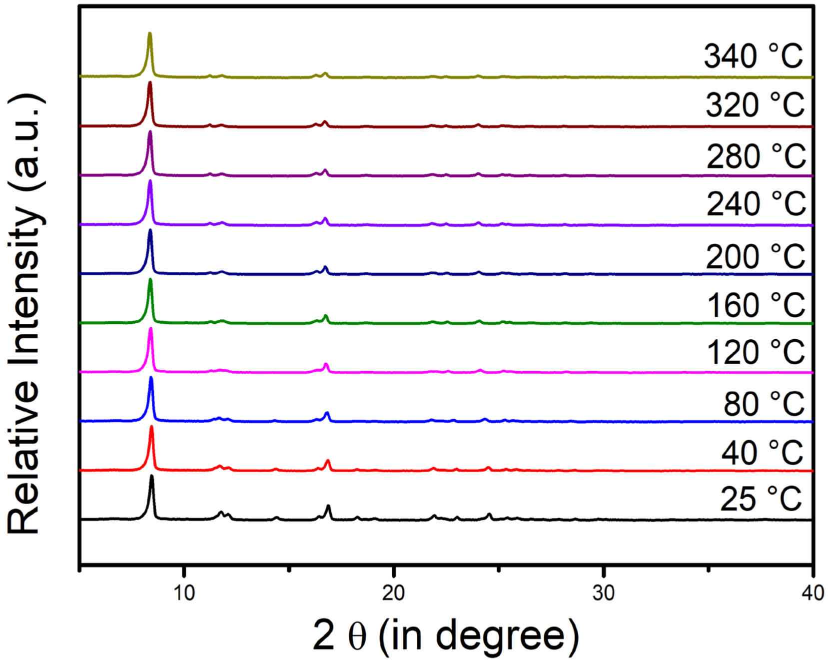

Figure S7. VT-PXRD profiles of **NbOFFIVE-3-Ni**.

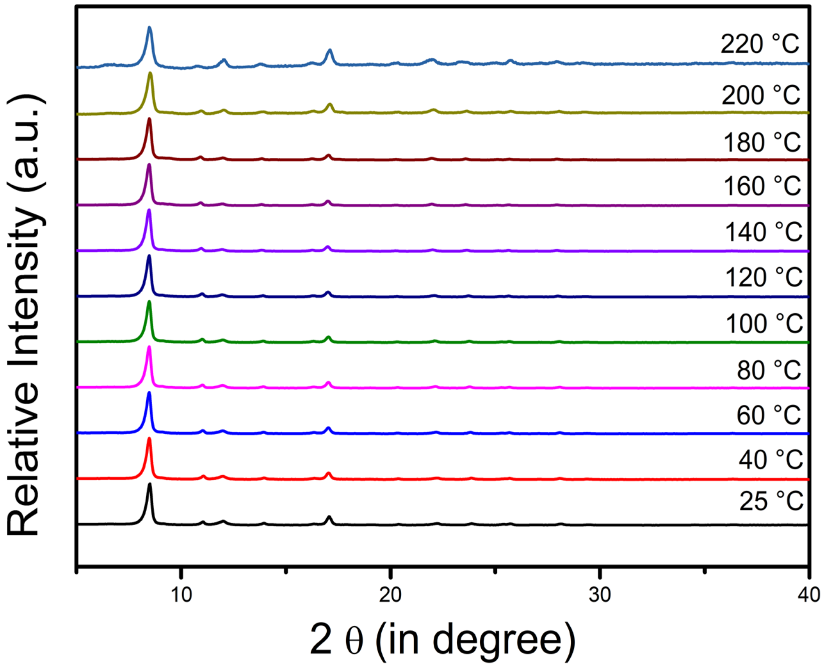

Figure S8. VT-PXRD profiles of **SIFSIX-21-Cu**.

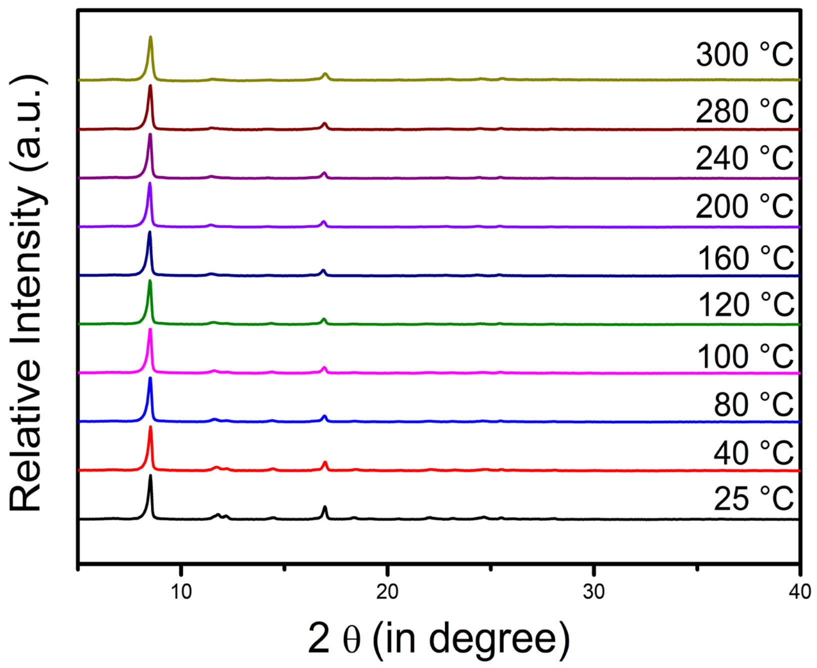

Figure S9. VT-PXRD profiles of **TIFSIX-4-Cu**.

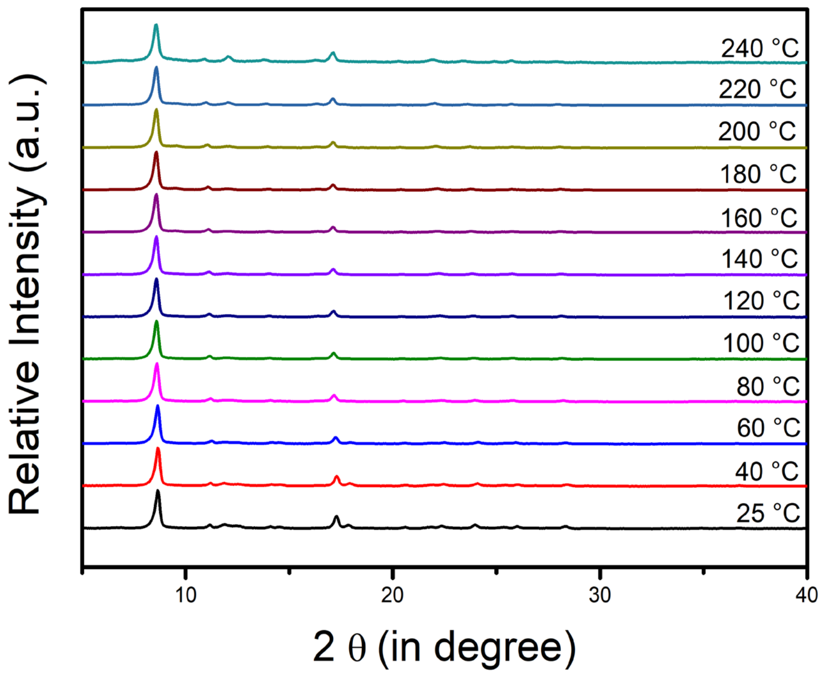

Figure S10. VT-PXRD profiles of **NbOFFIVE-3-Cu**.

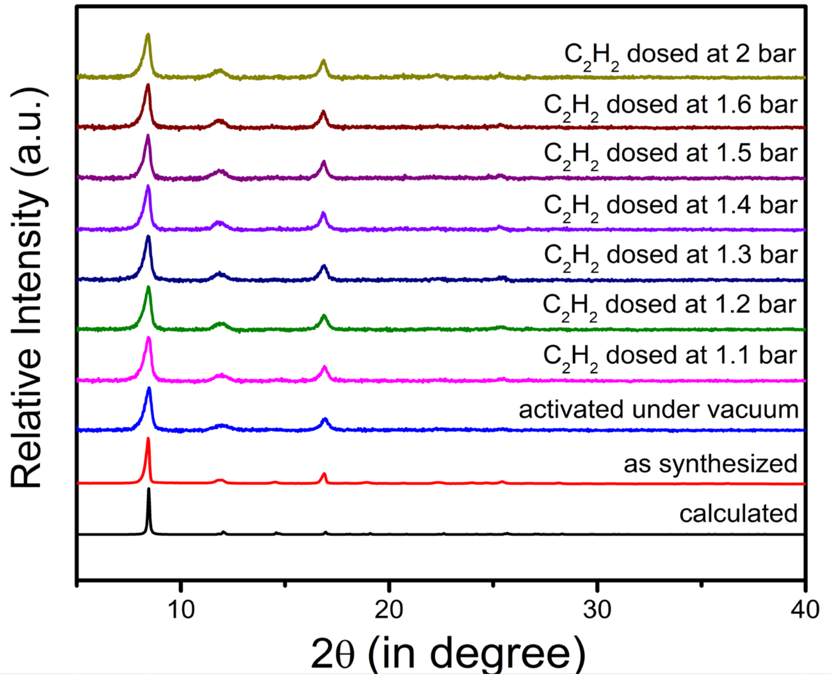

Figure S11. *In situ* PXRD profiles of **SIFSIX-21-Ni** on C_2H_2 dosing.

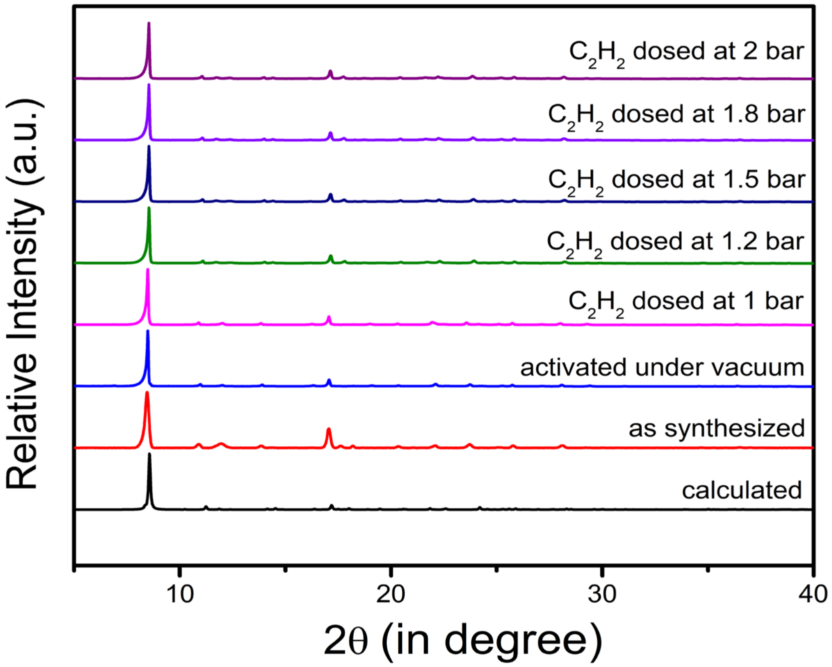

Figure S12. *In situ* PXRD profiles of **SIFSIX-21-Cu** on C_2H_2 dosing.

Thermogravimetric Analysis (TGA).

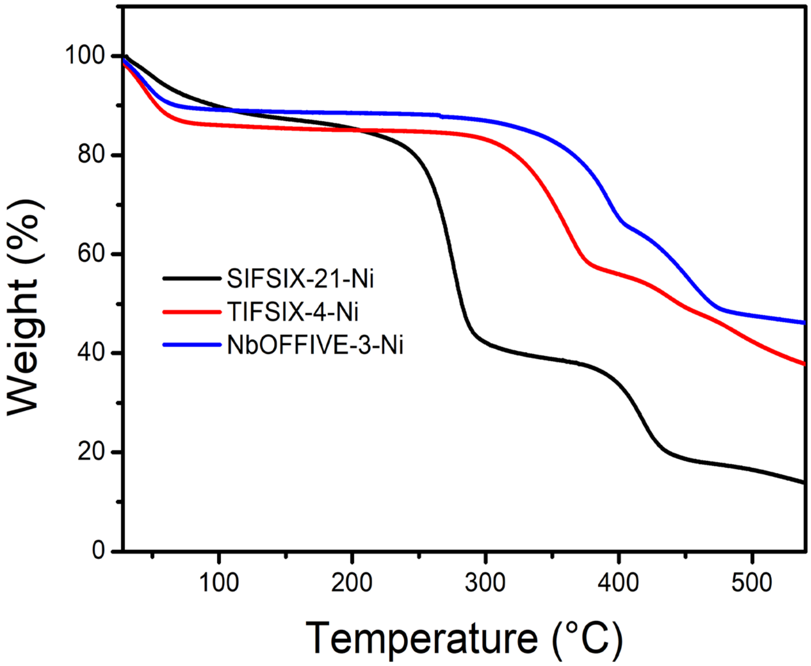

Figure S13. Thermogravimetric analysis profiles of the as-synthesised **SIFSIX-21-Ni, TIFSIX-4-Ni** and **NbOFFIVE-3-Ni**.

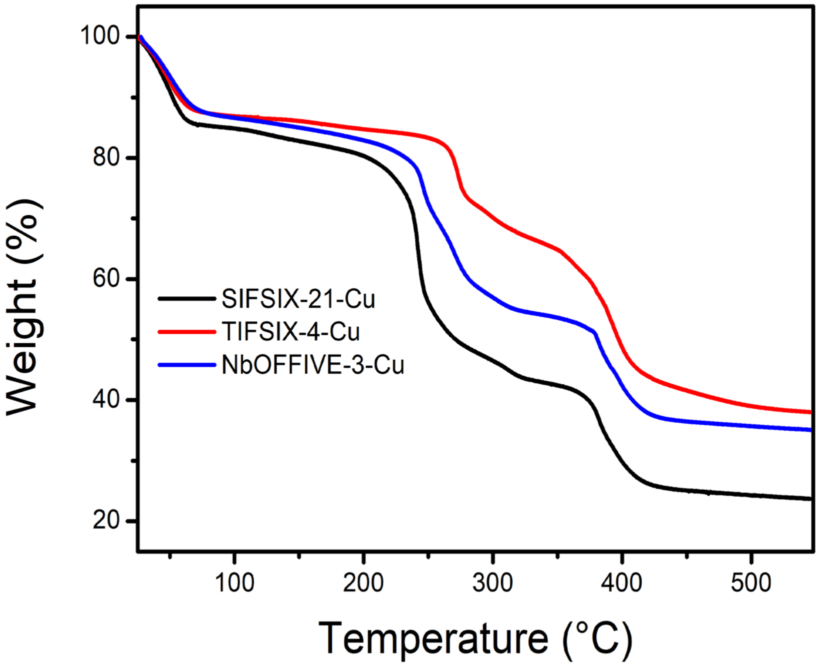

Figure S14. Thermogravimetric analysis profiles of the as-synthesised **SIFSIX-21-Cu, TIFSIX-4-Cu** and **NbOFFIVE-3-Cu**.

Gas Sorption Isotherms.

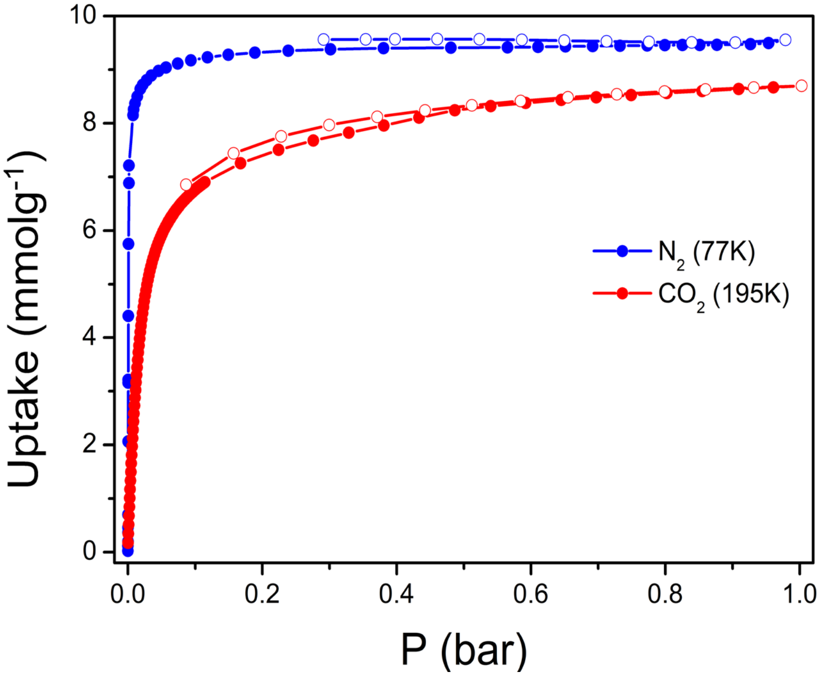

Figure S15. Low temperature CO_2 and N_2 sorption isotherms for **SIFSIX-21-Ni** (filled shape: adsorption; hollow shape: desorption) with BET surface areas 871 m^{2}g^{-1} and 776 m^{2}g^{-1} determined from N_2 and CO_2 isotherms respectively.

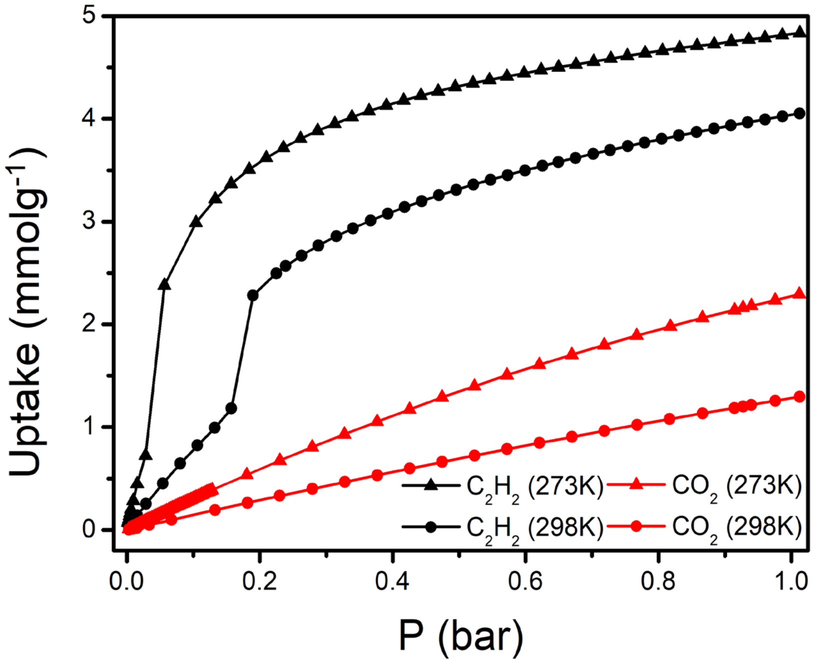

Figure S16. C_2H_2 and CO_2 adsorption isotherms for **SIFSIX-21-Ni**.

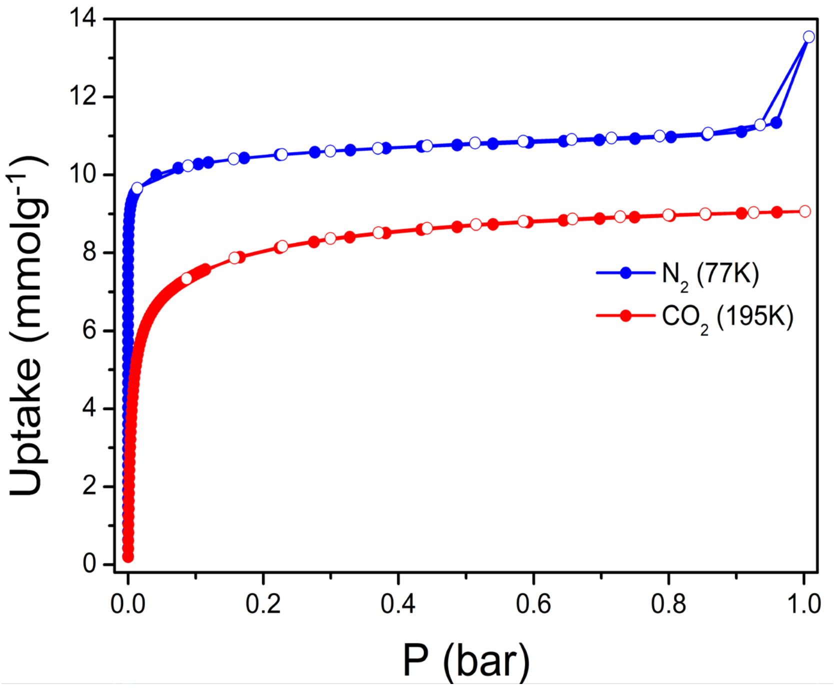

Figure S17. Low temperature CO_2 and N_2 sorption isotherms for **TIFSIX-4-Ni** (filled shape: adsorption; hollow shape: desorption) with BET surface areas 931 m^{2}g^{-1} and 700 m^{2}g^{-1} determined from N_2 and CO_2 isotherms respectively. Last adsorption data point is an outcome of condensation in inter-particle voids (similar to other physisorbents, such as **ZIF-8**, microporous silica material, and carbon nitride).[51-54]

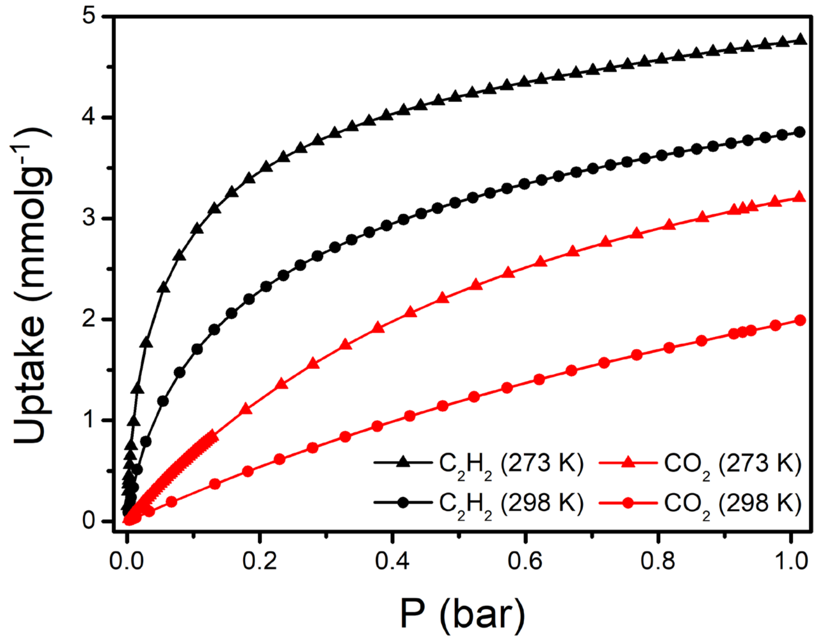

Figure S18. C_2H_2 and CO_2 adsorption isotherms for **TIFSIX-4-Ni**.

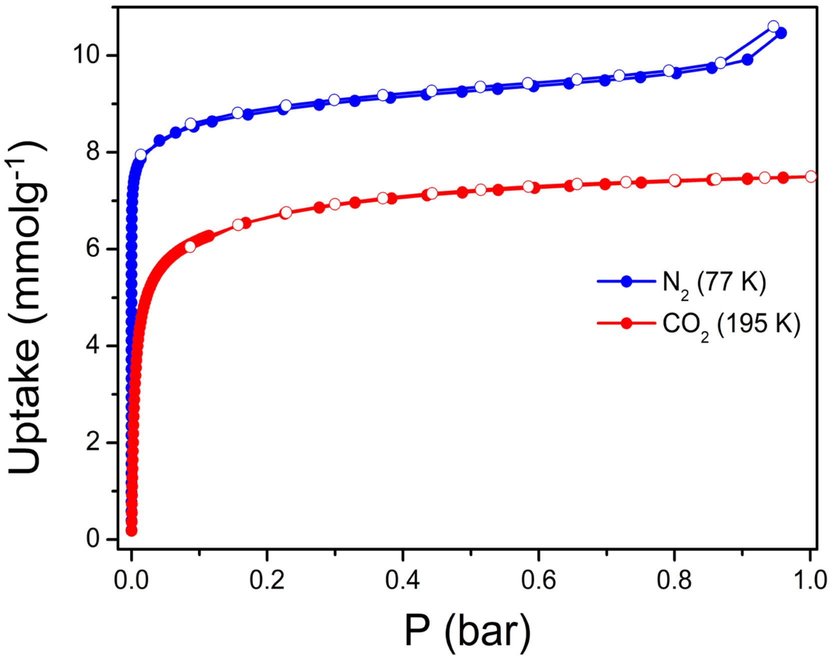

Figure S19. Low temperature CO_2 and N_2 sorption isotherms for **NbOFFIVE-3-Ni** (filled shape: adsorption; hollow shape: desorption) with BET surface areas 761 m^{2}g^{-1} and 599 m^{2}g^{-1} determined from N_2 and CO_2 isotherms respectively. Last adsorption data point is an outcome of condensation in inter-particle voids (similar to other physisorbents, such as ZIF-8, microporous silica material, and carbon nitride).[51-54]

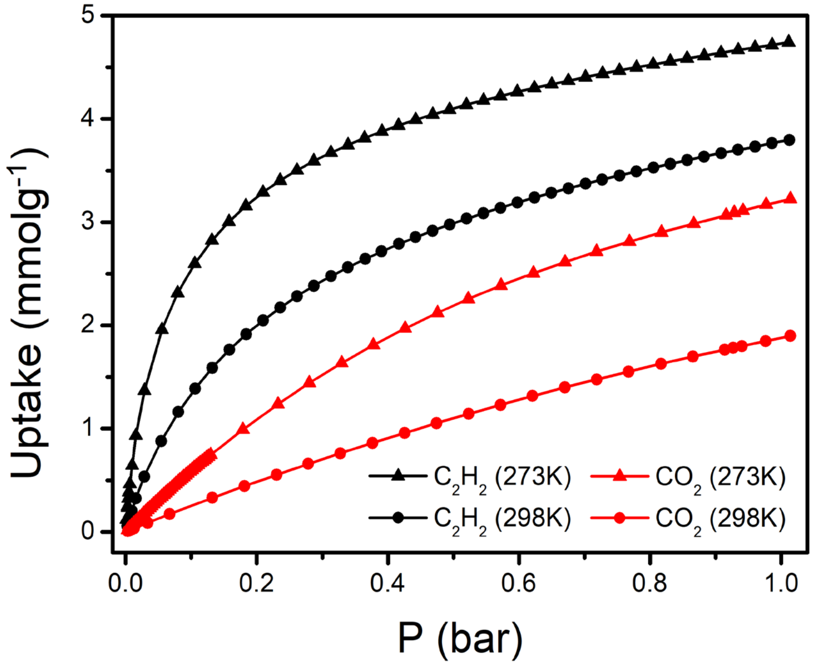

Figure S20. C_2H_2 and CO_2 adsorption isotherms for **NbOFFIVE-3-Ni**.

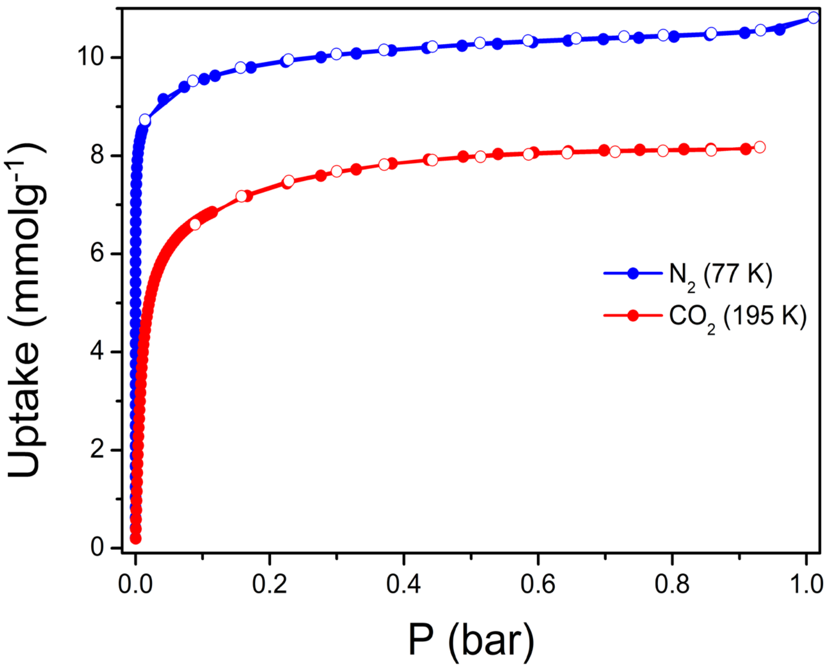

Figure S21. Low temperature CO_2 and N_2 sorption isotherms for **SIFSIX-21-Cu** (filled shape: adsorption; hollow shape: desorption) with BET surface areas 839 m^{2}g^{-1} and 695 m^{2}g^{-1} determined from N_2 and CO_2 isotherms respectively.

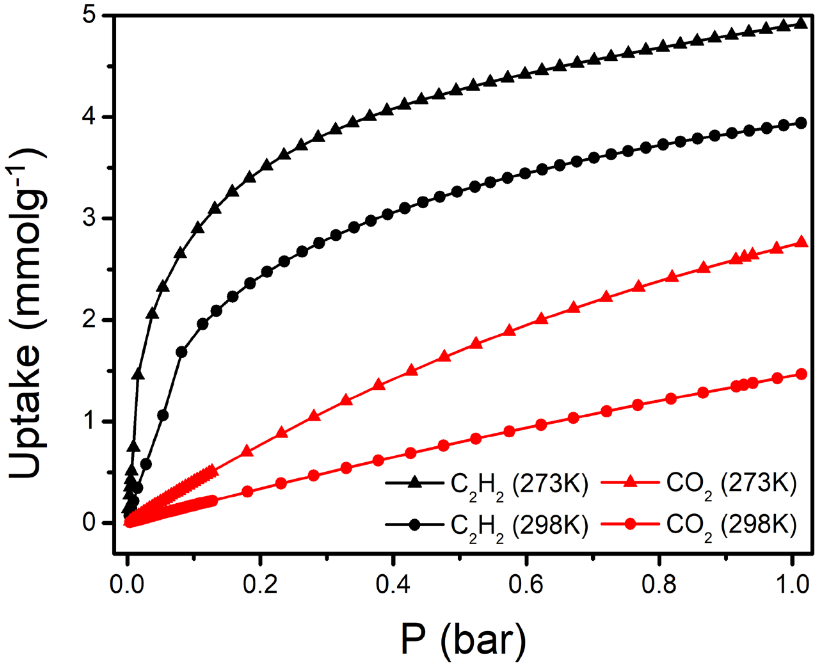

Figure S22. C_2H_2 and CO_2 adsorption isotherms for **SIFSIX-21-Cu**.

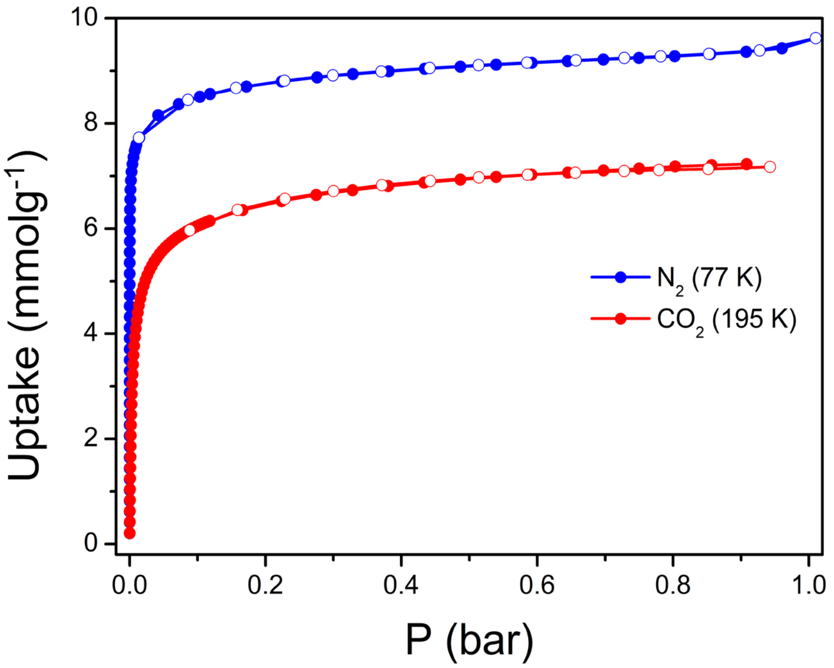

Figure S23. Low temperature CO_2 and N_2 sorption isotherms for **TIFSIX-4-Cu** (filled shape: adsorption; hollow shape: desorption) with BET surface areas 747 m^{2}g^{-1} and 568 m^{2}g^{-1} determined from N_2 and CO_2 isotherms respectively.

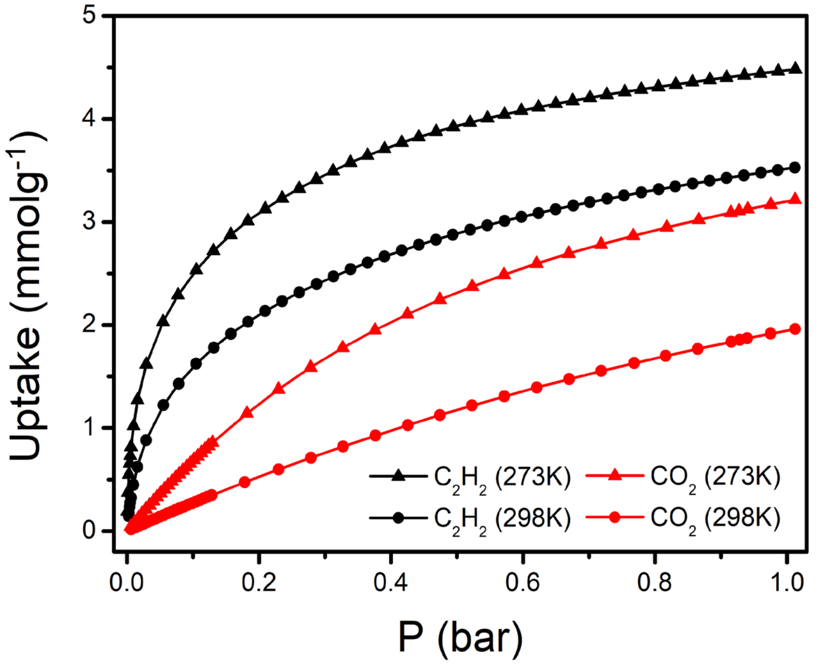

Figure S24. C_2H_2 and CO_2 adsorption isotherms for **TIFSIX-4-Cu**.

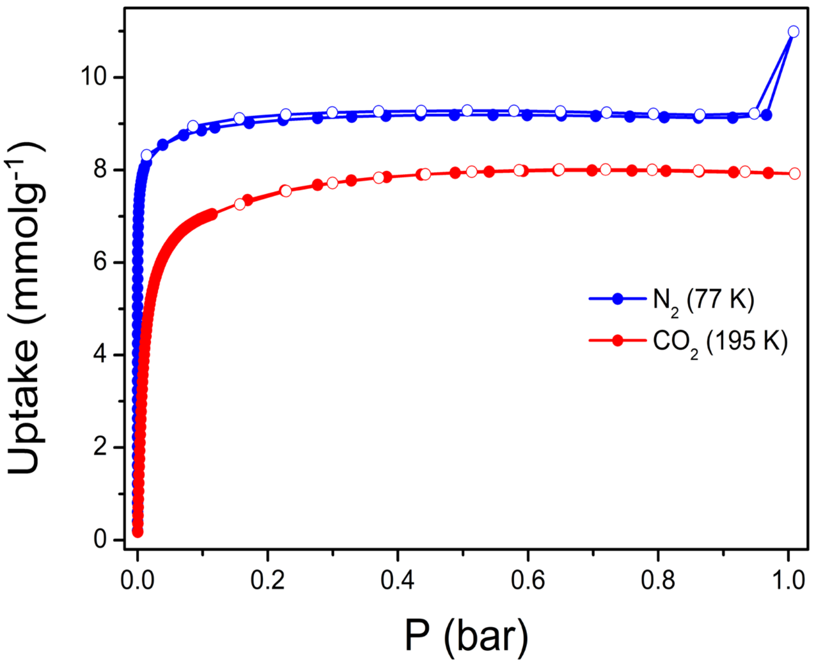

Figure S25. Low temperature CO_2 and N_2 sorption isotherms for **NbOFFIVE-3-Cu** (filled shape: adsorption; hollow shape: desorption) with BET surface areas 805 m^2g^{-1} and 722 m^2g^{-1} determined from N_2 and CO_2 isotherms respectively Last adsorption data point is an outcome of condensation in inter-particle voids (similar to other physisorbents, such as ZIF-8, microporous silica material, and carbon nitride).[51-54]

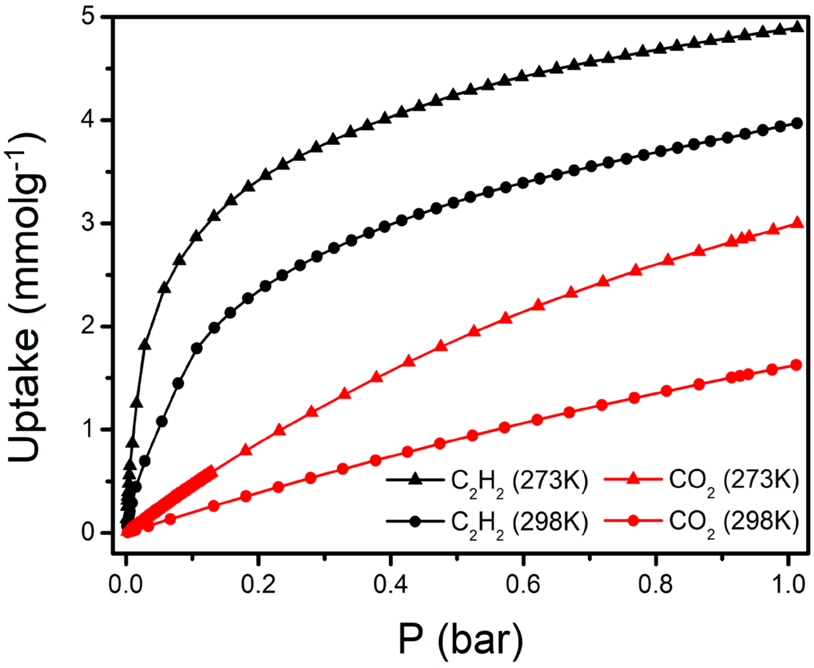

Figure S26. C_2H_2 and CO_2 adsorption isotherms for **NbOFFIVE-3-Cu**.

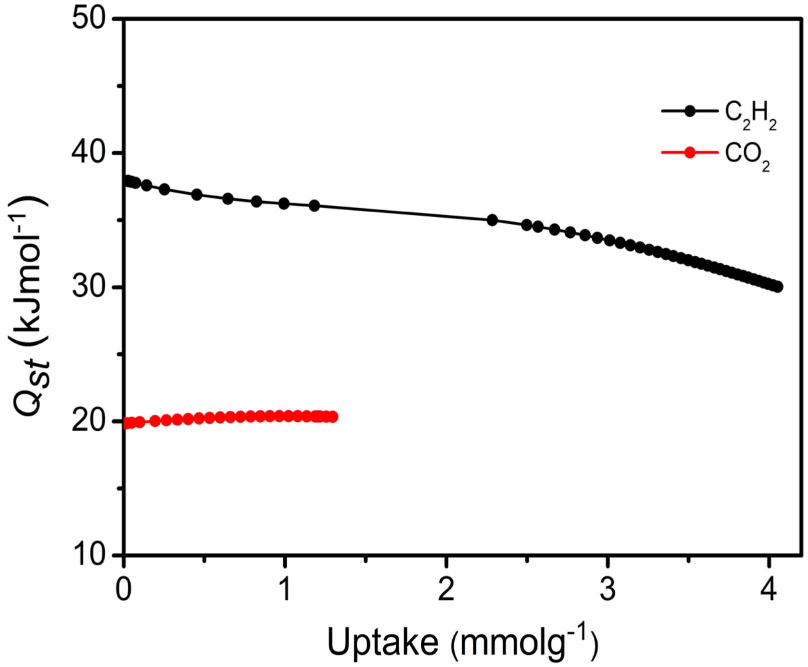

Figure S27. Isosteric enthalpies of adsorption for C_2H_2 and CO_2 for **SIFSIX-21-Ni**.

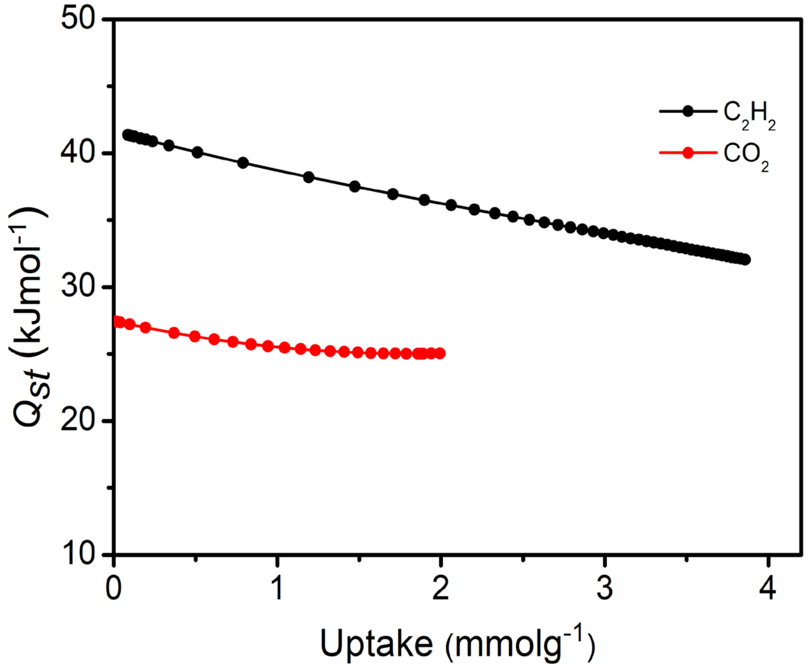

Figure S28. Isosteric enthalpies of adsorption for C_2H_2 and CO_2 for **TIFSIX-4-Ni**.

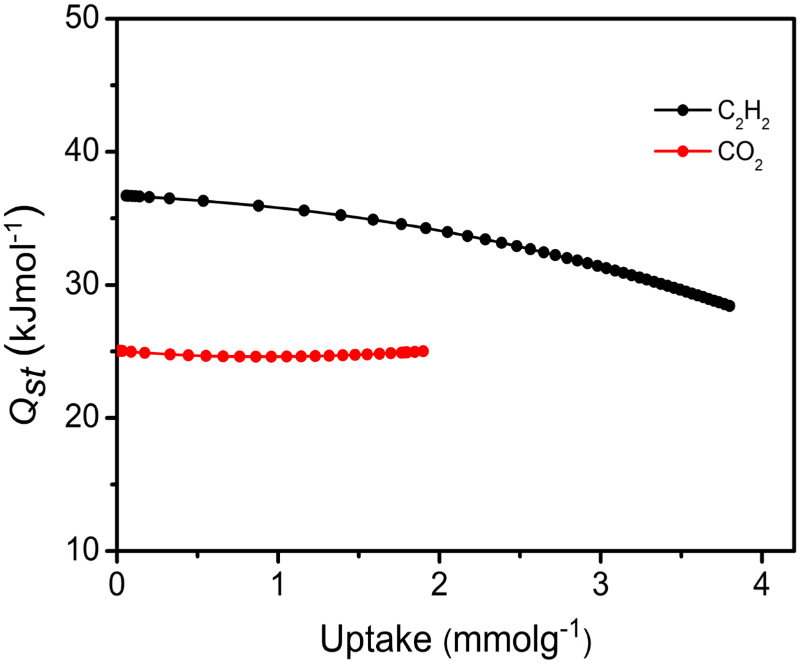

Figure S29. Isosteric enthalpies of adsorption for C_2H_2 and CO_2 for **NbOFFIVE-3-Ni**.

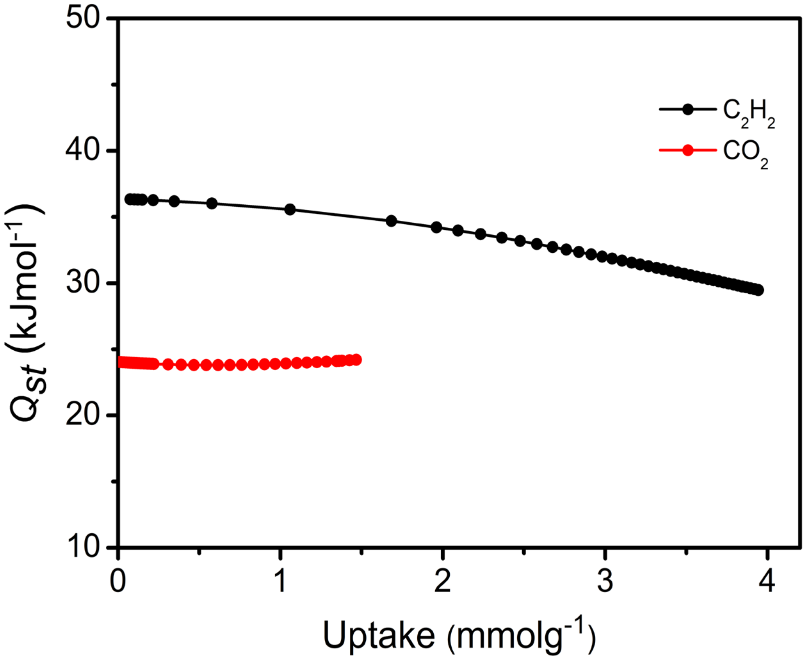

Figure S30. Isosteric enthalpies of adsorption for C_2H_2 and CO_2 for **SIFSIX-21-Cu**.

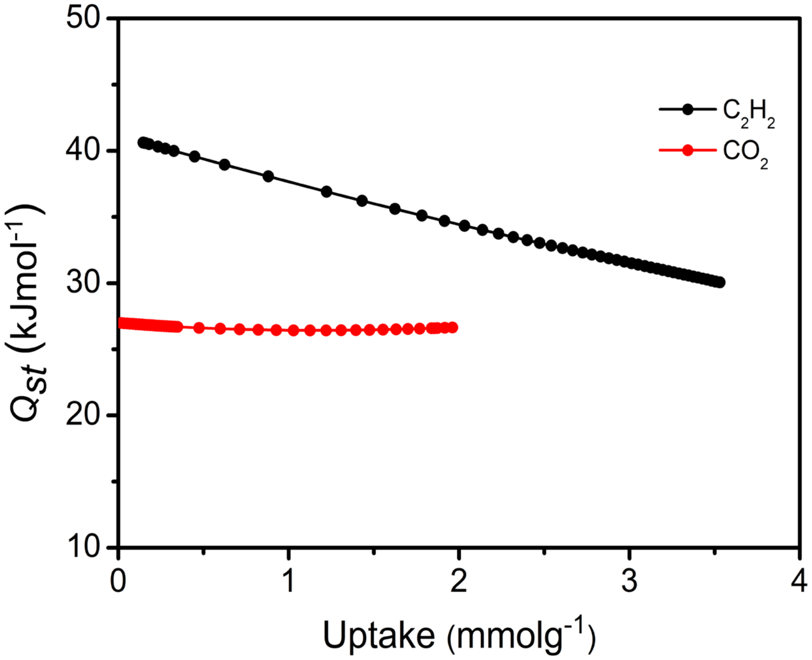

Figure S31. Isosteric enthalpies of adsorption for C_2H_2 and CO_2 for **TIFSIX-4-Cu**.

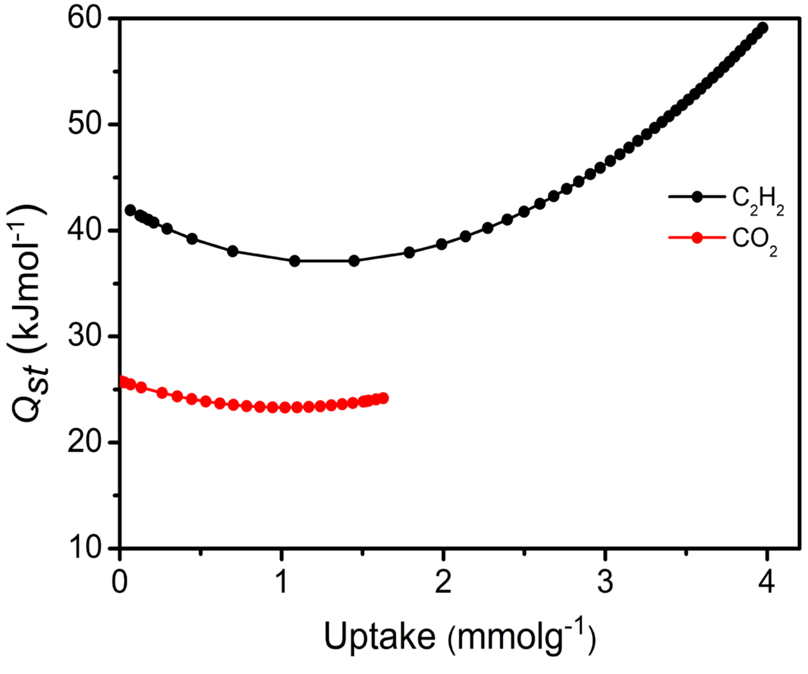

Figure S32. Isosteric enthalpies of adsorption for C_2H_2 and CO_2 for **NbOFFIVE-3-Cu**.

Q_{st} Calculation - Virial Fitting

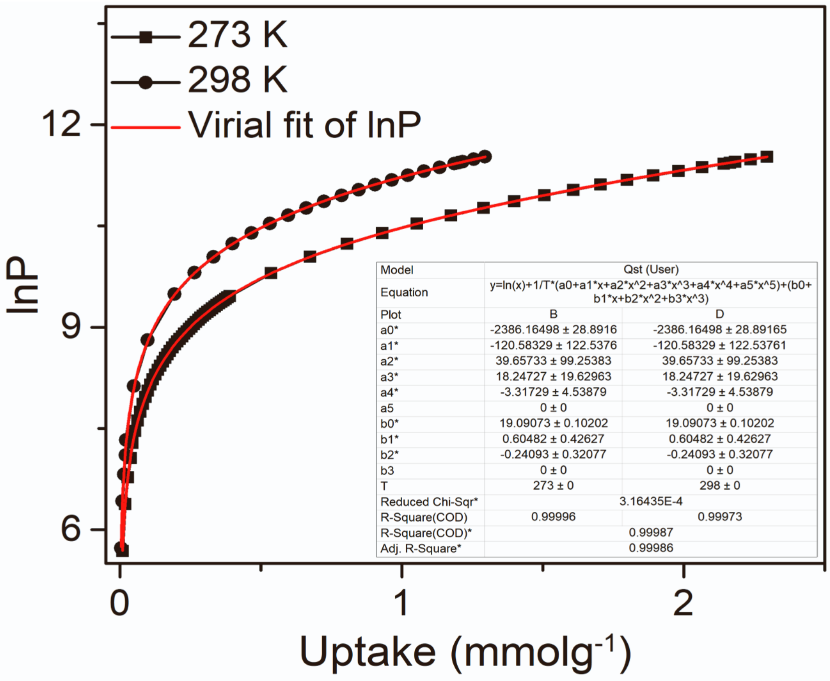

Model	Qst (User)	
Equation	y=ln(x)+1/T*(a0+a1*x+a2*x^2+a3*x^3+a4*x^4+a5*x^5)+(b0+ b1*x+b2*x^2+b3*x^3)	
Plot	B	D
a0*	-2386.16498 ± 28.8916	-2386.16498 ± 28.89165
a1*	-120.58329 ± 122.5376	-120.58329 ± 122.53761
a2*	39.65733 ± 99.25383	39.65733 ± 99.25383
a3*	18.24727 ± 19.62963	18.24727 ± 19.62963
a4*	-3.31729 ± 4.53879	-3.31729 ± 4.53879
a5	0 ± 0	0 ± 0
b0*	19.09073 ± 0.10202	19.09073 ± 0.10202
b1*	0.60482 ± 0.42627	0.60482 ± 0.42627
b2*	-0.24093 ± 0.32077	-0.24093 ± 0.32077
b3	0 ± 0	0 ± 0
T	273 ± 0	298 ± 0
Reduced Chi-Sqr*	3.16435E-4	
R-Square(COD)	0.99996	0.99973
R-Square(COD)*	0.99987	
Adj. R-Square*	0.99986	

Figure S33. Fitting of the CO_2 isotherm data for **SIFSIX-21-Ni** to the virial equation.

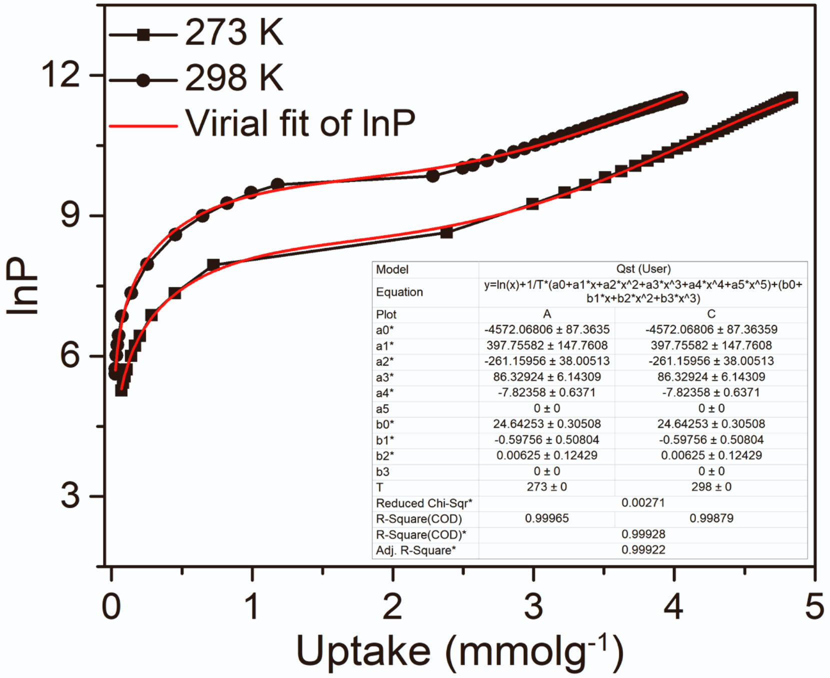

Model	Qst (User)	
Equation	y=ln(x)+1/T*(a0+a1*x+a2*x^2+a3*x^3+a4*x^4+a5*x^5)+(b0+ b1*x+b2*x^2+b3*x^3)	
Plot	A	C
a0*	-4572.06806 ± 87.3635	-4572.06806 ± 87.36359
a1*	397.75582 ± 147.7608	397.75582 ± 147.7608
a2*	-261.15956 ± 38.00513	-261.15956 ± 38.00513
a3*	86.32924 ± 6.14309	86.32924 ± 6.14309
a4*	-7.82358 ± 0.6371	-7.82358 ± 0.6371
a5	0 ± 0	0 ± 0
b0*	24.64253 ± 0.30508	24.64253 ± 0.30508
b1*	-0.59756 ± 0.50804	-0.59756 ± 0.50804
b2*	0.00625 ± 0.12429	0.00625 ± 0.12429
b3	0 ± 0	0 ± 0
T	273 ± 0	298 ± 0
Reduced Chi-Sqr*	0.00271	
R-Square(COD)	0.99965	0.99879
R-Square(COD)*	0.99928	
Adj. R-Square*	0.99922	

Figure S34. Fitting of the C_2H_2 isotherm data for **SIFSIX-21-Ni** to the virial equation.

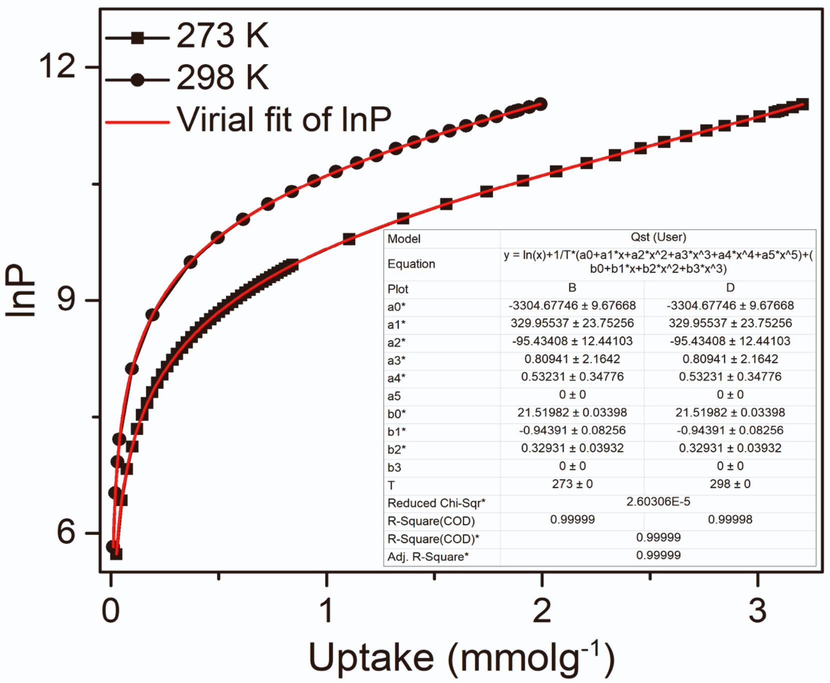

Model	Qst (User)	
Equation	y = ln(x)+1/T*(a0+a1*x+a2*x^2+a3*x^3+a4*x^4+a5*x^5)+(b0+b1*x+b2*x^2+b3*x^3)	
Plot	B	D
a0*	-3304.67746 ± 9.67668	-3304.67746 ± 9.67668
a1*	329.95537 ± 23.75256	329.95537 ± 23.75256
a2*	-95.43408 ± 12.44103	-95.43408 ± 12.44103
a3*	0.80941 ± 2.1642	0.80941 ± 2.1642
a4*	0.53231 ± 0.34776	0.53231 ± 0.34776
a5	0 ± 0	0 ± 0
b0*	21.51982 ± 0.03398	21.51982 ± 0.03398
b1*	-0.94391 ± 0.08256	-0.94391 ± 0.08256
b2*	0.32931 ± 0.03932	0.32931 ± 0.03932
b3	0 ± 0	0 ± 0
T	273 ± 0	298 ± 0
Reduced Chi-Sqr*	2.60306E-5	
R-Square(COD)	0.99999	0.99998
R-Square(COD)*	0.99999	
Adj. R-Square*	0.99999	

Figure S35. Fitting of the CO_2 isotherm data for **TIFSIX-4-Ni** to the virial equation.

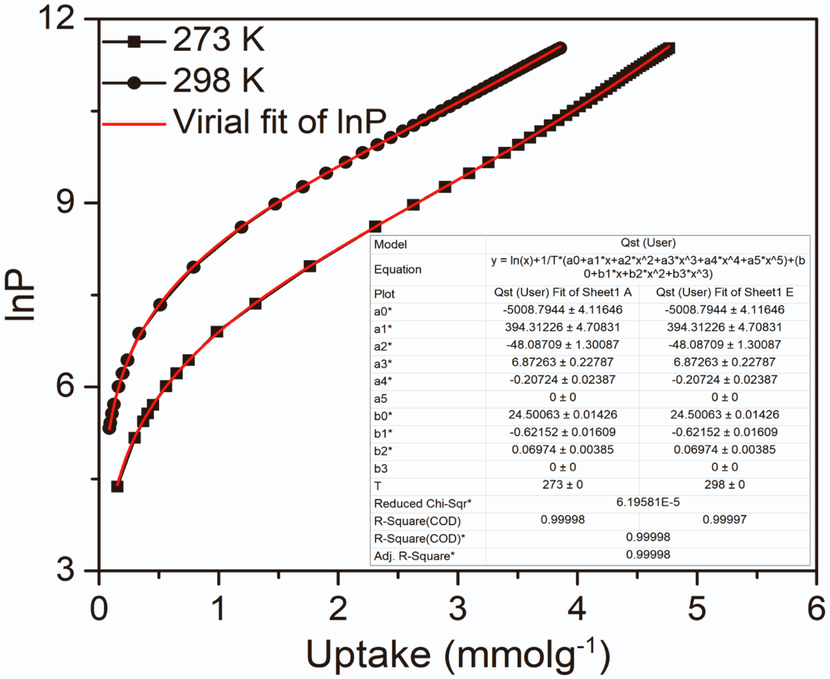

Model	Qst (User)	
Equation	y = ln(x)+1/T*(a0+a1*x+a2*x^2+a3*x^3+a4*x^4+a5*x^5)+(b0+b1*x+b2*x^2+b3*x^3)	
Plot	Qst (User) Fit of Sheet1 A	Qst (User) Fit of Sheet1 E
a0*	-5008.7944 ± 4.11646	-5008.7944 ± 4.11646
a1*	394.31226 ± 4.70831	394.31226 ± 4.70831
a2*	-48.08709 ± 1.30087	-48.08709 ± 1.30087
a3*	6.87263 ± 0.22787	6.87263 ± 0.22787
a4*	-0.20724 ± 0.02387	-0.20724 ± 0.02387
a5	0 ± 0	0 ± 0
b0*	24.50063 ± 0.01426	24.50063 ± 0.01426
b1*	-0.62152 ± 0.01609	-0.62152 ± 0.01609
b2*	0.06974 ± 0.00385	0.06974 ± 0.00385
b3	0 ± 0	0 ± 0
T	273 ± 0	298 ± 0
Reduced Chi-Sqr*	6.19581E-5	
R-Square(COD)	0.99998	0.99997
R-Square(COD)*	0.99998	
Adj. R-Square*	0.99998	

Figure S36. Fitting of the C_2H_2 isotherm data for **TIFSIX-4-Ni** to the virial equation.

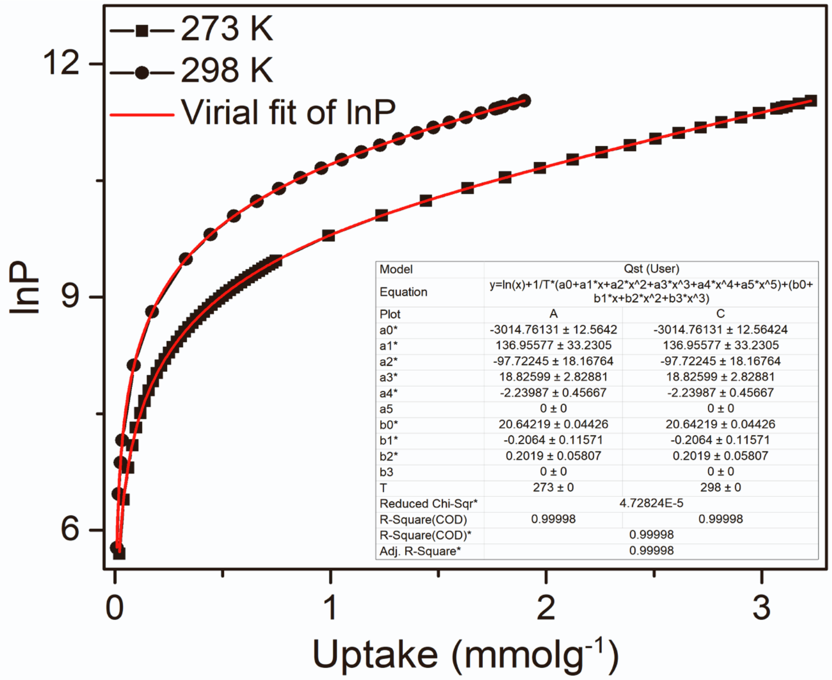

Model	Qst (User)	
Equation	y=ln(x)+1/T*(a0+a1*x+a2*x^2+a3*x^3+a4*x^4+a5*x^5)+(b0+b1*x+b2*x^2+b3*x^3)	
Plot	A	C
a0*	-3014.76131 ± 12.5642	-3014.76131 ± 12.56424
a1*	136.95577 ± 33.2305	136.95577 ± 33.2305
a2*	-97.72245 ± 18.16764	-97.72245 ± 18.16764
a3*	18.82599 ± 2.82881	18.82599 ± 2.82881
a4*	-2.23987 ± 0.45667	-2.23987 ± 0.45667
a5	0 ± 0	0 ± 0
b0*	20.64219 ± 0.04426	20.64219 ± 0.04426
b1*	-0.2064 ± 0.11571	-0.2064 ± 0.11571
b2*	0.2019 ± 0.05807	0.2019 ± 0.05807
b3	0 ± 0	0 ± 0
T	273 ± 0	298 ± 0
Reduced Chi-Sqr*	4.72824E-5	
R-Square(COD)	0.99998	0.99998
R-Square(COD)*	0.99998	
Adj. R-Square*	0.99998	

Figure S37. Fitting of the CO_2 isotherm data for **NbOFFIVE-3-Ni** to the virial equation.

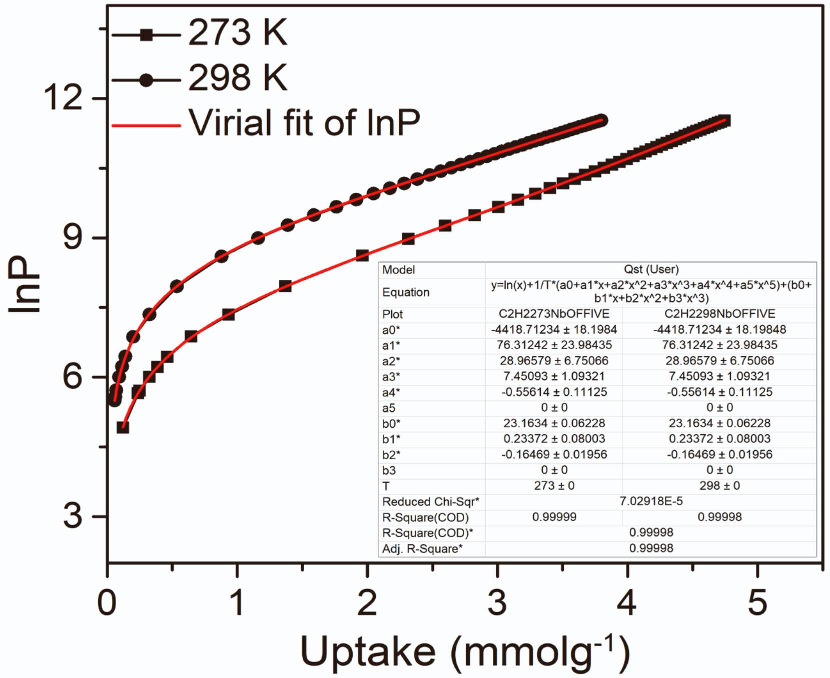

Model	Qst (User)	
Equation	y=ln(x)+1/T*(a0+a1*x+a2*x^2+a3*x^3+a4*x^4+a5*x^5)+(b0+b1*x+b2*x^2+b3*x^3)	
Plot	C2H2273NbOFFIVE	C2H2298NbOFFIVE
a0*	-4418.71234 ± 18.1984	-4418.71234 ± 18.19848
a1*	76.31242 ± 23.98435	76.31242 ± 23.98435
a2*	28.96579 ± 6.75066	28.96579 ± 6.75066
a3*	7.45093 ± 1.09321	7.45093 ± 1.09321
a4*	-0.55614 ± 0.11125	-0.55614 ± 0.11125
a5	0 ± 0	0 ± 0
b0*	23.1634 ± 0.06228	23.1634 ± 0.06228
b1*	0.23372 ± 0.08003	0.23372 ± 0.08003
b2*	-0.16469 ± 0.01956	-0.16469 ± 0.01956
b3	0 ± 0	0 ± 0
T	273 ± 0	298 ± 0
Reduced Chi-Sqr*	7.02918E-5	
R-Square(COD)	0.99999	0.99998
R-Square(COD)*	0.99998	
Adj. R-Square*	0.99998	

Figure S38. Fitting of the C_2H_2 isotherm data for **NbOFFIVE-3-Ni** to the virial equation.

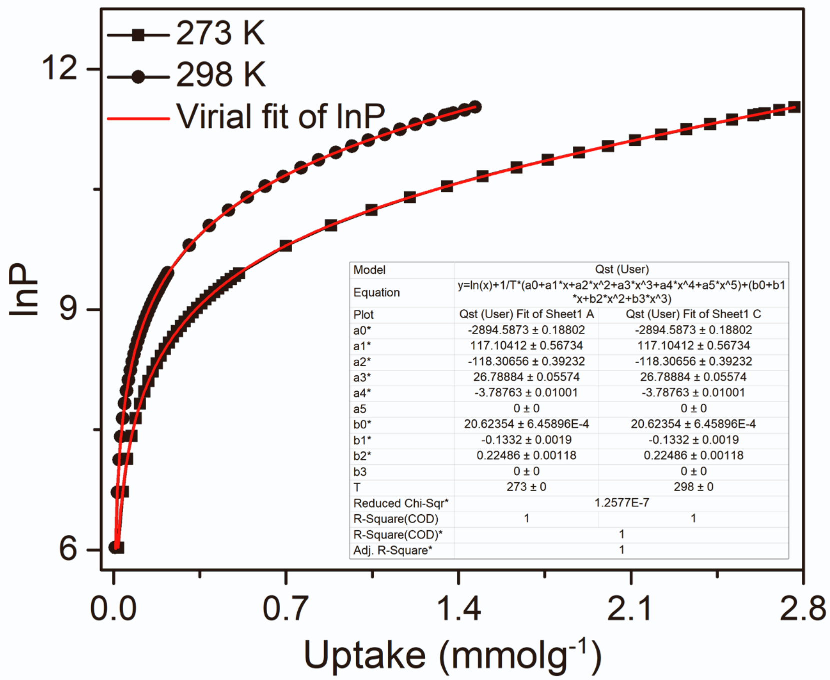

Model	Qst (User)	
Equation	y=ln(x)+1/T*(a0+a1*x+a2*x^2+a3*x^3+a4*x^4+a5*x^5)+(b0+b1*x+b2*x^2+b3*x^3)	
Plot	Qst (User) Fit of Sheet1 A	Qst (User) Fit of Sheet1 C
a0*	-2894.5873 ± 0.18802	-2894.5873 ± 0.18802
a1*	117.10412 ± 0.56734	117.10412 ± 0.56734
a2*	-118.30656 ± 0.39232	-118.30656 ± 0.39232
a3*	26.78884 ± 0.05574	26.78884 ± 0.05574
a4*	-3.78763 ± 0.01001	-3.78763 ± 0.01001
a5	0 ± 0	0 ± 0
b0*	20.62354 ± 6.45896E-4	20.62354 ± 6.45896E-4
b1*	-0.1332 ± 0.0019	-0.1332 ± 0.0019
b2*	0.22486 ± 0.00118	0.22486 ± 0.00118
b3	0 ± 0	0 ± 0
T	273 ± 0	298 ± 0
Reduced Chi-Sqr*	1.2577E-7	
R-Square(COD)	1	1
R-Square(COD)*	1	
Adj. R-Square*	1	

Figure S39. Fitting of the CO_2 isotherm data for **SIFSIX-21-Cu** to the virial equation.

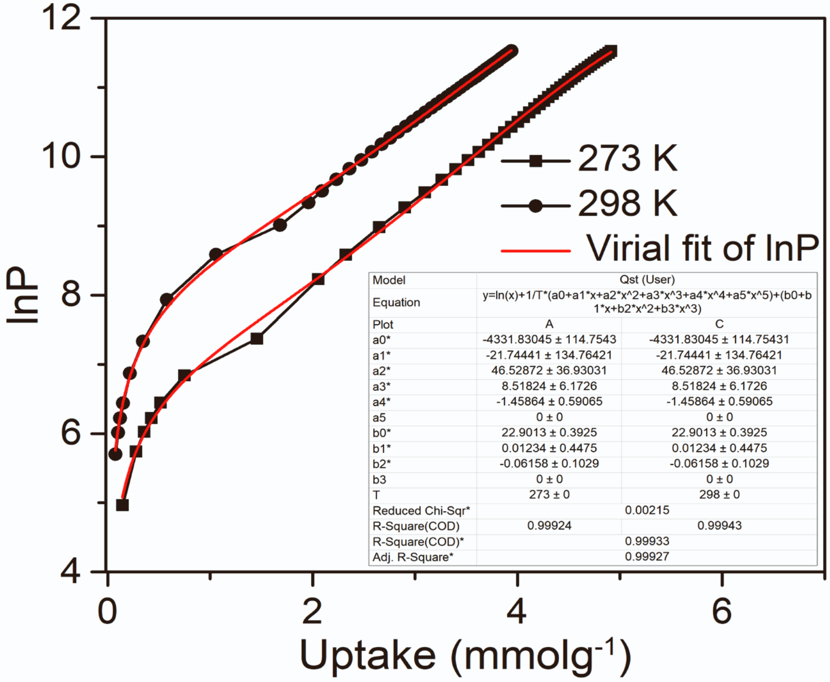

Model	Qst (User)	
Equation	y=ln(x)+1/T*(a0+a1*x+a2*x^2+a3*x^3+a4*x^4+a5*x^5)+(b0+b1*x+b2*x^2+b3*x^3)	
Plot	A	C
a0*	-4331.83045 ± 114.7543	-4331.83045 ± 114.75431
a1*	-21.74441 ± 134.76421	-21.74441 ± 134.76421
a2*	46.52872 ± 36.93031	46.52872 ± 36.93031
a3*	8.51824 ± 6.1726	8.51824 ± 6.1726
a4*	-1.45864 ± 0.59065	-1.45864 ± 0.59065
a5	0 ± 0	0 ± 0
b0*	22.9013 ± 0.3925	22.9013 ± 0.3925
b1*	0.01234 ± 0.4475	0.01234 ± 0.4475
b2*	-0.06158 ± 0.1029	-0.06158 ± 0.1029
b3	0 ± 0	0 ± 0
T	273 ± 0	298 ± 0
Reduced Chi-Sqr*	0.00215	
R-Square(COD)	0.99924	0.99943
R-Square(COD)*	0.99933	
Adj. R-Square*	0.99927	

Figure S40. Fitting of the C_2H_2 isotherm data for **SIFSIX-21-Cu** to the virial equation.

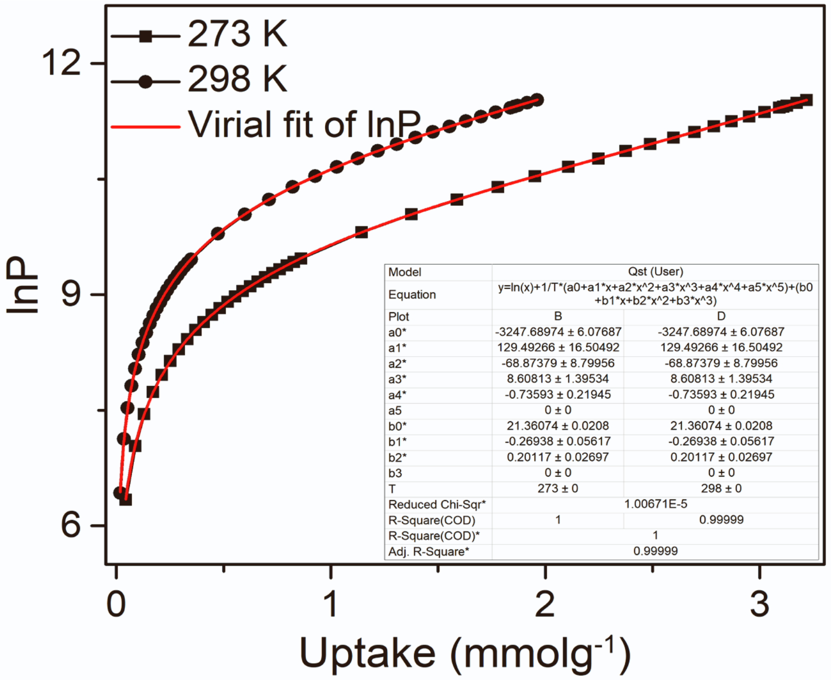

Model	Qst (User)	
Equation	y=ln(x)+1/T*(a0+a1*x+a2*x^2+a3*x^3+a4*x^4+a5*x^5)+(b0 +b1*x+b2*x^2+b3*x^3)	
Plot	B	D
a0*	-3247.68974 ± 6.07687	-3247.68974 ± 6.07687
a1*	129.49266 ± 16.50492	129.49266 ± 16.50492
a2*	-68.87379 ± 8.79956	-68.87379 ± 8.79956
a3*	8.60813 ± 1.39534	8.60813 ± 1.39534
a4*	-0.73593 ± 0.21945	-0.73593 ± 0.21945
a5	0 ± 0	0 ± 0
b0*	21.36074 ± 0.0208	21.36074 ± 0.0208
b1*	-0.26938 ± 0.05617	-0.26938 ± 0.05617
b2*	0.20117 ± 0.02697	0.20117 ± 0.02697
b3	0 ± 0	0 ± 0
T	273 ± 0	298 ± 0
Reduced Chi-Sqr*	1.00671E-5	
R-Square(COD)	1	0.99999
R-Square(COD)*	1	
Adj. R-Square*	0.99999	

Figure S41. Fitting of the CO_2 isotherm data for **TIFSIX-4-Cu** to the virial equation.

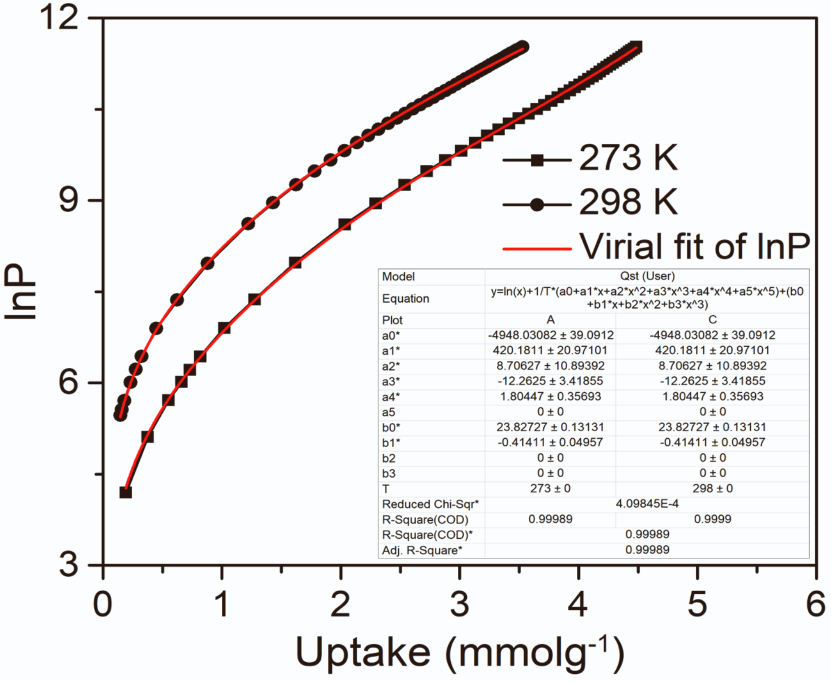

Model	Qst (User)	
Equation	y=ln(x)+1/T*(a0+a1*x+a2*x^2+a3*x^3+a4*x^4+a5*x^5)+(b0 +b1*x+b2*x^2+b3*x^3)	
Plot	A	C
a0*	-4948.03082 ± 39.0912	-4948.03082 ± 39.0912
a1*	420.1811 ± 20.97101	420.1811 ± 20.97101
a2*	8.70627 ± 10.89392	8.70627 ± 10.89392
a3*	-12.2625 ± 3.41855	-12.2625 ± 3.41855
a4*	1.80447 ± 0.35693	1.80447 ± 0.35693
a5	0 ± 0	0 ± 0
b0*	23.82727 ± 0.13131	23.82727 ± 0.13131
b1*	-0.41411 ± 0.04957	-0.41411 ± 0.04957
b2	0 ± 0	0 ± 0
b3	0 ± 0	0 ± 0
T	273 ± 0	298 ± 0
Reduced Chi-Sqr*	4.09845E-4	
R-Square(COD)	0.99989	0.9999
R-Square(COD)*	0.99989	
Adj. R-Square*	0.99989	

Figure S42. Fitting of the C_2H_2 isotherm data for **TIFSIX-4-Cu** to the virial equation.

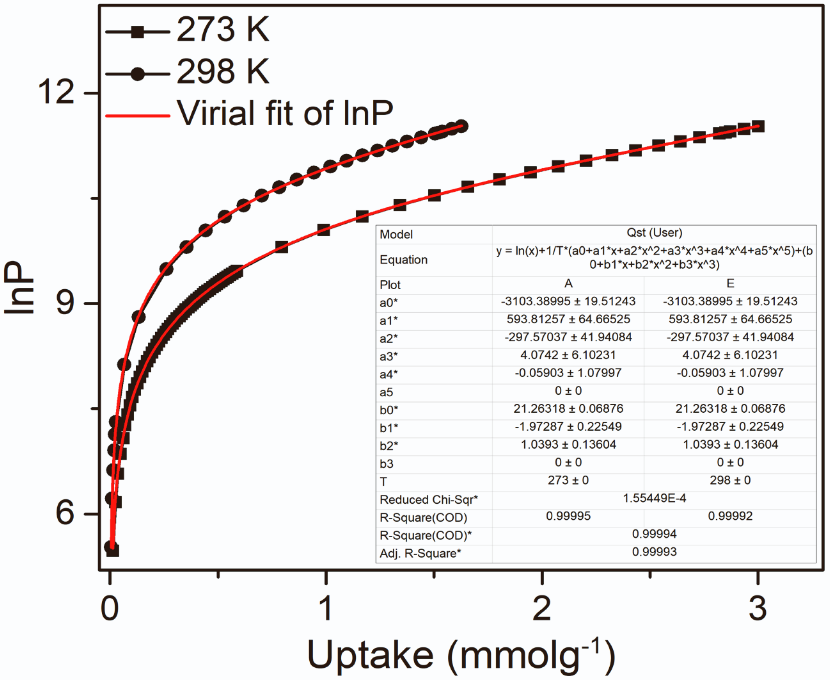

Model	Qst (User)	
Equation	y = ln(x)+1/T*(a0+a1*x+a2*x^2+a3*x^3+a4*x^4+a5*x^5)+(b0+b1*x+b2*x^2+b3*x^3)	
Plot	A	E
a0*	-3103.38995 ± 19.51243	-3103.38995 ± 19.51243
a1*	593.81257 ± 64.66525	593.81257 ± 64.66525
a2*	-297.57037 ± 41.94084	-297.57037 ± 41.94084
a3*	4.0742 ± 6.10231	4.0742 ± 6.10231
a4*	-0.05903 ± 1.07997	-0.05903 ± 1.07997
a5	0 ± 0	0 ± 0
b0*	21.26318 ± 0.06876	21.26318 ± 0.06876
b1*	-1.97287 ± 0.22549	-1.97287 ± 0.22549
b2*	1.0393 ± 0.13604	1.0393 ± 0.13604
b3	0 ± 0	0 ± 0
T	273 ± 0	298 ± 0
Reduced Chi-Sqr*	1.55449E-4	
R-Square(COD)	0.99995	0.99992
R-Square(COD)*	0.99994	
Adj. R-Square*	0.99993	

Figure S43. Fitting of the CO_2 isotherm data for **NbOFFIVE-3-Cu** to the virial equation.

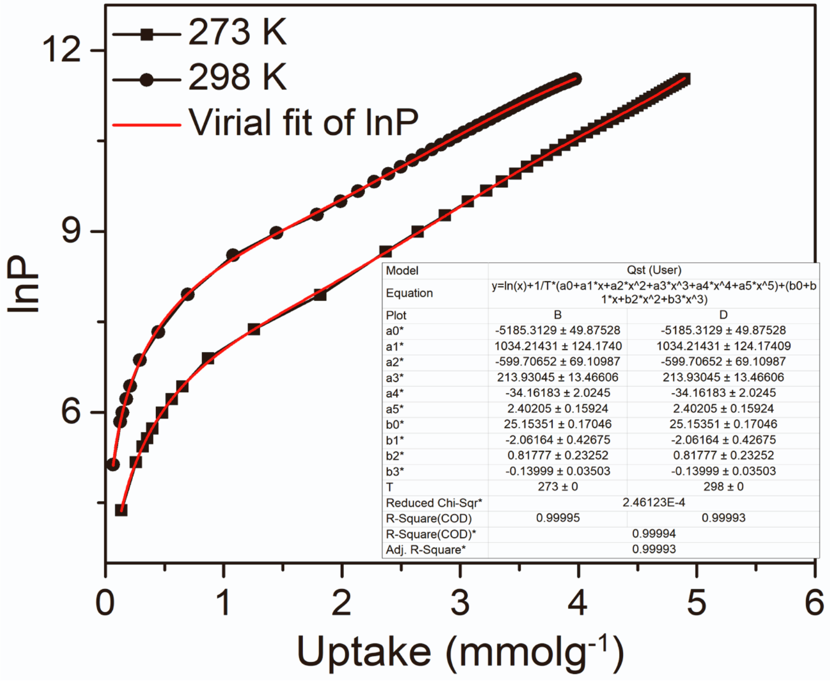

Model	Qst (User)	
Equation	y=ln(x)+1/T*(a0+a1*x+a2*x^2+a3*x^3+a4*x^4+a5*x^5)+(b0+b1*x+b2*x^2+b3*x^3)	
Plot	B	D
a0*	-5185.3129 ± 49.87528	-5185.3129 ± 49.87528
a1*	1034.21431 ± 124.1740	1034.21431 ± 124.17409
a2*	-599.70652 ± 69.10987	-599.70652 ± 69.10987
a3*	213.93045 ± 13.46606	213.93045 ± 13.46606
a4*	-34.16183 ± 2.0245	-34.16183 ± 2.0245
a5*	2.40205 ± 0.15924	2.40205 ± 0.15924
b0*	25.15351 ± 0.17046	25.15351 ± 0.17046
b1*	-2.06164 ± 0.42675	-2.06164 ± 0.42675
b2*	0.81777 ± 0.23252	0.81777 ± 0.23252
b3*	-0.13999 ± 0.03503	-0.13999 ± 0.03503
T	273 ± 0	298 ± 0
Reduced Chi-Sqr*	2.46123E-4	
R-Square(COD)	0.99995	0.99993
R-Square(COD)*	0.99994	
Adj. R-Square*	0.99993	

Figure S44. Fitting of the C_2H_2 isotherm data for **NbOFFIVE-3-Cu** to the virial equation.

IAST(S_{AC}) data.

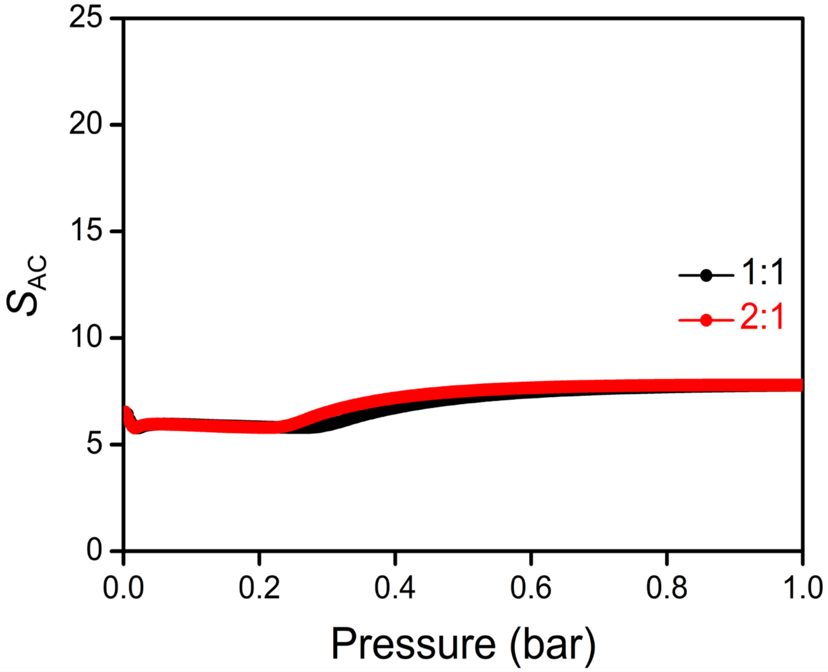

Figure S45. Selectivity for C_2H_2 and CO_2, S_{AC} (1:1 and 2:1 gas mixtures) to 1 bar and 298 K, as calculated by IAST for **SIFSIX-21-Ni**.

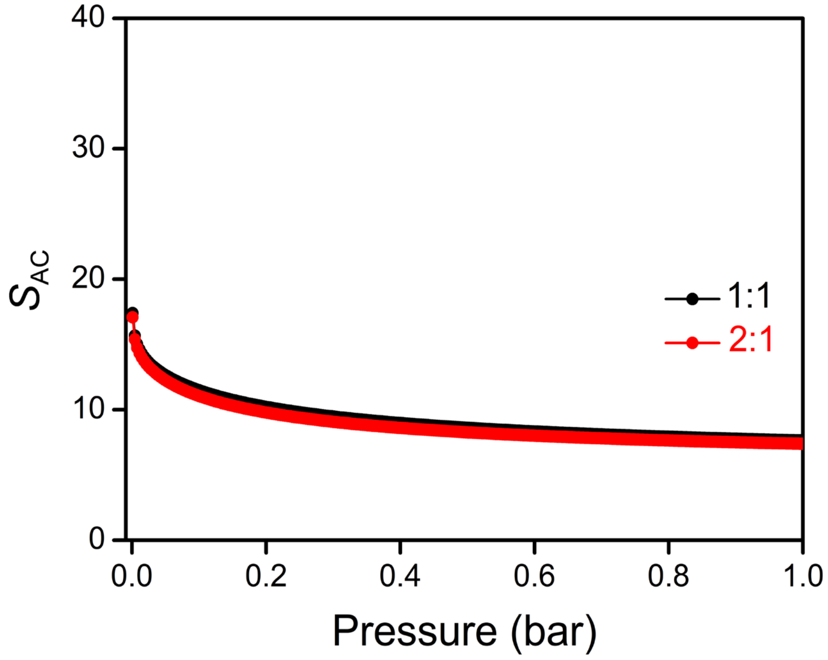

Figure S46. Selectivity for C_2H_2 and CO_2, S_{AC} (1:1 and 2:1 gas mixtures) to 1 bar and 298 K, as calculated by IAST for **TIFSIX-4-Ni**.

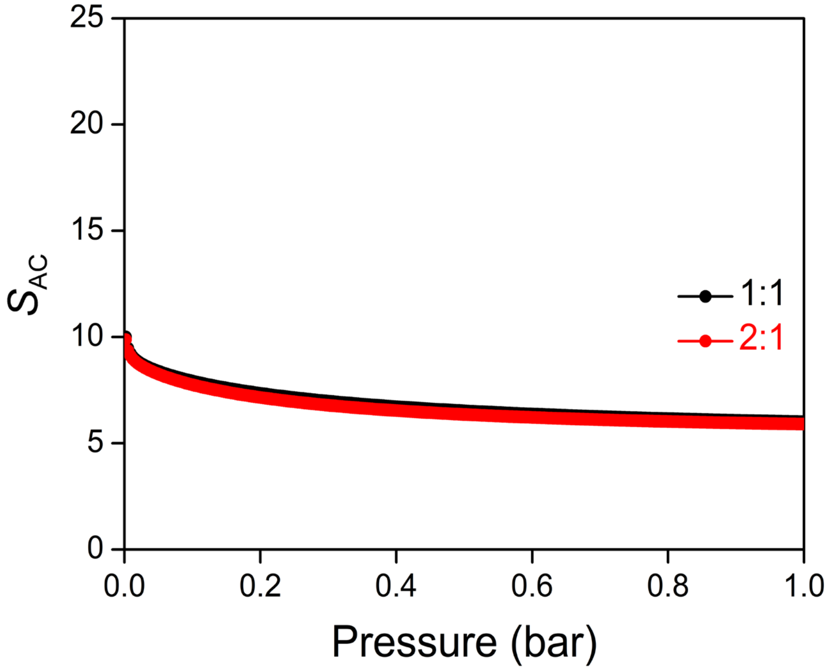

Figure S47. Selectivity for C_2H_2 and CO_2, S_{AC} (1:1 and 2:1 gas mixtures) to 1 bar and 298 K, as calculated by IAST for **NbOFFIVE-3-Ni**.

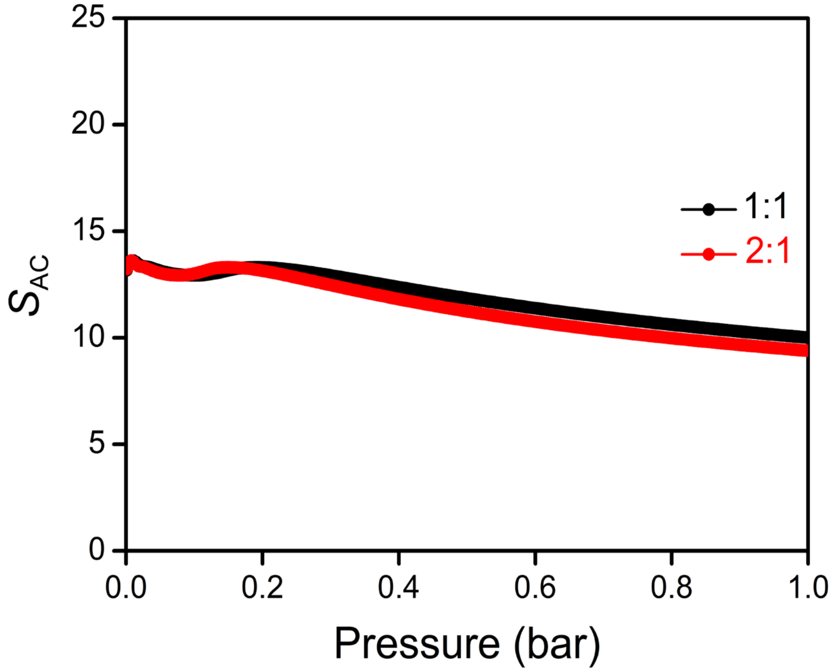

Figure S48. Selectivity for C_2H_2 and CO_2, S_{AC} (1:1 and 2:1 gas mixtures) to 1 bar and 298 K, as calculated by IAST for **SIFSIX-21-Cu**.

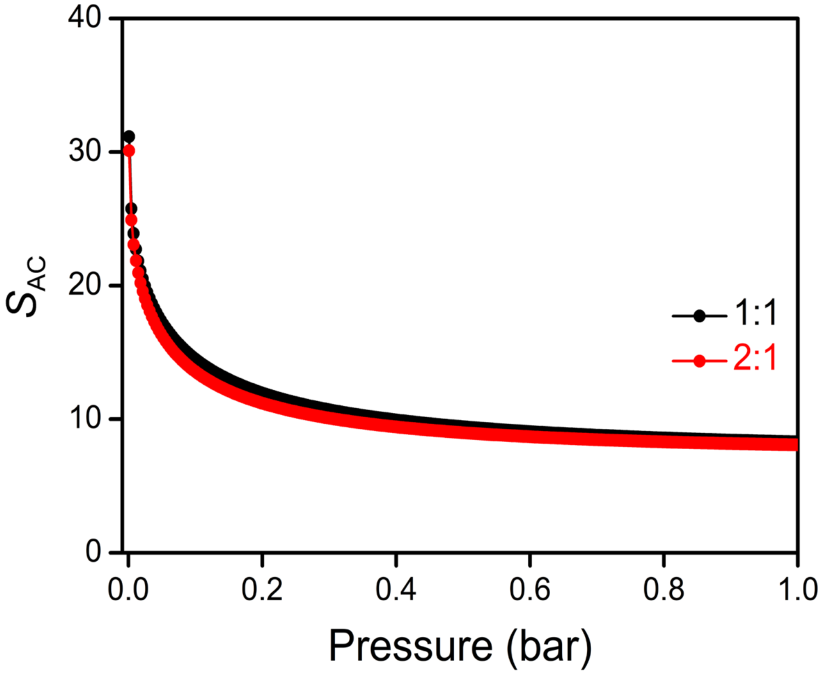

Figure S49. Selectivity for C_2H_2 and CO_2, S_{AC} (1:1 and 2:1 gas mixtures) to 1 bar and 298 K, as calculated by IAST for **TIFSIX-4-Cu**.

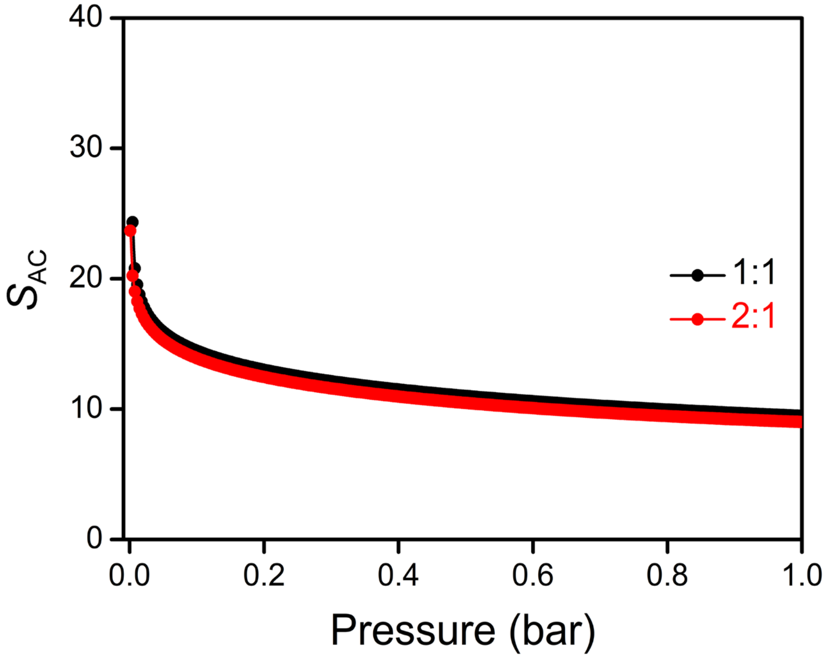

Figure S50. Selectivity for C_2H_2 and CO_2, S_{AC} (1:1 and 2:1 gas mixtures) to 1 bar and 298 K, as calculated by IAST for **NbOFFIVE-3-Cu**.

Mixed isotherms.

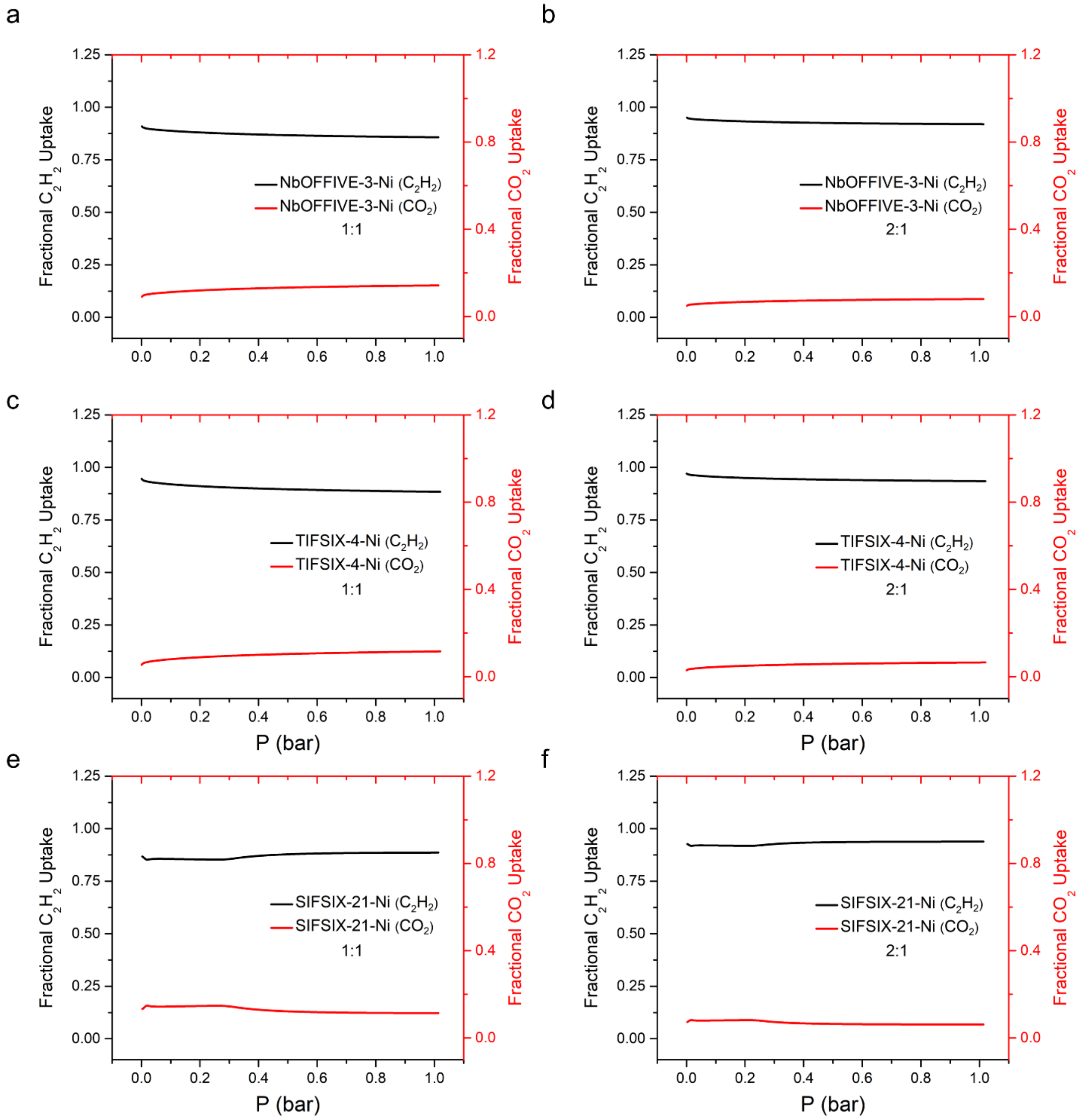

Figure S51. IAST calculations for C_2H_2 and CO_2 uptake capacities for equimolar(1:1) and 2:1 C_2H_2/CO_2 mixtures (X-axis refers to the total gas phase pressure in bar and Y-axis refers to fractional loading of the gases) at 298 K, for (a, b) **NbOFFIVE-3-Ni**, (c, d) **TIFSIX-4-Ni** and (e, f) **SIFSIX-21-Ni**.

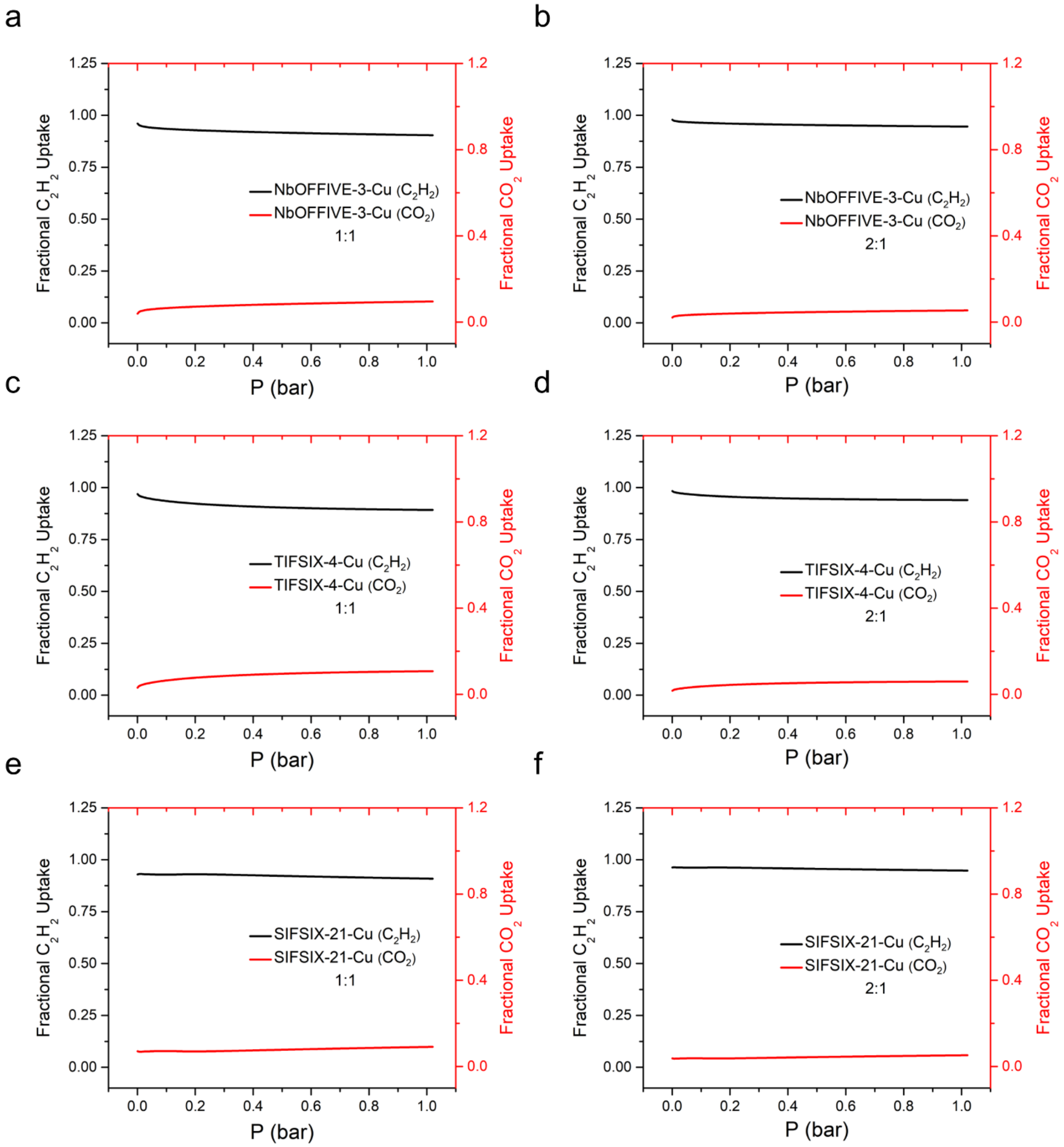

Figure S52. IAST calculations for C_2H_2 and CO_2 uptake capacities for equimolar (v/v = 1:1) and 2:1 (v/v) C_2H_2/CO_2 mixtures (X-axis refers to the total gas phase pressure in bar and Y-axis refers to fractional loading of the gases) at 298 K, for (a, b) **NbOFFIVE-3-Cu**, (c, d) **TIFSIX-4-Cu** and (e, f) **SIFSIX-21-Cu**.

Binding sites.

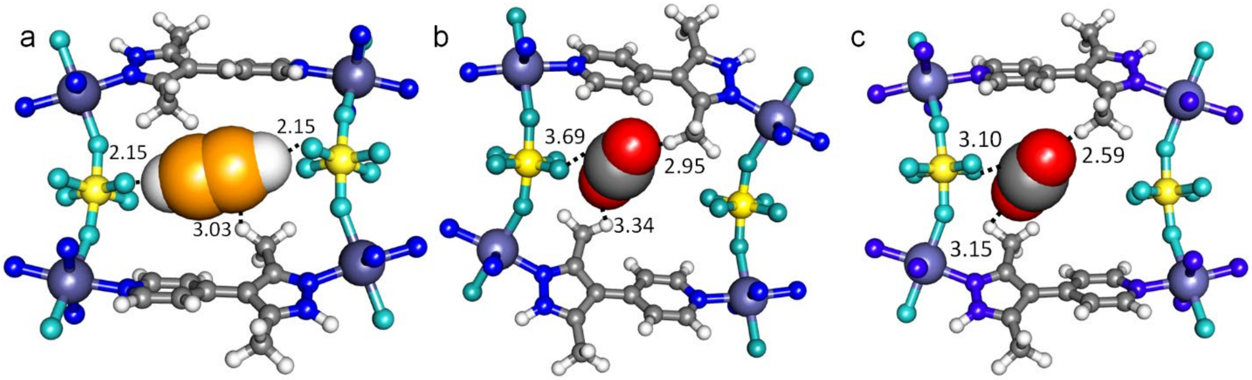

Figure S53. Plausible binding sites for **SIFSIX-21-Ni**, for C_2H_2 (a) and (b, c) CO_2.

Kinetic studies

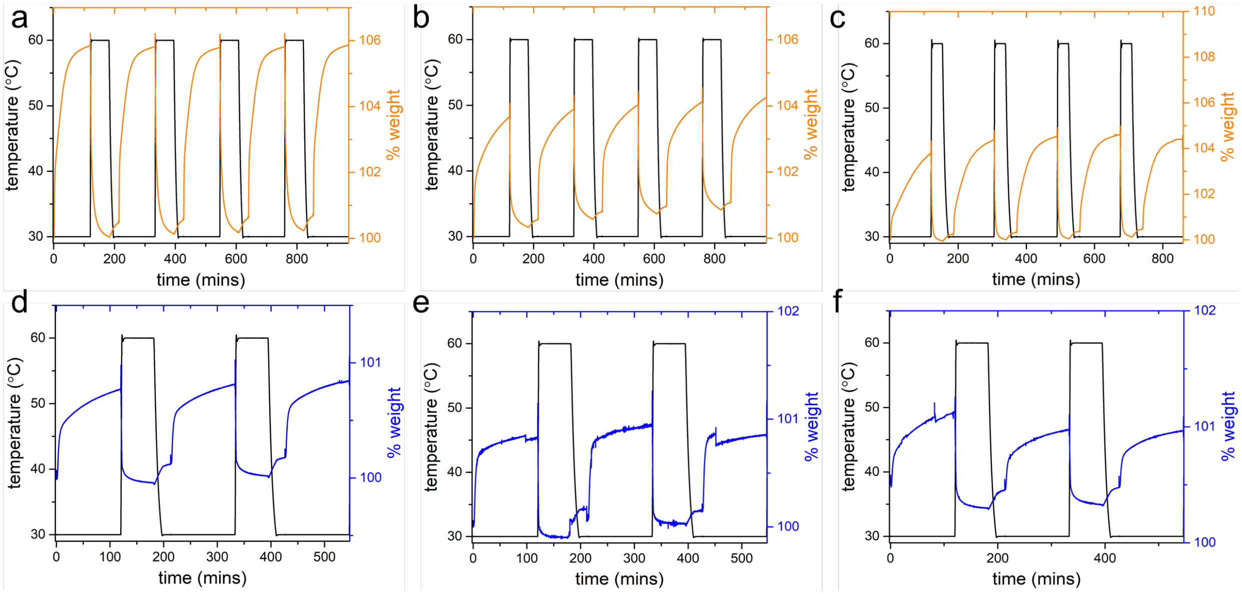

Figure S54. C_2H_2 kinetic plots for a) **SIFSIX-21-Ni**, b) **TIFSIX-4-Ni** and c) **NbOFFIVE-3-Ni**; CO_2 kinetic plots for d) **SIFSIX-21-Ni**, e) **TIFSIX-4-Ni** and f) **NbOFFIVE-3-Ni**.

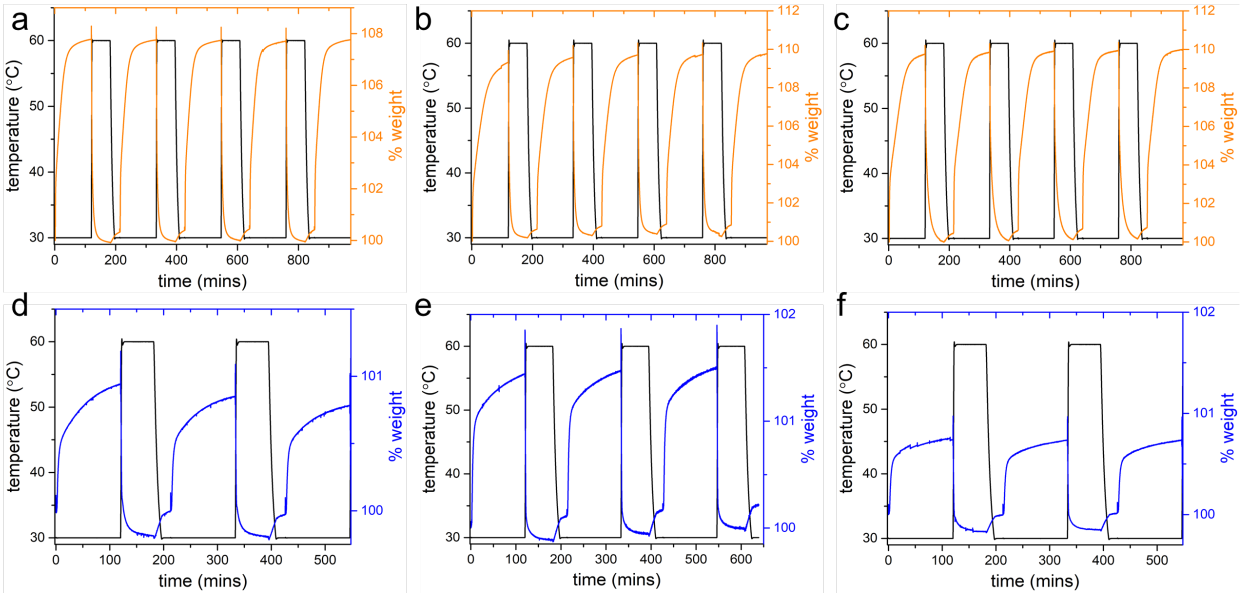

Figure S55. C_2H_2 kinetic plots for a) **SIFSIX-21-Cu**, b) **TIFSIX-4-Cu** and c) **NbOFFIVE-3-Cu**; CO_2 kinetic plots for d) **SIFSIX-21-Cu**, e) **TIFSIX-4-Cu** and f) **NbOFFIVE-3-Cu**.

Dynamic gas breakthrough separation experimental setup.

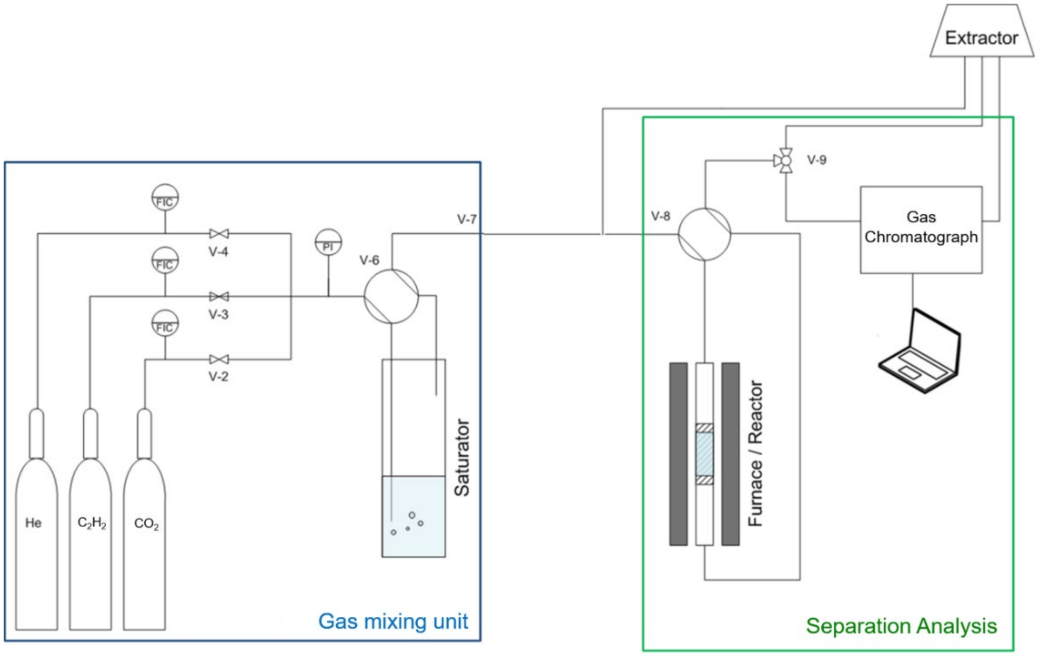

Figure S56. Schematic of gas mixing unit, gravimetric gas uptake analyser and gas separation analyser for breakthrough experiments.

Temperature programmed desorption.

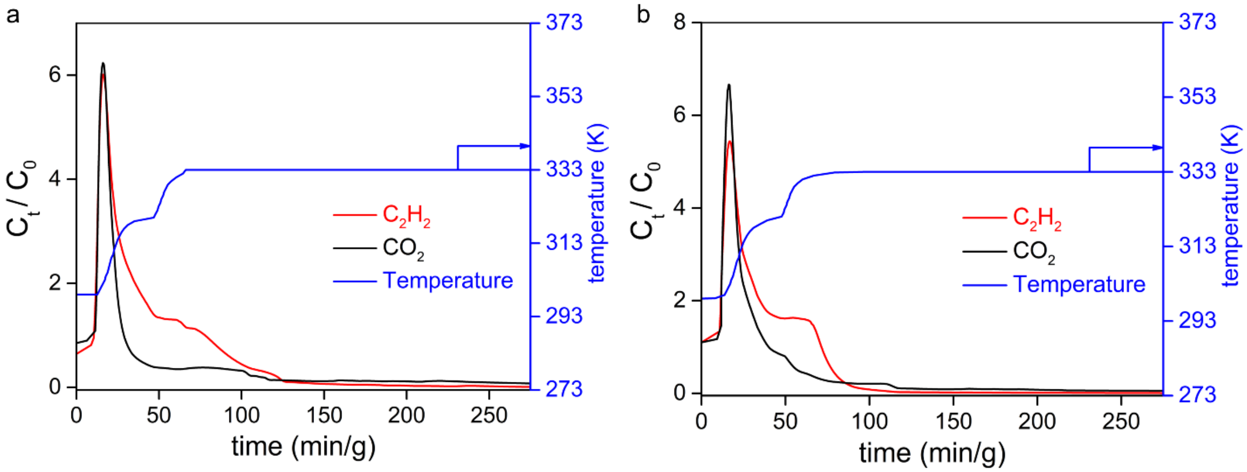

Figure S57. Temperature programmed desorption experiments conducted on a) **SIFSIX-21-Ni**; b) **NbOFFIVE-3-Cu** packed beds. Desorption temperature was set at 60 °C (set along the blue profile) and the He flow was maintained at 20 cm^3 min^{-1}.

Q_{st}(C_2H_2) comparison.

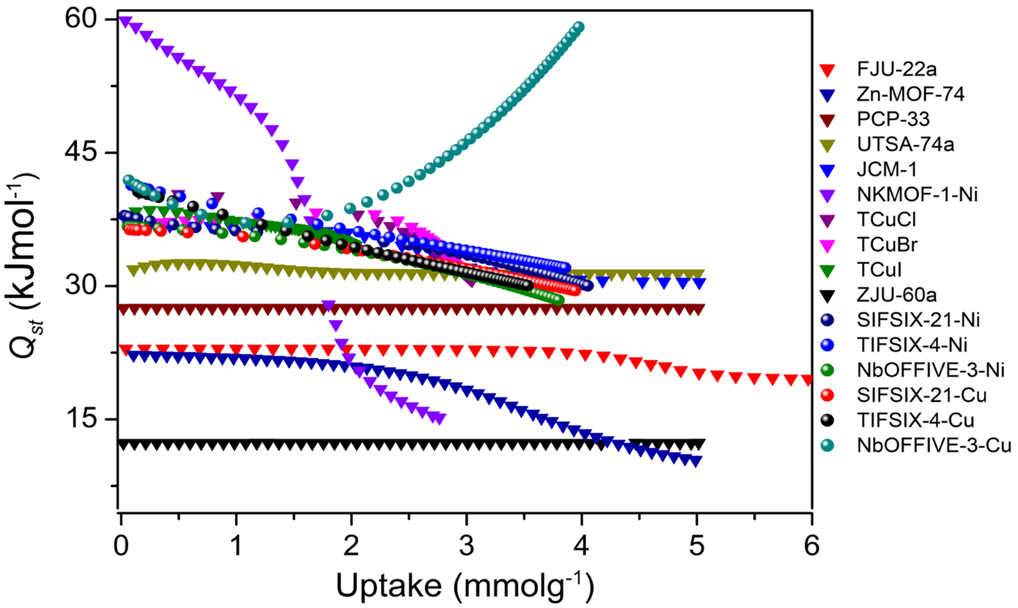

Figure S58. Comparison of isosteric heat of adsorption profiles for C_2H_2, considering all the C_2H_2/CO_2 separating MOM physisorbents.

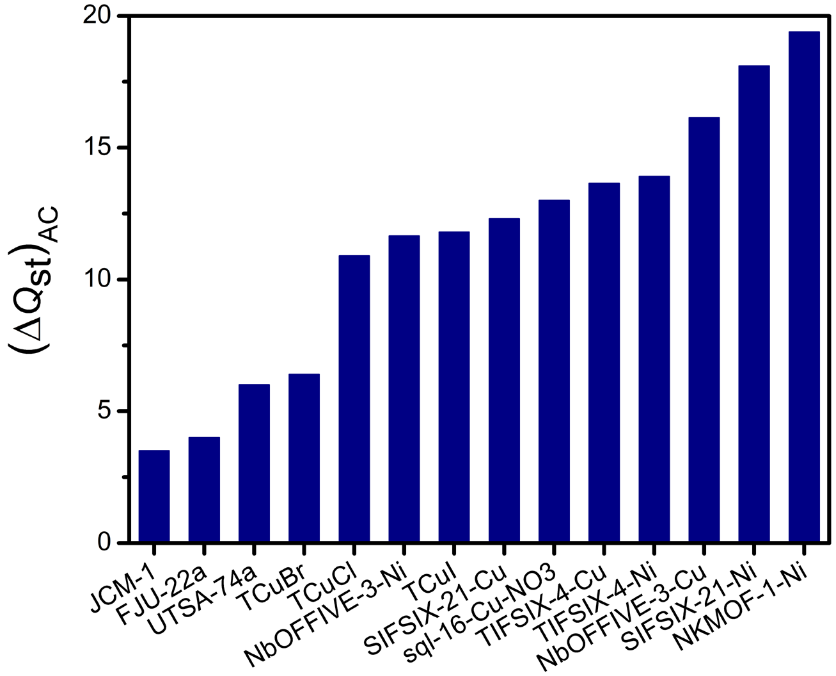

Figure S59. Comparison of ΔQ_{st}(C_2H_2/CO_2) at low loading, considering all the C_2H_2/CO_2 separating MOM physisorbents.

***In situ* Infrared (IR) spectra.**

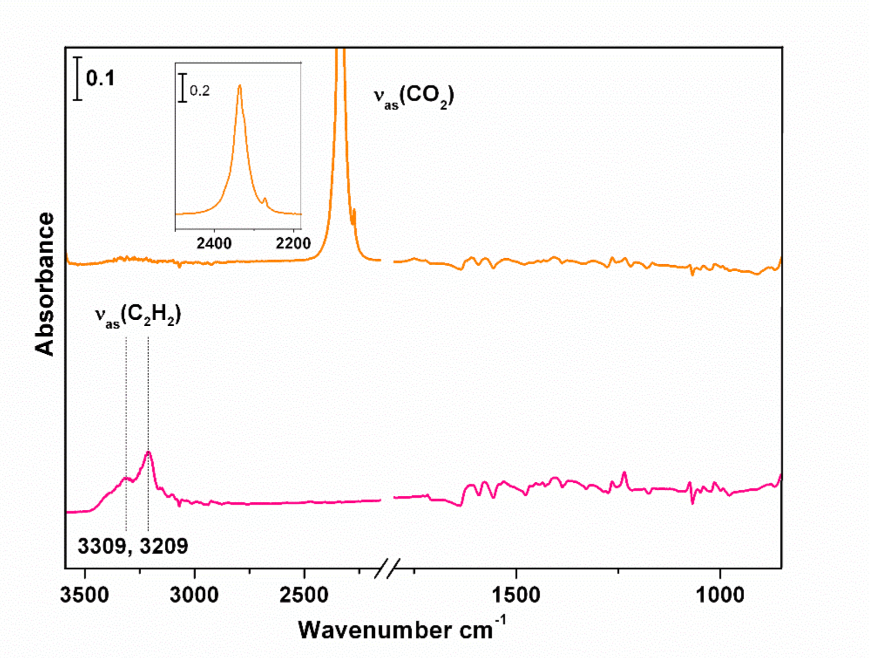

Figure. S60. Difference IR spectra showing the adsorbed CO_2 (orange) and C_2H_2 (pink) upon loading at 1 bar adsorbate pressure into **SIFSIX-21-Ni** and subsequent evacuation of the gas phase within 3 seconds, respectively. Each is referenced to the spectrum of activated HUMs. Inset shows the $\nu_{as}(CO_2)$ band.

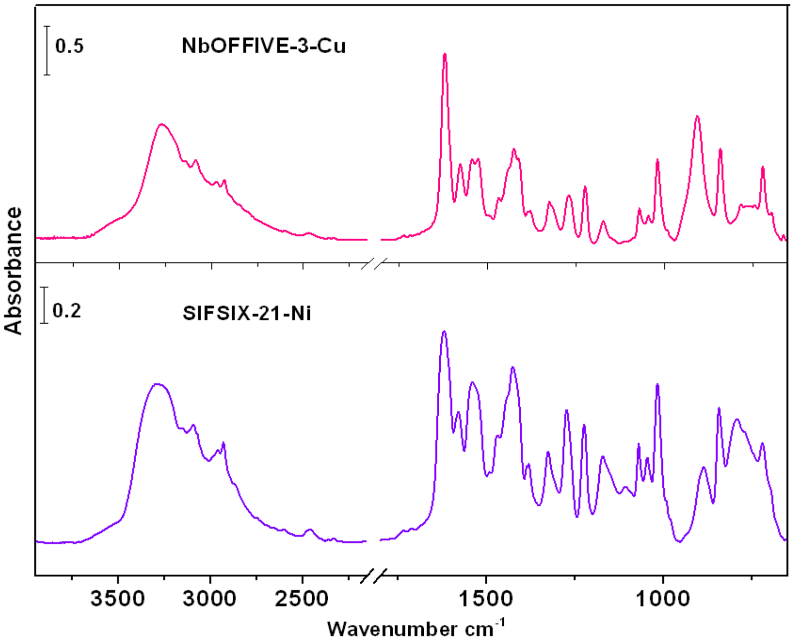

Figure S61. IR spectra of activated **NbOFFIVE-3-Cu** (top) and **SIFSIX-21-Ni** (bottom), referenced to pure KBr pellet in vacuum (< 2.66645 ×10^{-5} bar base pressure).

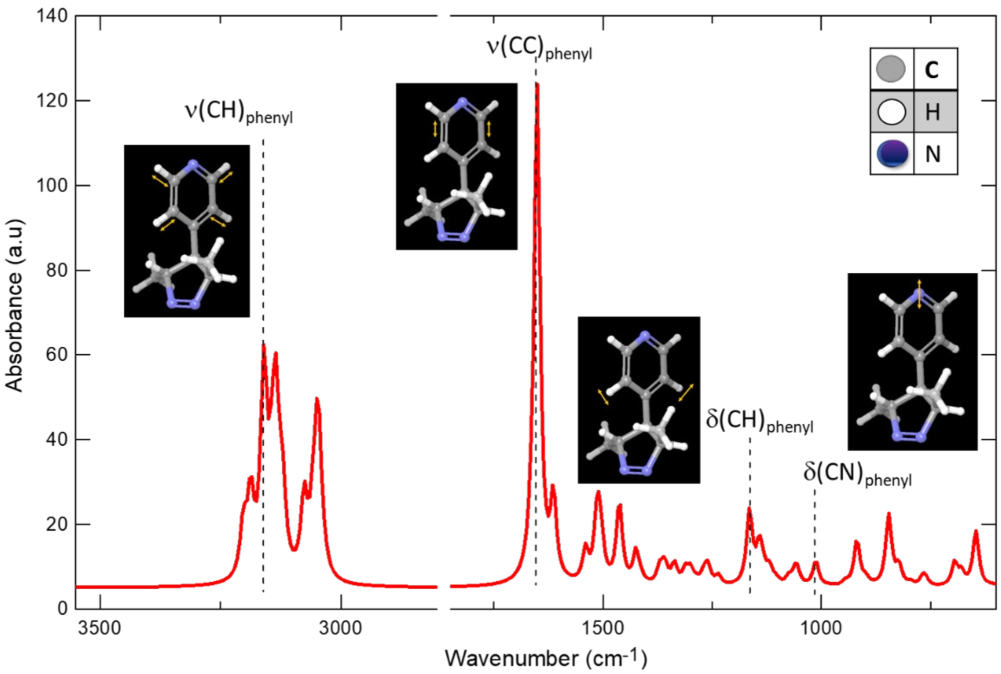

Figure S62. IR spectrum of pypz from DFT calculation.

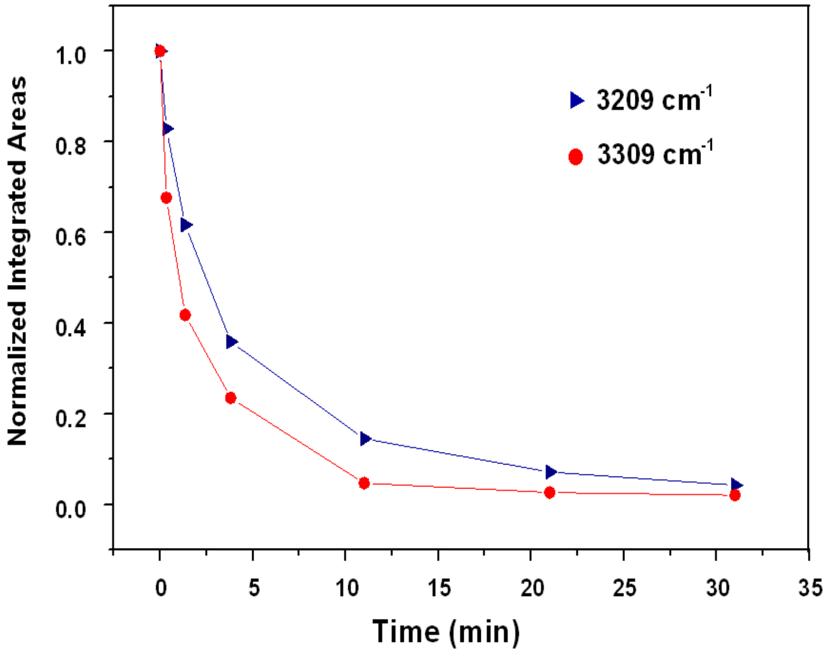

Figure S63. Evolution of the ν_{as}(C_2H_2) bands at 3308 (triangle) and 3209 cm^{-1} (circle) in **NbOFFIVE-3-Cu** under vacuum.

Solid-state NMR spectra

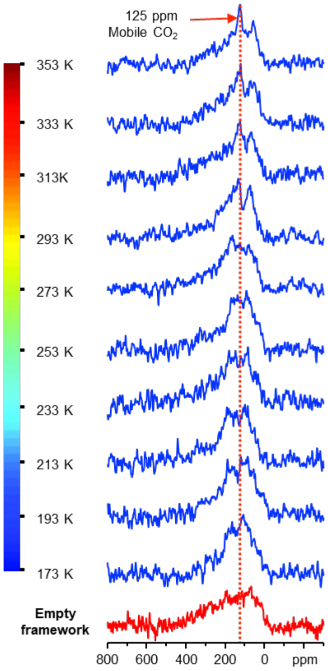

Figure S64. Experimental ^{13}C static NMR spectra of $^{13}CO_2$ adsorbed in **NbOFFIVE-3-Cu** as a function of temperature (blue line) and the spectrum of activated **NbOFFIVE-3-Cu** (red line).

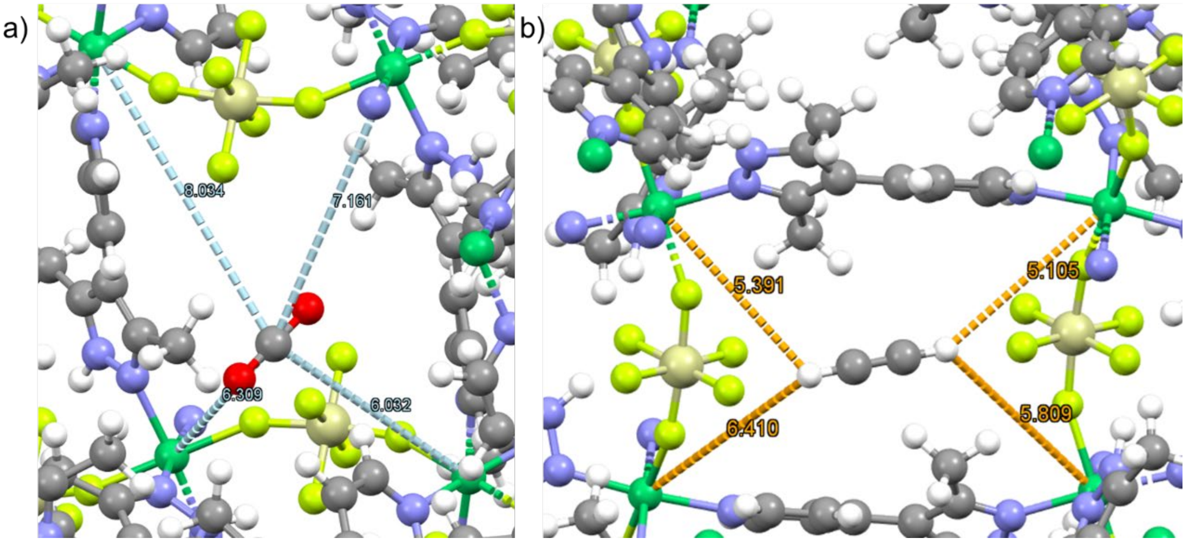

Figure S65. a) Modelled structure of **NbOFFIVE-3-Cu** showing the distances between the $C^{\delta+}$ of CO_2 and the nearby Cu(II) centres. b) Modelled structure of **NbOFFIVE-3-Cu** showing the distances between the H atoms in C_2H_2 and the nearby Cu(II) centres. Note: the structure of **SIFSIX-21-Ni** is used instead of the isostructural HUM **NbOFFIVE-3-Cu**.

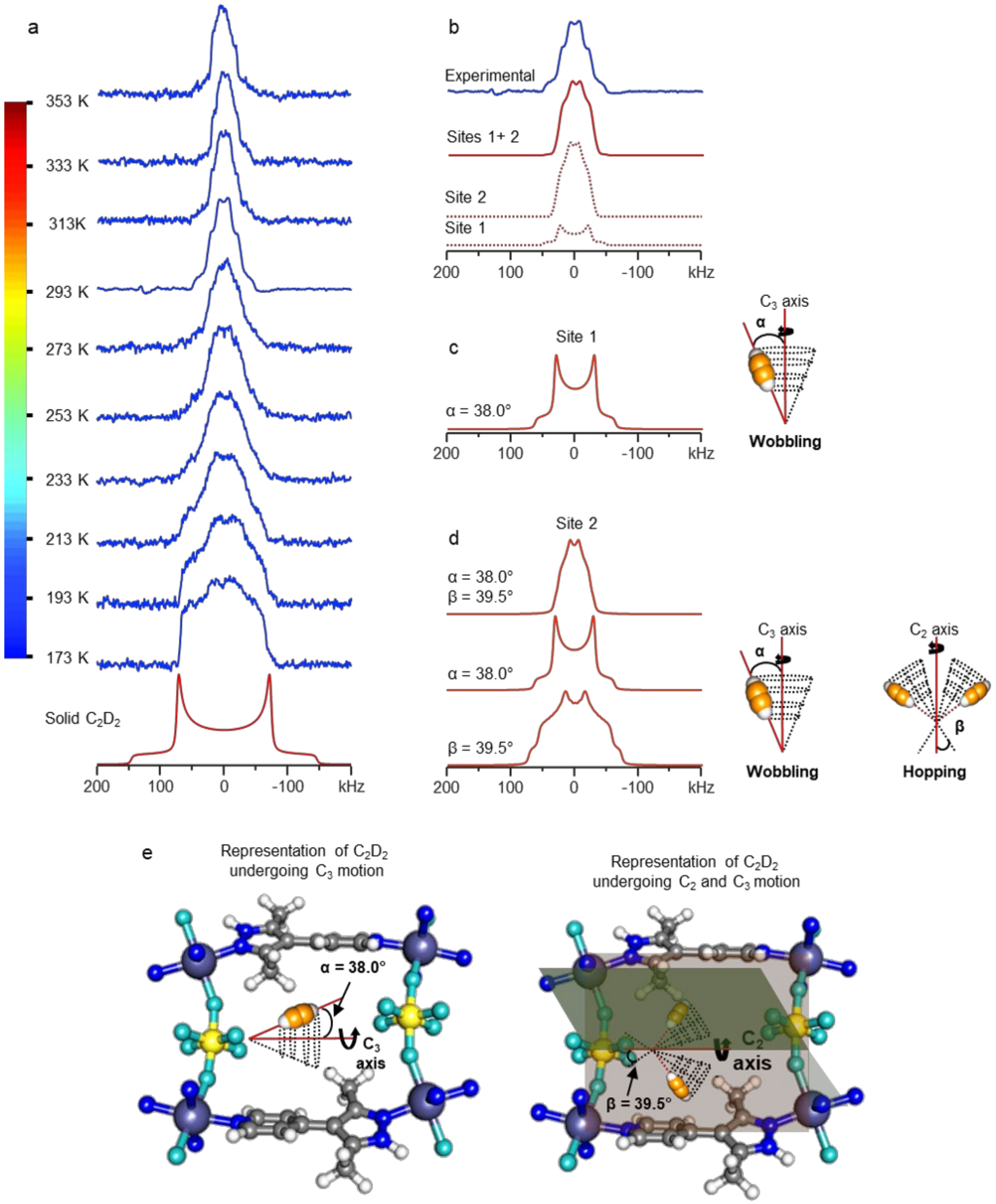

Figure S66. a) Experimental ^{2}H static spectra of 0.4 C_2D_2 per Cu adsorbed in **NbOFFIVE-3-Cu** as a function of temperature (blue line) and simulated ^{2}H spectrum of static C_2D_2. b) Experimental (blue) and simulated static ^{2}H spectra showing two different sites. c) Simulated ^{2}H spectra of C_2D_2 at site 1. Dynamical model for simulation: rotation of the C_2D_2 about a C_3 axis. d) Simulated ^{2}H spectra of C_2D_2 at site 2. Dynamical model for simulation: rotation of the C_2D_2 about a C_3 axis followed by a two-site hopping motion. e) Illustration of the dynamical models of C_2D_2 within **NbOFFIVE-3-Cu**. Note: the structure of **SIFSIX-21-Ni** is used instead of the isostructural HUM **NbOFFIVE-3-Cu**.

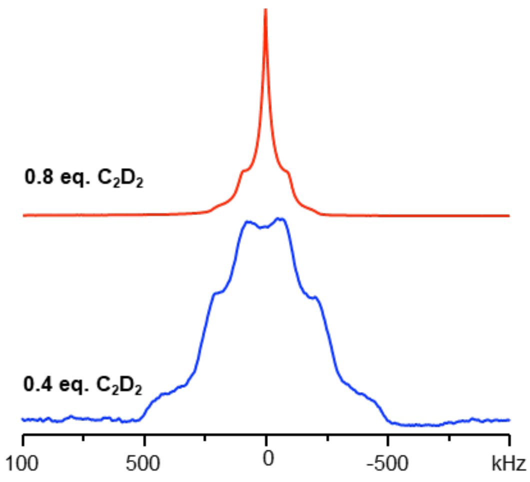

Figure S67. Comparison of experimental ^{2}H static NMR spectra of **NbOFFIVE-3-Cu** loaded with 0.4 and 0.8 C_2D_2 per Cu at room temperature.

Accelerated Stability Tests.

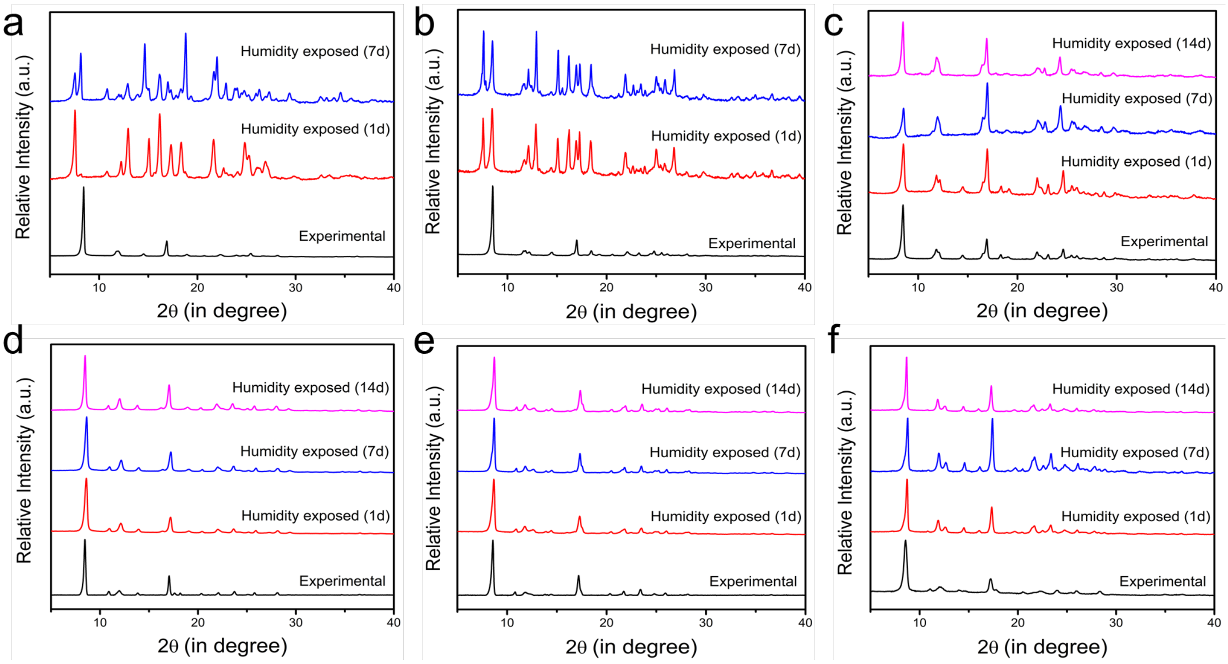

Figure S68. Comparison of experimental and calculated PXRD patterns with those of the three distinct humidity exposed phases: 1, 7 and 14 days a: **SIFSIX-21-Ni**, b: **TIFSIX-4-Ni**, c: **NbOFFIVE-3-Ni**, d: **SIFSIX-21-Cu**, e: **TIFSIX-4-Cu**, f: **NbOFFIVE-3-Cu**.

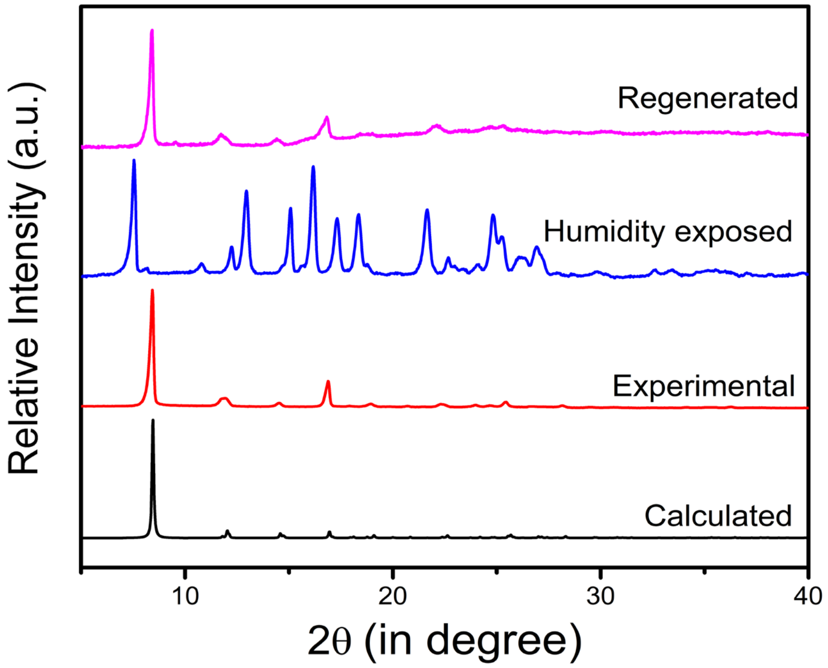

Figure S69. PXRD patterns of calculated (black), as-synthesised samples (red), the samples after exposed to humidity for a day (blue) and the regenerated **SIFSIX-21-Ni** (pink) in methanol solution.

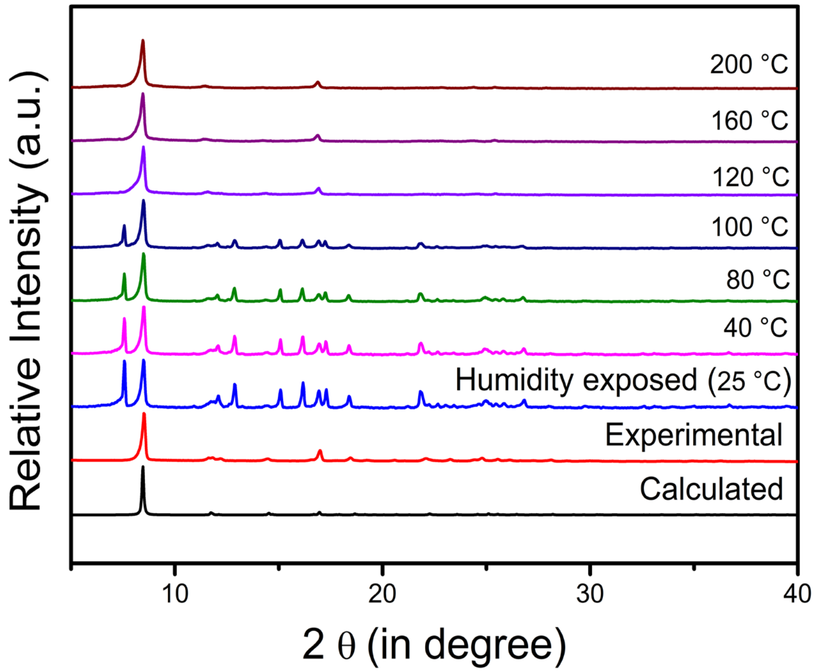

Figure S70. VT-PXRD profiles for humidity exposed samples (for 1 day) of **TIFSIX-4-Ni**.

Supplemental figures for the previously unreported HUMs.

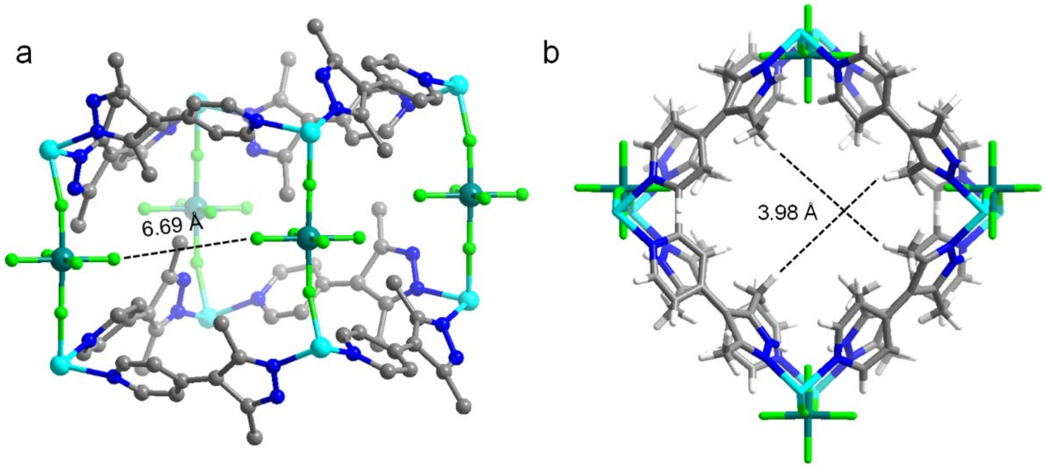

Figure S71. (a) View of the C_2H_2 binding pocket in adsorbent **TIFSIX-4-Ni** along the diagonally opposite F atoms of TiF_6^{2-} pillars; (b) View of the ultramicropore along the crystallographic b-axis of **TIFSIX-4-Ni**.

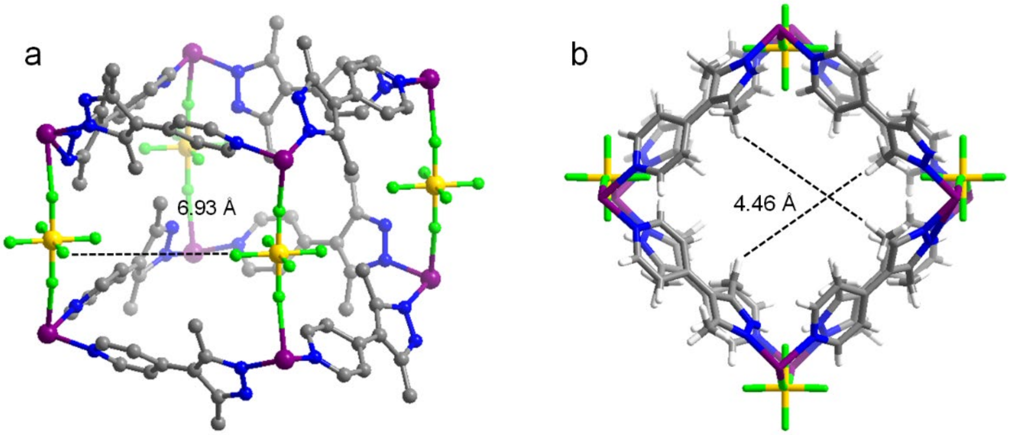

Figure S72. (a) View of the C_2H_2 binding pocket in adsorbent **SIFSIX-21-Cu** along the diagonally opposite F atoms of SiF_6^{2-} pillars; (b) View of the ultramicropore along the crystallographic b-axis of **SIFSIX-21-Cu**.

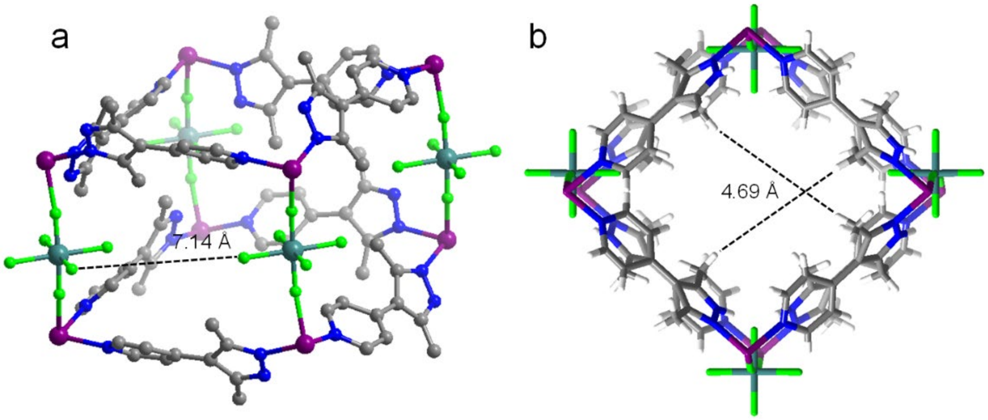

Figure S73. (a) View of the C_2H_2 binding pocket in adsorbent **TIFSIX-4-Cu** along the diagonally opposite F atoms of TiF_6^{2-} pillars; (b) View of the ultramicropore along the crystallographic b-axis of **TIFSIX-4-Cu**.

Tables S1-S4.

Table S1. Summary of structural information, sorption data and C_2H_2/CO_2 selectivities.

Material	Pore size (Å × Å)	S_{BET} / m^2g^{-1}	C_2H_2/CO_2 Q_{st} at zero loading (kJ mol^{-1})	C_2H_2/CO_2 Q_{st} at half loading (kJ mol^{-1})	C_2H_2/CO_2 uptakes at 1 bar,[a] mmol g^{-1}	S_{AC}[b]	α_{AC} (1:1/2:1)	Ref
[$Cu_2(pzdc)_2(pyz)$] [c]	4.0 × 6.0	571	42.5/31.9	–	1.9/0.07	26[d]	–	55, 56
Zn-MOF-74	11.0 × 11.0	1360	22.1/26.8	–	5.5/5.4	4[e]	–	57, 58
ZJU-60a	4.4 × 5.4	1627	17.6/15.2	–	6.7/3.3	6.7[e]	–	59
MIL–100(Fe)	5.5 × 8.6	2300	65.0/30.0	–	5.3/2.5	12.5[e]	–	60
PCP-33	9.0 × 22.0	1248	27.5/26.3	–	5.4/2.6	5.6[e]	–	61
FJU-22a	7.1 × 7.1	828	23.0/19.0	22.9/19.4	5.1/5.0	7.1[e]	1.9/–	12
UTSA-74a	8.0 × 8.0	830	31.0/25.0	31.4/25.5	4.8/3.2	14.3[e]	20.1/–	58
TIFSX-2-Cu-i	5.1 × 5.1	685	46.0/36.0	41.9/34.6	4.1/4.3	10.0[e]/10.7[f]	–/50[g]	62
UTSA-300a	2.4 × 3.3	311	57.6[h],30.0[i]/–	–	3.3/0.2	743	–	63
DICRO-4-Ni-i	6.2 × 6.6	398	37.7/33.9	35.4/34.6	1.9/1.0	18.2[e]/13.9[j]	–/13[g]	31
NKMOF-1-Ni	5.8 × 5.8	382	60.3/40.9	46.0/36.4	2.7/2.3	~60[e],[f]	2.6/1.8	64
JCM-1	12.5 × 3.9	550	36.9/33.4	–	3.3/1.7	13[e]	4.4/–	65
ZJU-196	5.1 × 5.1	–	39.2[h],15[i]/–	–	3.7/0.4	25[k]	–	66
[$Ni_3(HCOO)_6$]	4.3 × 4.3	289	40.9/24.5	–	2.4/1.6	22[l]	–	67
FJU-90a	5.4 × 5.1	1572	25.1/20.7	–	8.0/4.6	4.3[l]	–	68
JNU-1	16.3 × 6.6	818	13.0, 47.6[m]/–	–	2.7/2.2	3[e]	–	69
MUF-17	4.7 × 4.8	247	49.5/33.8	–	2.7[n]/2.2[n]	6[e]	–	70
ZJUT-2a	3.2 × 3.2	350	41.5/35.5	–	3.4/2.2	10[l]	–	71
FJU-89a	12 × 8	774	31.0/27.8	24.9/23.5	4.5/2.7	4.3	3	72
HOF-3	7.0 × 7.0	165	20.0	–	2.1/0.9	14.0	2.0	73
FJU-6-TATB	(15.6 × 6.4),	1306	29.0/26.0	–	4.9/2.6	5.3-3.1	2.3	74

	(16.9 × 21.9)							
SNNU-45	4.5 × 5.1	1006	39.9/27.1	31/26.9	6.0/4.3	8.5-4.5	2.9	75
JXNU-5	4.6, 6.7	406	32.9/25.2	30.2/26.8	2.5/1.5	5	9.9	76
FJU-36a	(9.1 × 13.4); (10.2 × 15.4)	409	32.9/31.1	–	2.3/1.6	2.8	2.1	77
FeNi-M′MOF	(4.15 × 4.27); (3.94 × 4.58)	383	27.0/24.5	27.0/24.9	4.3/2.7	24	1.7	78
TCuI	3.66 × 3.66	250	38.4/26.6	37.3/29.6	2.2/1.6	6.7[e]/6.5[f]	33.4/7.8	79
TCuBr	3.59 × 3.59	173	36.6/30.2	38.2/32.7	2.8/2.0	9.1[e]/9.1[f]	104.5/10.5	79
TCuCl	3.69 × 3.69	167	41.0/30.1	39.5/31.4	3.0/2.0	16.0[e]/16.1[f]	143.1/25.4	79
FJI-H8-Me	-	2044±3	33.7/21.8	-	10.2/4.7	10.4	-	80
SIFSIX-Cu-TPA	-	1330	39.1/25.7	-	8.3/4.8	5.3	1.97	81
SIFSIX-21-Ni	3.16 × 3.64	871	37.9/19.8	35.2/20.3	4.0/1.3	7.8	27.7/10.0	**This work**
TIFSIX-4-Ni	3.98 × 3.98	931	41.4/27.4	36.4/25.5	3.8/2.0	7.6	4.4/3.1	**This work**
NbOFFIVE-3-Ni	-	761	36.7/25.0	33.4/25.6	3.8/1.9	6.0	15.0/6.5	**This work**
SIFSIX-21-Cu	4.46 × 4.46	839	36.3/24.0	34.2/23.8	3.9/1.5	10.0	4.6/3.1	**This work**
TIFSIX-4-Cu	4.69 × 4.69	747	40.6/27.0	35.1/26.4	3.5/2.0	8.3	5.4/4.1	**This work**
NbOFFIVE-3-Cu	-	805	41.9/25.8	38.6/23.4	4.0/1.6	9.5	16.9/7.9	**This work**

[a] Unless otherwise mentioned, all values correspond to 298 K measurements; [b] unless otherwise mentioned, all values are calculated from IAST selectivities for 1:1 equimolar mixtures; [c] title compound is a metal-organic complex with 1D channels; [d] uptake ratio at 0.01 bar for 270 K measurements; [e] IAST selectivity at 0.15 bar for 1:1 ratio; [f] IAST selectivity at 0.15 bar for 2:1 ratio; [g] for gas mixture 10:5:85 $C_2H_2/CO_2/He$; [h] at zero loading; [i] consistent for loadings > 0.22 mmol g^{-1}; [j] uptake at 0.01 bar; [k] uptake ratio at 0.5 bar; [l] IAST selectivity at 1 bar for 1:1 ratio; [m] at uptake 2 mmol g^{-1}; [n] recorded at 293 K. [o] determined from Horvath–Kawazoe method applied on N_2 isotherm at 77 K.

Table S2. Crystallographic data of **SIFSIX-21-Ni**, **TIFSIX-4-Ni, SIFSIX-21-Cu** and **TIFSIX-21-Cu**.

	SIFSIX-21-Ni	**TIFSIX-4-Ni**	**SIFSIX-21-Cu**	**TIFSIX-4-Cu**
Formula	$C_{23}H_{34}F_6N_6NiO_3Si$	$C_{23}H_{34}F_6N_6NiO_3Ti$	$C_{26}H_{42}CuF_6N_6O_6Si$	$\mathbf{C_{25}H_{40}CuF_6N_6O_5Ti}$
Formula weight	643.33	663.108	740.28	**730.02**
Temperature/K	100.0	100.0	120.0(5)	**120.00(12)**
Crystal system	orthorhombic	orthorhombic	orthorhombic	**orthorhombic**
Space group	*Pnna*	*Pnna*	*Pnna*	***Pnna***
***a*/Å**	14.8769(12)	14.9625(11)	14.9853(16)	**16.2099(14)**
***b*/Å**	14.6342(11)	15.0720(12)	15.7634(10)	**14.7716(14)**
***c*/Å**	14.6946(11)	14.5962(12)	14.2288(16)	**14.445(2)**
***α*/°**	90	90	90	**90**
***β*/°**	90	90	90	**90**
***γ*/°**	90	90	90	**90**
Volume/Å^3	3199.2(4)	3291.7(5)	3361.1(6)	**3458.8(7)**
Z	4	4	4	**4**
ρ_{calc}, g/cm^3	1.335	1.338	1.463	**1.402**
μ/mm^{-1}	1.845	3.365	1.982	**0.918**
F(000)	1113	1145.2	1124.0	**1156.0**
Radiation	CuKα (λ = 1.54178)	CuKα (λ = 1.54178)	CuKα (λ = 1.54184)	**Mo *Kα* (λ = 0.71073 Å)**
Reflections collected	17785	19154	18207	**15644**
Independent reflections	1758 [R_{int} = 0.0849, R_{sigma} = 0.0427]	2516 [R_{int} = 0.0700, R_{sigma} = 0.0468]	3516 [R_{int} = 0.1237, R_{sigma} = 0.0795]	**3857 [R_{int} = 0.1230, R_{sigma} = 0.1354]**
Data/restraints/parameters	1758/194/240	2516/126/240	3516/255/235	**3857/257/193**
Goodness-of-fit on F^2	1.065	1.335	0.956	**0.994**
Final R indexes [I>=2σ (I)]	R_1 = 0.0764, wR_2 = 0.2105	R_1 = 0.0986, wR_2 = 0.2798	R_1 = 0.0946, wR_2 = 0.2621	**R_1 = 0.1167,** **wR_2 = 0.2982**
Final R indexes [all data]	**R_1 = 0.0936,** **wR_2 = 0.2303**	**R_1 = 0.1069,** **wR_2 = 0.2951**	**R_1 = 0.1358,** **wR_2 = 0.3034**	**R_1 = 0.1722,** **wR_2 = 0.3432**

Table S3. DSLF fitting parameters summary for C_2H_2 and CO_2 sorption.

Adsorbent	**gas**	q_1	k_1	n_1	q_2	k_2	n_2	R^2
NbOFFIVE-3-Ni	C_2H_2	3.591	0.0006	0.965	3.125	0.008	0.954	0.999
	CO_2	4.609	0.0008	1.180	0.180	0.009	0.939	0.999
SIFSIX-21-Ni	C_2H_2	4.060	0.006	1.878	0.059	4173.33	15.759	0.998
	CO_2	6.581	0.0003	1.048	0.094	0.0008	0.657	0.999
TIFSIX-4-Ni	C_2H_2	4.08225	1.6914	0.852066	1.40998	19.4212	0.991972	0.999
	CO_2	1 2.352	0.668	1.469	1.995	1.320	0.984	0.999
NbOFFIVE-3-Cu	C_2H_2	0.551	1.089	4.068	4.331	5.973	0.914	0.999
	CO_2	1.398	0.671	1.923	2.466	0.904	1.033	0.999
SIFSIX-21-Cu	C_2H_2	3.614	9.498	1.162	0.691	1.435	3.729	0.999
	CO_2	9.033	0.187	0.985	0.0140	5.9e-08	218.447	0.999
TIFSIX-4-Cu	C_2H_2	4.681	1.585	0.757	0.782	51.723	1.032	0.999
	CO_2	2.293	1.121	0.982	1.746	0.815	1.558	1

Table S4: Calculated averaged total potential energies (in kJ mol^{-1}) for a single C_2H_2 and CO_2 molecule, individually, positioned at their global minimum in **SIFSIX-21-Ni** as determined from CMC simulations at 298 K/0.10 atm.

Adsorbate	**HUM–Adsorbate Energy (kJ mol^{-1})**
C_2H_2	–40.40
CO_2	–25.85

References.

1. Waterman, K. C., Understanding and Predicting Pharmaceutical Product Shelf-Life. In *Handbook of Stability Testing in Pharmaceutical Development: Regulations, Methodologies, and Best Practices*, Huynh-Ba, K., Ed. Springer New York: New York, **2009**; pp 115-135.
2. Kumar, A.; Hua, C.; Madden, D. G.; O'Nolan, D.; Chen, K.-J.; Keane, L.-A. J.; Perry, J. J.; Zaworotko, M. J., Hybrid ultramicroporous materials (HUMs) with enhanced stability and trace carbon capture performance. *Chem.Commun.* **2017**, *53*, 5946-5949.
3. Krause, L.; Herbst-Irmer, R.; Sheldrick, G. M.; Stalke, D., Comparison of silver and molybdenum microfocus X-ray sources for single-crystal structure determination. *J. Appl. Crystallogr.* **2015,** *48*, 3-10.
4. Shen, J.; He, X.; Ke, T.; Krishna, R.; van Baten, J. M.; Chen, R.; Bao, Z.; Xing, H.; Dincӑ, M.; Zhang, Z.; Yang, Q.; Ren, Q., Simultaneous interlayer and intralayer space control in two-dimensional metal−organic frameworks for acetylene/ethylene separation. *Nat. Commun.* **2020**, *11*, 6259.
5. Sheldrick, G., SHELXT - Integrated space-group and crystal-structure determination. *Acta Crystallogr., Sect. A* **2015**, *71*, 3-8.
6. Sheldrick, G., Crystal structure refinement with SHELXL. *Acta Crystallogr., Sect. C* **2015**, *71*, 3-8.
7. Dolomanov, O. V.; Bourhis, L. J.; Gildea, R. J.; Howard, J. A. K.; Puschmann, H., OLEX2: a complete structure solution, refinement and analysis program. *J. Appl. Crystallogr.* **2009**, *42*, 339-341.
8. Rohatgi, A., *WebPlotDigitalizer: HTML5 based online tool to extract numerical data from plot images* **2015**, *Version: 4.2*.
9. Origin(Pro), Version 2021. OriginLab Corporation, Northampton, MA, USA..
10. Myers, A. L.; Prausnitz, J. M., Thermodynamics of mixed-gas adsorption. *AIChE J.* **1965**, *11*, 121-127.
11. Yang, R. T., *Gas separation by adsorption processes*. Butterworth-Heinemann: **2013**.
12. Yao, Z.; Zhang, Z.; Liu, L.; Li, Z.; Zhou, W.; Zhao, Y.; Han, Y.; Chen, B.; Krishna, R.; Xiang, S., Extraordinary Separation of Acetylene-Containing Mixtures with Microporous Metal–Organic Frameworks with Open O Donor Sites and Tunable Robustness through Control of the Helical Chain Secondary Building Units. *Chem. Eur. J.* **2016**, *22*, 5676-5683.
13. Bochevarov, A. D.; Harder, E.; Hughes, T. F.; Greenwood, J. R.; Braden, D. A.; Philipp, D. M.; Rinaldo, D.; Halls, M. D.; Zhang, J.; Friesner, R. A., Jaguar: A high-performance quantum chemistry software program with strengths in life and materials sciences. *Int. J. Quantum Chem.* **2013**, *113*, 2110-2142.
14. Schrödinger Release 2020-1: Jaguar, Schrödinger, LLC, New York, NY. 2020] in the Schrödinger software suite (Release 2020-1).
15. Grimme, S.; Antony, J.; Ehrlich, S.; Krieg, H. *J. Chem. Phys.* **2010**, *132*, 154104.
16. Hehre, W. J.; Radom, L.; von R. Schleyer, P.; Pople, J. A. Ab initio molecular orbital theory (Wiley, New York, 1986).
17. Schrödinger Release 2020-1: Maestro, Schrödinger, LLC, New York, NY, **2020**.
18. Chen, M.; Chen, S.; Chen, W.; Lucier, B. E. G.; Zhang, Y.; Zheng, A.; and Huang, Y. Analyzing Gas Adsorption in an Amide-Functionalized Metal Organic Framework: Are the Carbonyl or Amine Groups Responsible? *Chem. Mater.*, **2018**, *30*, 3613-3617.

19. Gul-E-Noor, F.; Mendt, M.; Michel, D.; Pöppl, A.; Krautscheid, H.; Haase, J.; and Bertmer, M. Adsorption of Small Molecules on $Cu_3(btc)_2$ and $Cu_{3-x}Zn_x(btc)_2$ Metal–Organic Frameworks (MOF) As Studied by Solid-State NMR. *J. Phys. Chem. C* **2013**, *117*, 7703-7712.
20. Eichele, K., WSolids1, Version 1.20.15. Universität Tübingen: Tübingen, Germany, 2011.
21. Vold, R. L.; Hoatson, G. L., Effects of jump dynamics on solid state nuclear magnetic resonance line shapes and spin relaxation times. *J. Magn. Reson*. **2009**, *198*, 57-72.
22. Kruger, P. E.; Moubaraki, B.; Fallon, G. D.; Murray, K. S., Tetranuclear copper(II) complexes incorporating short and long metal–metal separations: synthesis, structure and magnetism. *J. Chem. Soc., Dalton Trans.* **2000**, 713-718.
23. Jorgensen, W. L.; Maxwell, D. S.; Tirado-Rives, J., Development and Testing of the OPLS All-Atom Force Field on Conformational Energetics and Properties of Organic Liquids. *J. Am. Chem. Soc.* **1996**, *118*, 11225-11236.
24. Rappe, A. K.; Casewit, C. J.; Colwell, K. S.; Goddard, W. A.; Skiff, W. M., UFF, a full periodic table force field for molecular mechanics and molecular dynamics simulations. *J. Am. Chem. Soc.* **1992**, *114*, 10024-10035.
25. Bayly, C. I.; Cieplak, P.; Cornell, W.; Kollman, P. A., A well-behaved electrostatic potential based method using charge restraints for deriving atomic charges: the RESP model. *J. Phys. Chem.* **1993**, *97*, 10269-10280.
26. Kühne, T. D.; Iannuzzi, M.; Del Ben, M.; Rybkin, V. V.; Seewald, P.; Stein, F.; Laino, T.; Khaliullin, R. Z.; Schütt, O.; Schiffmann, F.; Golze, D.; Wilhelm, J.; Chulkov, S.; Bani-Hashemian, M. H.; Weber, V.; Borštnik, U.; Taillefumier, M.; Jakobovits, A. S.; Lazzaro, A.; Pabst, H.; Müller, T.; Schade, R.; Guidon, M.; Andermatt, S.; Holmberg, N.; Schenter, G. K.; Hehn, A.; Bussy, A.; Belleflamme, F.; Tabacchi, G.; Glöß, A.; Lass, M.; Bethune, I.; Mundy, C. J.; Plessl, C.; Watkins, M.; VandeVondele, J.; Krack, M.; Hutter, J., CP2K: An electronic structure and molecular dynamics software package - Quickstep: Efficient and accurate electronic structure calculations. *J. Chem. Phys.* **2020**, *152*, 194103.
27. van Duijnen, P. T.; Swart, M., Molecular and Atomic Polarizabilities: Thole's Model Revisited. *J. Phys. Chem. A* **1998**, *102*, 2399-2407.
28. Pham, T.; Forrest, K. A.; McLaughlin, K.; Tudor, B.; Nugent, P.; Hogan, A.; Mullen, A.; Cioce, C. R.; Zaworotko, M. J.; Space, B., Theoretical Investigations of CO_2 and H_2 Sorption in an Interpenetrated Square-Pillared Metal–Organic Material. *J. Phys. Chem. C* **2013**, *117*, 9970-9982.
29. Pham, T.; Forrest, K. A.; Banerjee, R.; Orcajo, G.; Eckert, J.; Space, B., Understanding the H_2 Sorption Trends in the M-MOF-74 Series (M = Mg, Ni, Co, Zn). *J. Phys. Chem. C* **2015**, *119*, 1078-1090.
30. Kirkpatrick, S.; Gelatt, C. D.; Vecchi, M. P., Optimization by Simulated Annealing. *Science* **1983**, *220*, 671.
31. Scott, H. S.; Shivanna, M.; Bajpai, A.; Madden, D. G.; Chen, K.-J.; Pham, T.; Forrest, K. A.; Hogan, A.; Space, B.; Perry Iv, J. J.; Zaworotko, M. J., Highly Selective Separation of C_2H_2 from CO_2 by a New Dichromate-Based Hybrid Ultramicroporous Material. *ACS Appl. Mater. Interfaces* **2017**, *9*, 33395-33400.
32. Mullen, A. L.; Pham, T.; Forrest, K. A.; Cioce, C. R.; McLaughlin, K.; Space, B., A Polarizable and Transferable PHAST CO_2 Potential for Materials Simulation. *J. Chem. Theory Comput.* **2013**, *9*, 5421-5429.

33. Jones, J. E.; Chapman, S., On the determination of molecular fields- II. From the equation of state of a gas. *Proc. Math. Phys. Eng. Sci.* **1924**, *106*, 463-477.
34. Ewald, P. P., Die Berechnung optischer und elektrostatischer Gitterpotentiale. *Ann. Phys. (Berl.)* **1921**, *369*, 253-287.
35. Wells, B. A.; Chaffee, A. L., Ewald Summation for Molecular Simulations. *J. Chem. Theory Comput.* **2015**, *11*, 3684-3695.
36. Applequist, J.; Carl, J. R.; Fung, K.-K., Atom dipole interaction model for molecular polarizability. Application to polyatomic molecules and determination of atom polarizabilities. *J. Am. Chem. Soc.* **1972**, *94*, 2952-2960.
37. Thole, B. T., Molecular polarizabilities calculated with a modified dipole interaction. *Chem. Phys.* **1981**, *59*, 341-350.
38. Bode, K. A.; Applequist, J., A New Optimization of Atom Polarizabilities in Halomethanes, Aldehydes, Ketones, and Amides by Way of the Atom Dipole Interaction Model. *J. Phys. Chem.* **1996**, *100*, 17820-17824.
39. McLaughlin, K.; Cioce, C. R.; Pham, T.; Belof, J. L.; Space, B., Efficient calculation of many-body induced electrostatics in molecular systems. *J. Chem. Phys.* **2013**, *139*, 184112.
40. Belof, J. L.; Space, B. Massively Parallel Monte Carlo (MPMC). 2012, Available on GitHub. https://github.com/mpmccode/mpmc.
41. Franz, D. M.; Belof, J. L.; McLaughlin, K.; Cioce, C. R.; Tudor, B.; Hogan, A.; Laratelli, L.; Mulcair, M.; Mostrom, M.; Navas, A.; Stern, A. C.; Forrest, K. A.; Pham, T.; Space, B., MPMC and MCMD: Free High-Performance Simulation Software for Atomistic Systems. *Adv. Theory Simul.* **2019**, *2*, 1900113.
42. Kresse, G.; Furthmuller, J., Efficiency of ab-initio total energy calculations for metals and semiconductors using a plane-wave basis set. *Comp. Mater. Sci.* **1996**, *6*, 15-50.
43. Kresse, G.; Furthmuller, J., Efficient iterative schemes for ab initio total-energy calculations using a plane-wave basis set. *Phys. Rev. B* **1996**, *54*, 11169-11186.
44. Wellendorff, J.; Lundgaard, K. T.; Møgelhøj, A.; Petzold, V.; Landis, D. D.; Nørskov, J. K.; Bligaard, T.; Jacobsen, K. W., Density functionals for surface science: Exchange-correlation model development with Bayesian error estimation. *Phys. Rev. B* **2012**, *85*, 235149.
45. Blochl, P. E., Projector augmented-wave Method. *Phys. Rev. B* **1994**, *50*, 17953-17979.
46. Pack, J. D.; Monkhorst, H. J., "Special points for Brillouin-zone integrations"-a reply. *Phys. Rev. B* **1977**, *16*, 1748-1749.
47. Monkhorst, H. J.; Pack, J. D., Special points for Brillouin-zone integrations. *Phys. Rev. B* **1976**, *13*, 5188-5192.
48. Vandichel, M.; Hajek, J.; Vermoortele, F.; Waroquier, M.; De Vos, D. E.; Van Speybroeck, V., Active site engineering in UiO-66 type metal-organic frameworks by intentional creation of defects: a theoretical rationalization. *Crystengcomm* **2015**, *17*, 395-406.
49. Vandichel, M.; Hajek, J.; Ghysels, A.; De Vos, A.; Waroquier, M.; Van Speybroeck, V., Water coordination and dehydration processes in defective UiO-66 type metal organic frameworks. *Crystengcomm* **2016**, *18*, 7056-7069.
50. Ghysels, A.; Verstraelen, T.; Hemelsoet, K.; Waroquier, M.; Van Speybroeck, V., TAMkin: A Versatile Package for Vibrational Analysis and Chemical Kinetics. *J Chem Inf Model* **2010**, *50*, 1736-1750.

51. Sotomayor, F. J.; Cychosz, K. A.; Thommes, M., Characterization of micro/mesoporous materials by physisorption: concepts and case studies. *Acc. Mater. Surf. Res* **2018**, *3*, 34-50.
52. Schejn, A.; Aboulaich, A.; Balan, L.; Falk, V.; Lalevée, J.; Medjahdi, G.; Aranda, L.; Mozet, K.; Schneider, R., Cu^{2+}-doped zeolitic imidazolate frameworks (ZIF-8): efficient and stable catalysts for cycloadditions and condensation reactions. *Catal. Sci. Technol.* **2015**, *5*, 1829-1839.
53. Kooli, F.; Kiyozumi, Y.; Rives, V.; Mizukami, F., Synthesis and Textural Characterization of a New Microporous Silica Material. *Langmuir* **2002**, *18*, 4103-4110.
54. Liu, L.; Ma, D.; Zheng, H.; Li, X.; Cheng, M.; Bao, X., Synthesis and characterization of microporous carbon nitride. *Microporous and Mesoporous Materials* **2008**, *110*, 216-222.
55. Matsuda, R.; Kitaura, R.; Kitagawa, S.; Kubota, Y.; Belosludov, R. V.; Kobayashi, T. C.; Sakamoto, H.; Chiba, T.; Takata, M.; Kawazoe, Y.; Mita, Y., Highly controlled acetylene accommodation in a metal–organic microporous material. *Nature* **2005**, *436*, 238-241.
56. Bloch, E. D.; Queen, W. L.; Krishna, R.; Zadrozny, J. M.; Brown, C. M.; Long, J. R., Hydrocarbon Separations in a Metal-Organic Framework with Open Iron(II) Coordination Sites. *Science* **2012**, *335*, 1606-1610.
57. Xiang, S.; Zhou, W.; Zhang, Z.; Green, M. A.; Liu, Y.; Chen, B., Open Metal Sites within Isostructural Metal–Organic Frameworks for Differential Recognition of Acetylene and Extraordinarily High Acetylene Storage Capacity at Room Temperature. *Angew. Chem. Int. Ed.* **2010**, *49*, 4615-4618.
58. Luo, F.; Yan, C.; Dang, L.; Krishna, R.; Zhou, W.; Wu, H.; Dong, X.; Han, Y.; Hu, T.-L.; O'Keeffe, M.; Wang, L.; Luo, M.; Lin, R.-B.; Chen, B., UTSA-74: A MOF-74 Isomer with Two Accessible Binding Sites per Metal Center for Highly Selective Gas Separation. *J. Am. Chem. Soc.* **2016**, *138*, 5678-5684.
59. Duan, X.; Zhang, Q.; Cai, J.; Yang, Y.; Cui, Y.; He, Y.; Wu, C.; Krishna, R.; Chen, B.; Qian, G., A new metal–organic framework with potential for adsorptive separation of methane from carbon dioxide, acetylene, ethylene, and ethane established by simulated breakthrough experiments. *J. Mater. Chem. A* **2014**, *2*, 2628-2633.
60. Yoon, J. W.; Lee, J. S.; Lee, S.; Cho, K. H.; Hwang, Y. K.; Daturi, M.; Jun, C.-H.; Krishna, R.; Chang, J.-S., Adsorptive Separation of Acetylene from Light Hydrocarbons by Mesoporous Iron Trimesate MIL-100(Fe). *Chem. Eur. J.* **2015**, *21*, 18431-18438.
61. Duan, J.; Jin, W.; Krishna, R., Natural Gas Purification Using a Porous Coordination Polymer with Water and Chemical Stability. *Inorg. Chem.* **2015**, *54*, 4279-4284.
62. Chen, K.-J.; Scott, Hayley S.; Madden, D. G.; Pham, T.; Kumar, A.; Bajpai, A.; Lusi, M.; Forrest, K. A.; Space, B.; Perry, J. J.; Zaworotko, M. J., Benchmark C_2H_2/CO_2 and CO_2/C_2H_2 Separation by Two Closely Related Hybrid Ultramicroporous Materials. *Chem* **2016**, *1*, 753-765.
63. Lin, R.-B.; Li, L.; Wu, H.; Arman, H.; Li, B.; Lin, R.-G.; Zhou, W.; Chen, B., Optimized Separation of Acetylene from Carbon Dioxide and Ethylene in a Microporous Material. *J. Am. Chem. Soc.* **2017**, *139*, 8022-8028.
64. Peng, Y.-L.; Pham, T.; Li, P.; Wang, T.; Chen, Y.; Chen, K.-J.; Forrest, K. A.; Space, B.; Cheng, P.; Zaworotko, M. J.; Zhang, Z., Robust Ultramicroporous Metal–Organic Frameworks with Benchmark Affinity for Acetylene. *Angew. Chem. Int. Ed.* **2018**, *57*, 10971-10975.

65. Lee, J.; Chuah, C. Y.; Kim, J.; Kim, Y.; Ko, N.; Seo, Y.; Kim, K.; Bae, T. H.; Lee, E., Separation of Acetylene from Carbon Dioxide and Ethylene by a Water-Stable Microporous Metal–Organic Framework with Aligned Imidazolium Groups inside the Channels. *Angew. Chem. Int. Ed.* **2018**, *57*, 7869-7873.
66. Zhang, L.; Jiang, K.; Li, L.; Xia, Y.-P.; Hu, T.-L.; Yang, Y.; Cui, Y.; Li, B.; Chen, B.; Qian, G., Efficient separation of C_2H_2 from C_2H_2/CO_2 mixtures in an acid–base resistant metal–organic framework. *Chem. Commun.* **2018**, *54*, 4846-4849.
67. Zhang, L.; Jiang, K.; Zhang, J.; Pei, J.; Shao, K.; Cui, Y.; Yang, Y.; Li, B.; Chen, B.; Qian, G., Low-Cost and High-Performance Microporous Metal–Organic Framework for Separation of Acetylene from Carbon Dioxide. *ACS Sustain. Chem. Eng.* **2019**, *7*, 1667-1672.
68. Ye, Y.; Ma, Z.; Lin, R.-B.; Krishna, R.; Zhou, W.; Lin, Q.; Zhang, Z.; Xiang, S.; Chen, B., Pore Space Partition within a Metal–Organic Framework for Highly Efficient C_2H_2/CO_2 Separation. *J. Am. Chem. Soc.* **2019**, *141*, 4130-4136.
69. Zeng, H.; Xie, M.; Huang, Y.-L.; Zhao, Y.; Xie, X.-J.; Bai, J.-P.; Wan, M.-Y.; Krishna, R.; Lu, W.; Li, D., Induced Fit of C_2H_2 in a Flexible MOF Through Cooperative Action of Open Metal Sites. *Angew. Chem. Int. Ed.* **2019**, *58*, 8515-8519.
70. Qazvini, O. T.; Babarao, R.; Telfer, S. G., Multipurpose Metal–Organic Framework for the Adsorption of Acetylene: Ethylene Purification and Carbon Dioxide Removal. *Chem. Mater.* **2019**, *31*, 4919-4926.
71. Wen, H.-M.; Liao, C.; Li, L.; Yang, L.; Wang, J.; Huang, L.; Li, B.; Chen, B.; Hu, J., Reversing C_2H_2–CO_2 adsorption selectivity in an ultramicroporous metal–organic framework platform. *Chem. Commun.* **2019**, *55*, 11354-11357.
72. Ye, Y.; Chen, S.; Chen, L.; Huang, J.; Ma, Z.; Li, Z.; Yao, Z.; Zhang, J.; Zhang, Z.; Xiang, S., Additive-Induced Supramolecular Isomerism and Enhancement of Robustness in Co(II)-Based MOFs for Efficiently Trapping Acetylene from Acetylene-Containing Mixtures. *ACS Appl. Mater. Inter.* **2018**, *10*, 30912-30918.
73. Li, P.; He, Y.; Zhao, Y.; Weng, L.; Wang, H.; Krishna, R.; Wu, H.; Zhou, W.; O'Keeffe, M.; Han, Y.; Chen, B., A Rod-Packing Microporous Hydrogen-Bonded Organic Framework for Highly Selective Separation of C_2H_2/CO_2 at Room Temperature. *Angew. Chem. Int. Ed.* **2015**, *54*, 574-577.
74. Liu, L.; Yao, Z.; Ye, Y.; Yang, Y.; Lin, Q.; Zhang, Z.; O’Keeffe, M.; Xiang, S., Integrating the Pillared-Layer Strategy and Pore-Space Partition Method to Construct Multicomponent MOFs for C_2H_2/CO_2 Separation. *J. Am. Chem. Soc.* **2020**, *142*, 9258-9266.
75. Li, Y.-P.; Wang, Y.; Xue, Y.-Y.; Li, H.-P.; Zhai, Q.-G.; Li, S.-N.; Jiang, Y.-C.; Hu, M.-C.; Bu, X., Ultramicroporous Building Units as a Path to Bi-microporous Metal–Organic Frameworks with High Acetylene Storage and Separation Performance. *Angew. Chem. Int. Ed.* **2019**, *58*, 13590-13595.
76. Liu, R.; Liu, Q.-Y.; Krishna, R.; Wang, W.; He, C.-T.; Wang, Y.-L., Water-Stable Europium 1,3,6,8-Tetrakis(4-carboxylphenyl)pyrene Framework for Efficient C_2H_2/CO_2 Separation. *Inorg. Chem.* **2019**, *58*, 5089-5095.
77. Liu, L.; Yao, Z.; Ye, Y.; Chen, L.; Lin, Q.; Yang, Y.; Zhang, Z.; Xiang, S., Robustness, Selective Gas Separation, and Nitrobenzene Sensing on Two Isomers of Cadmium Metal–Organic Frameworks Containing Various Metal–O–Metal Chains. *Inorg. Chem.* **2018**, *57*, 12961-12968.

78. Gao, J.; Qian, X.; Lin, R.-B.; Krishna, R.; Wu, H.; Zhou, W.; Chen, B., Mixed Metal–Organic Framework with Multiple Binding Sites for Efficient C_2H_2/CO_2 Separation. *Angew. Chem. Int. Ed.* **2020**, *59*, 4396-4400.
79. Mukherjee, S.; He, Y.; Franz, D.; Wang, S.-Q.; Xian, W.-R.; Bezrukov, A. A.; Space, B.; Xu, Z.; He, J.; Zaworotko, M. J., Halogen–C_2H_2 Binding in Ultramicroporous Metal–Organic Frameworks (MOFs) for Benchmark C_2H_2/CO_2 Separation Selectivity. *Chem. Eur. J.* **2020**, *26*, 4923-4929.
80. Di, Z.; Liu, C.; Pang, J.; Chen, C.; Hu, F.;Yuan, D.; Wu, M.; Hong, M. Cage‐like Porous Materials with Simultaneous High C_2H_2 Storage and Excellent C_2H_2/CO_2 Separation Performance. *Angew. Chem. Int. Ed.* **2021**, https://doi.org/10.1002/anie.202101907.
81. Li, H.; Liu, C.; Chen, C.; Di, Z.; Yuan, D.; Pang, J.; Wei, W.; Wu, M.; Hong, M. An Unprecedented Pillar-Cage Fluorinated Hybrid Porous Framework with Highly Efficient Acetylene Storage and Separation. *Angew. Chem. Int. Ed.* **2021**, *60*, 7547-7552.